A High-Sensitivity THz-Sensing Technology for DNA Detection with Split-Ring Resonator based Biochips

Christian Debus
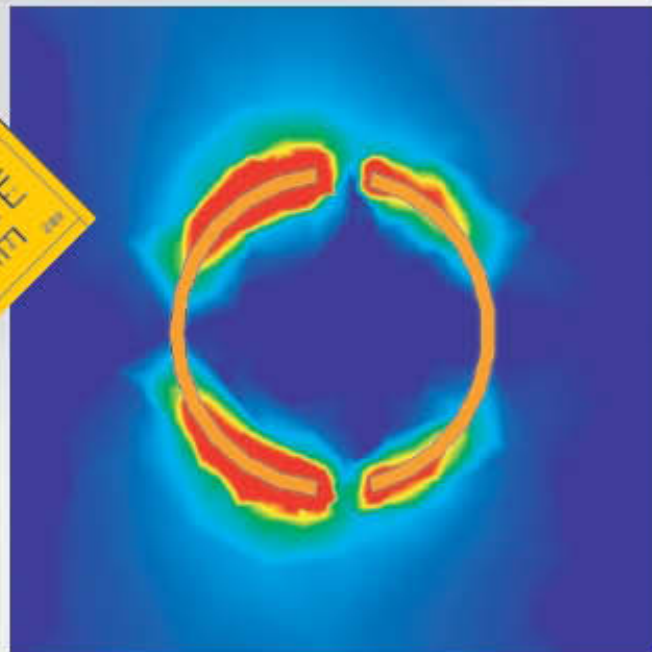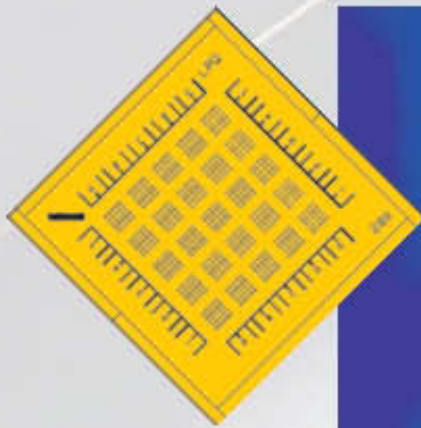
A High-Sensitivity THz-Sensing Technology for DNA Detection with Split-Ring Resonator based Biochips

Von der Naturwissenschaftlich-Technischen Fakultät
Universität Siegen

zur Erlangung des akademischen Grades
Doktor der Ingenieurwissenschaften
(Dr.-Ing.)

genehmigte
DISSERTATION

vorgelegt von
Dipl.-Ing. Christian Debus
aus Bergneustadt

Publications

Parts of this dissertation have already been published:

Journal Paper and Proceedings

- *"Frequency selective surfaces for high sensitivity terahertz sensing"*
  by Christian Debus & Peter Haring Bolívar
  in Applied Physics Letters 91, 184102 (2007).

- *"Terahertz biosensors based on double split ring arrays"*
  by Christian Debus & Peter Haring Bolívar
  in Proceedings of SPIE 6987, 69870U (2008).

- *"Terahertz Biochip Technology: Toward High-Sensitivity Label-Free DNA Sensors"*
  by Christian Debus, Peter Haring Bolívar, Mohammad Awad, & Michael Nagel
  in American Biotechnology Laboratory 27(6) pp. 8-11 (2009).

- *"All-Electronic THz Spectrometer for Biosensing"*
  by Christian Debus, Gunnar Spickermann, Michael Nagel, & Peter Haring Bolívar
  in Microwave and Optical Technology Letters 53(12), pp. 2899-2902 (2011).

Conference Contributions

- *"Frequency Selective Surfaces for High-Sensitivity Terahertz Sensors"*
  by <u>Christian Debus</u> & Peter Haring Bolívar
  at Conference on Lasers and Electrooptics (CLEO/QELS), Baltimore (USA), 6.-11. May 2007.

- *"New concepts for THz biomolecular sensing systems"*
  by Christian Debus, Francesco Voltolina, & <u>Peter Haring Bolívar</u>
  INVITED at 4ièmes Journées THz, Bombannes (France), 29.-31. May 2007.

- *"Towards Cost-Efficient THz Biochip Technologies"*
  by Christian Debus, Francesco Voltolina, & <u>Peter Haring Bolívar</u>
  at IEEE AP-S International Symposium, Honolulu (USA), 10.-15. June 2007.

- *"Recent Advances in Photonic Crystals and Metamaterials"*
  by Nigel P. Johnson, Ali Z. Khokhar, Basudev Lahiri, Scott McMeekin, Richard M. De La Rue, Christian Debus, & Peter Haring Bolivar
  INVITED at 9th International Conference on Transparent Optical Networks (ICTON 2007), Rome (Italy), 1.-5. July 2007.

- *"New approaches for high-sensitivity THz biosensing systems"*
  by Christian Debus, Francesco Voltolina, Dustin Surawicz, <u>Peter Haring Bolívar</u>
  INVITED at International Symposium Topical Problems of Biophotonics, Nizhny Nowgorod (Russia), 4.-11. August 2007.

- *"Terahertz Biosensors based on Double Split Ring Arrays"*
  by <u>Christian Debus</u>, Peter Haring Bolívar
  INVITED at SPIE Europe: Photonics Europe, Straßburg (France), 7.-11. April 2008.

- *"High Speed THz Biochip Reader System"*
  by <u>Christian Debus</u>, Gunnar Spickermann, Michael Nagel, Peter Haring Bolívar
  at Conference on Lasers and Electrooptics (CLEO:2011), Baltimore (USA), 1.-6. May 2011.

Kurzfassung

Die Detektion und Charakterisierung von dünnen dielektrischen Schichten und Biomolekülen sind von großem Interesse in der THz-Forschung, da viele Materialien charakteristische Eigenschaften in diesem Frequenzbereich aufweisen. Um Schichten, die sehr viel dünner sind als eine Wellenlänge, oder Materialmengen im Femtomol-Bereich zu detektieren werden spezielle Sensoren benötigt. Die Sensoren bestimmen die Permittivität bzw. den Brechungsindex eines Materials über die Laufzeitverzögerung des Signals in der Zeitbereichsmessung oder über das Verstimmen eines Resonators im Frequenzbereich. Biochips im Speziellen dienen der Detektion von Molekülen im sub-µm Größenbereich, z.B. DNA oder Proteine.

Zu Beginn der vorliegenden Arbeit wird der Stand der Technik in der THz-Dünnschichtmessung dargestellt und beurteilt. Die Entwicklung hin zur Detektion immer dünnerer Schichten führt zu der Erkenntnis, dass Resonatoren mit einer hohen Güte erforderlich sind, da mit ihnen eine effizientere Interaktion von Probe und elektrischem Feld möglich ist. Dazu wird der asymmetrische doppeltgeschlitzte Ringresonator (asymmetric double-split ring resonator – aDSR) erforscht. Er zeigt eine spektral scharfe Resonanz kombiniert mit einer starken Konzentration des elektrischen Feldes. Der aDSR wird periodisch angeordnet, entsprechend einer frequenzselektiven Oberfläche, die als zentrales resonantes Element des Biochips verwendet wird, um eine hohe Empfindlichkeit zu erreichen. Die Entwicklung dieses Biochips berücksichtigt neben Materialeigenschaften auch praktische und kommerzielle Aspekte. Der fertige Biochip ist eine strukturierte dreistöckige Metallschicht auf einem Glassubstrat, wobei die Strukturkanten unterätzt sind.

Zusätzlich wird ein Lesegerät für die Biochips entwickelt, das hinsichtlich einer Anwendung in biomedizinischen Labors ausgelegt wird. Gemessen an aktuell eingesetzter THz-Technologie ist das Lesegerät klein, einfach zu bedienen, erfordert wenig Wartung und hat reduzierte Investitionskosten. Das Lesegerät ist im Wesentlichen ein voll-elektronisches Spektrometer für den Frequenzbereich von 240 bis 320 GHz und benötigt für eine Messung 110 Millisekunden. Das System ist kompakter und preiswerter als ein vollwertiges Laborspektrometer, da nur ein spannungsgesteuerter Oszillator (VCO) verwendet wird. Die Hochfrequenz wird in Diodenmischern erzeugt und heterodyne Detektion wird künstlich durch das Zusammenspiel von Frequenzdurchlauf und Laufzeitverzögerung ermöglicht.

Die Funktionsfähigkeit von Biochip und Lesegerät wird demonstriert und durch Vergleichsmessungen mit THz-TDS bestätigt. Die Fähigkeit zur Detektion dünner Schichten wird anhand von dünnen Filmen aus Lacken bzw. Gelatine experimentell nachgewiesen. Hybridisierte DNA, die mittels Oberflächenfunktionalisierung an ausgewählten Stellen auf dem Biochip deponiert wird, wird detektiert. Diese Detektion kann jedoch nicht durch weitere Messreihen bestätigt werden. Gründe für diesen Ausfall werden untersucht und diskutiert.

<u>Abstract</u>

The detection and characterization of dielectric thin-films and biomolecules are of great interest for THz-research due to characteristic material properties at these frequencies. The detection of films much thinner than wavelength or material amounts in femtomol range requires specialized sensors. The sensors identify a material's permittivity, or refractive index, respectively, by a signal delay in the time domain or the detuning of a resonator in the frequency domain. A biochip in particular aims at the detection of sub-µm-size molecules, such as DNA or proteins.

This work begins with a review of the state-of-the-art THz-thin-film sensing approaches evolving towards lower film thicknesses. These indicate that more promising results are achieved with high-Q resonators due to their more efficient sample/E-field interaction. The asymmetric double-split ring resonator (aDSR) is researched, exhibiting a sharp resonance feature and a strong concentration of the electric field. In a two-dimensional array, corresponding to a frequency selective surface, the aDSR qualifies as the basic element for a biochip with a high sensitivity. For the biochip development material properties as well as practical and commercial aspects are taken into account. The result is a glass chip with a structured three-layer metal surface and undercut edges.

With regard to practical aspects, a biochip reader is developed being compact, easy to use, of low-maintenance and affordable, to find application in biomedical laboratories. The reader is essentially a fully-electronic spectrometer for 240 – 320 GHz, reading a single measurement spot in 110 Milliseconds. Compared to a classical network analyzer, the setup has reduced complexity and cost. It generates the high frequencies from a single voltage controlled oscillator by upconverting in diode-based mixers. Heterodyne detection is realized by utilizing the time delay of the signal sweeping through the frequency band.

The functionality of biochip and reader is compared to TDS measurements proving good results. The detection of dielectric thin-films is successfully applied with dye, photo-resist and gelatin. Hybridized DNA, deposited locally by a functionalization process, is detected. However, the DNA detection could not be confirmed by additional measurements. Causes for this failure are investigated and discussed.

Contents

1 <u>Introduction</u>

The search for applications for THz-radiation is a manifold and challenging field, which is taking place in various disciplines of science. THz-radiation being electromagnetic radiation in the spectral range between the microwave and the (far-infrared) optical regime is made accessible with technology from both, the electrical and the optical side. The earlier and established systems for THz-generation and -detection originate from optical research. These systems have been used to determine relevant fields of activity, which remain on a research level due to the complexity of the measurement setups. More recently, microwave components have become available for higher frequencies reaching the lower part of the THz-range which is interesting for applications. Generally, the microwave technology provides smaller and less complex setups than the optical equivalent. This technology is cheaper and more familiar to engineers, which makes THz-radiation more and more recognized beyond researchers. Industrial attention in particular, generates increasing interest in applications which are close to being market-ready. Therefore THz-research is not limited to basic research anymore, but becomes subject to interdisciplinary applied research.

THz-spectroscopy is widely used for material characterization. It has been shown that certain types of materials exhibit characteristic resonances, resulting in so-called spectral fingerprints. Remarkable results are found for example for explosives,[Fed05] making THz-radiation interesting for security applications, especially in connection with the capability to see through clothes or packaging. With this combination THz-cameras should be able not only to reveal hidden objects, but also to identify the objects' material.

Biomolecules, such as DNA, have various intermolecular modes in the THz-range resulting in a characteristic behavior of the electromagnetic properties.[Pic06, Har04, Bax11] But characteristic behavior is found even without the need for observing individual resonances. The bulk permittivity of DNA at THz-frequencies depends on the binding state of the DNA strands.[Bru00] Measurements of DNA[Har02] appear to be similar to measurements of thin dielectric films[Nag01] in terms of film thickness and measurement results. These experiments utilize an electromagnetic resonator to measure nonconductive dielectric material or DNA, respectively: The material is deposited in the electromagnetic field of the resonator where the permittivity affects the field. This deposition, also called loading, reduces the resonator's resonant frequency. Hence, the changing of the resonant frequency basically indicates the material's permittivity.

The THz-DNA-detection is realized without manipulation of the DNA samples, (i.e. without labeling the assays). In drug discovery it is common to label assays, for example with a fluorescent marker, to identify an interaction state. However, label-free assay analysis has several advantages over labeling, such as lower preparation effort and no possible interaction or contamination caused by the label.[Coo06] The proposed biosensor in this work makes use of a label-free procedure to identify DNA on the basis of minute amounts of sample material. This could allow the medical examination of patients for mutagen diseases in an early state.

Figure 1-1 depicts the idea of how the biochip works. Several probes are integrated on one chip, each requiring a resonator with a known single-stranded probe of DNA. The probe strands are produced artificially, so that their composition is known. Different probe strands are mounted to the different probe resonators. Thus the probes are sensitive to different samples. When the chip is exposed to a solution containing the sample, or target DNA, the single-stranded sample binds to its complementary strand, forming hybridized DNA (the double helix as seen on Probe10 in yellow illumination), while leaving the other probes denatured as they are. Thereby the unknown sample is identified indirectly. Its composition is complementary to those of the probe strand it binds to. To find out, at which resonator hybridization took place, the probes are illuminated consecutively with a THz-beam to determine the resonant frequency of the probe resonators. A probe at which the sample is hybridized exhibits a reduced resonant frequency.
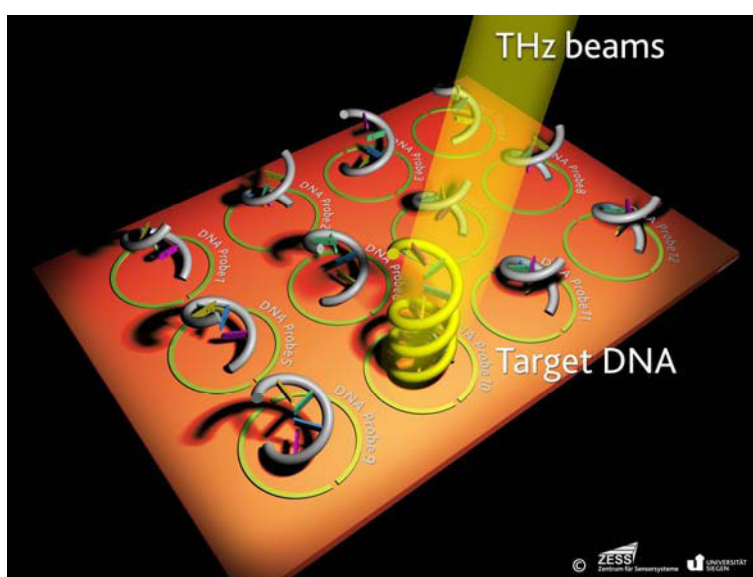
Figure 1-1: Artist's depiction of the biochip with twelve probe resonators (yellow rings), loaded with single-stranded probe DNA molecules (gray with colored nucleotides), and one hybridized probe/target DNA molecule illuminated by a THz-beam (transparent yellow).

The goal of this research is to develop a biochip and to demonstrate THz-technology to be qualified for everyday examination usage. The biochip is intended to be sensitive enough for the detection of minute amounts of DNA. This turns out to be similar to the detection of a dielectric thin-film which is a major topic in active THz-research, as discussed in chapter 2. The resonator requires a high Q-factor to be competitive to other label-free technologies, such as the widespread surface plasmon resonance (SPR).[Coo06] For practical and economical reasons, the resonator is a simple metallic structure: a modified split-ring resonator (SRR). The SRR combines a sharp resonance feature (high Q-factor) with a strong E-field concentration, as discussed in chapter 3. In chapter 4 the biochip is optimized for a high sensitivity on dielectric loading, taking into account technological and material aspects.

Due to free-space accessibility, the biochip is independent of the type of read-out setup and technology. Microwave components are becoming available in the THz-range providing a simpler alternative to the common optical THz-setups. The smaller and waveguide-connected

electronic components promise to require less maintenance and be more robust. The technology is discussed in chapter 5 and a demonstrator setup is presented proving the possibility to build a reasonable biochip reader with commercially available components.

The experimental results are presented in chapter 6 beginning with the verification of the bare biochip functionality. The biochip is used for sensing of dielectric thin-films achieving successful measurements of film thicknesses much lower than other thin-film sensing approaches, which are reviewed in chapter 2. A successful measurement of hybridized DNA on the biochip proves the biochip/reader technology to be working and indicates a very high sensitivity in the femtomol range. A further demonstration of the sensing capabilities would include a test series of DNA binding states. However, although the chemical handling of DNA strands is apparently known from publications, the test series fails due to DNA-handling related issues.

2 Terahertz Thin-Film Sensing

Chapter two provides an overview of thin-film sensing technologies in the Terahertz frequency range. Various approaches applying different devices to detect or characterize samples sized a fraction of the wavelength are reviewed. The chapter closes with a discussion on the terminology of sensitivity.

Biochemical materials have shown to be an interesting sample to be investigated with THz radiation.[Sie04] Macromolecule[I] properties, such as vibrational modes[Fis02] and binding states[Mic02], cause resonances in the THz range resulting in characteristic spectroscopic fingerprints[Glo02, Fis05] and broadband frequency dependent behavior[Bru00]. The challenge of measuring molecules with THz radiation is the huge difference between wavelength and molecule size. The wavelength at 1 Terahertz (300 μm) is approximately two orders of magnitude larger than the size of bacteria and 4 orders of magnitude larger than proteins or short DNA-strands.[II]

For measurements the material has to be arranged in the THz-beam of the setup in such a way that it effectively interacts with the radiation and can be exchanged reproducibly. Special preparation procedures are required depending on the type of sample. Because of their small size and instability as a bulk or film, macromolecules require a carrier or substrate. Preparation in solution is utile in means of handling but the strong absorption of THz-radiation by water reduces the signal strength significantly.[Sie04] Deposition and drying of the solution on a substrate results in sample spots with a very low and inhomogeneous height. With functionalization techniques molecules can be arranged as a film being homogeneous with respect to wavelength and diameter of the THz-beam focus.[III] Hence, the efforts to characterize macromolecules with THz-radiation are initially focused on sensing thin dielectric films in general. Thin-film characterization is also explored for nondestructive material test of coatings[The11], the analysis of semiconductor layers and nanotechnology devices[Bru02] and other technological areas[Mic02a].

Thin-films of a few micrometers or less in thickness and a low refractive index are challenging to be measured, as the thickness is much lower than THz-wavelengths and the refractive index is comparably close to those of the surrounding air. Thus, a special sensor device is required in the setup to amplify the sample's interaction with the THz-beam. The most common approaches are manipulation of the resonant frequency or the pulse delay of the sensor device by the sample material.

[I] In biology a macromolecule, such as a nucleic acid or protein, is a large molecule with a molecular weight of several thousand Dalton. It is a compound of small molecules, such as sugar or nucleotides.[Alber]

[II] Bacteria Escherichia Coli measure ca. 3 μm in length, DNA 0.3 nm per amino acid.[Alber]

[III] Functionalization is discussed in chapter 6.3.1 DNA-Functionalization on page 75.

2.1 THz-TDS and Improvements

In a classical THz-TDS[IV] setup samples are characterized by measuring a THz-pulse transmitted through the sample, as depicted in Figure 2-1(a). The received THz-pulse is compared to a reference pulse being the result from the same measurement without the sample. Depending on the sample material properties the pulse will be damped and delayed. While the damping is caused by reflection and absorption, the delay is caused by the reduced propagation velocity in material $v_m = \frac{v_0}{n_m}$. With a known sample thickness T the refractive index n_m can be derived from the delay time. THz-TDS is an established and powerful technology to coherently characterize dielectric materials[Har99] in transmission configuration, but the optimal sample thickness is in the range of 300 µm to 1 mm.[Wit08] Due to its wavelength of approximately 100 µm and larger TDS is not sensitive enough to measure µm-thick films.[Jia00] The sensitivity can be increased by differential TDS (DTDS) where the sample is moved in and out of the THz-beam at kHz rates. Transmission changes between sample and reference of -90 dB and film thicknesses as low as 100 nm have been measured.[Bru02] However, DTDS requires a complex setup and is unsuitable for the read-out of sample arrays.
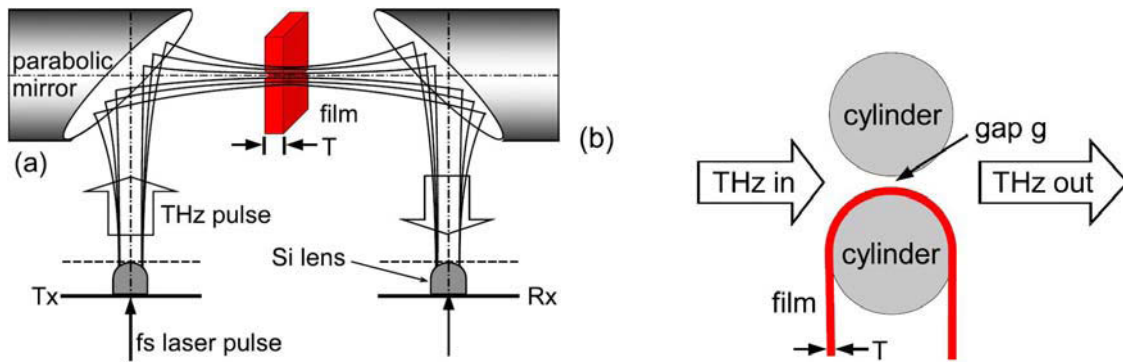
Figure 2-1 (with permission from [The10]): (a) Classical THz-TDS setup: The THz-radiation passes through the sample film one time only in orthogonal direction. (b) Passing through the gap g, more interaction between the film and the THz-radiation occurs.

To use TDS for thin-films the interaction length of THz-pulse and sample has to be increased. Multiple passes through the sample add up to results like from a thicker sample. However, disturbing multiple reflections might be generated at the sample interfaces depending on the setup design. A more effective way is to use the film as a waveguide transmitting the THz-pulse in surface direction instead of normal direction. In this configuration a dielectric film with thickness T surrounded by air can be assumed a dielectric waveguide and has the lowest cut-off frequency[Zinke]

$$f_c = \frac{c_0}{2T\sqrt{n_r^2 - n_{air}^2}} = \frac{c_0}{2T\sqrt{\varepsilon_r \mu_r - 1}} \tag{2-1}$$

resulting in a minimum thickness T = 150 µm at 1 THz with an exemplary $\varepsilon_r = 2$ and $\mu_r = 1$. Hence, micrometer thin films act as dielectric waveguides for frequencies two orders of magnitude larger.

[IV] Time Domain Spectroscopy (TDS) is discussed in chapter 5.1 THz-Spectroscopy on page 49.

Utilizing metallic waveguides as THz sensors is a successful approach. A parallel plate waveguide (PPWG) consists of two (conductive) metallic plates with an extent much larger than the distance between them. In the space between the plates an electromagnetic wave is guided in a direction parallel to the metal surfaces. Similar to the dielectric waveguide, the bandwidth of a PPWG is limited. The cut-off frequency corresponds to the largest wavelength which is equal to two times the distance between the plates, assuming E-field polarization perpendicular to the plates. The propagation speed in a metallic waveguide, such as the PPWG or a rectangular hollow waveguide, is reduced if dielectric material is deposited inside. A close-to-application setup is depicted in Figure 2-1(b). Two cylinders at a low distance represent an infinitely short PPWG (actually called 'gap') with adiabatic input and output horn-antennas. The THz- radiation passing through the gap is delayed by the dielectric film. The experiments by Theuer et al.[The10] show the capability of measuring films as thin as 2.5 µm with a considerable 0.25 ps delay time. The sensitivity is determined by the fill factor of the gap, so that it increases with increasing film thickness or decreasing gap width. Decreasing the gap also cuts off bandwidth impeding this technique from spectroscopic applications[The11] or measuring sub-µm thin films.

2.2 Resonators in Parallel-Plate Waveguides

In the preceding paragraph material properties are determined with time domain measurements by evaluating the delay of THz-pulses transmitted through a sample. Additional information for analysis is found in the frequency domain. The transmission spectra of sample and reference are obtained from the pulses by Fourier Transform. The frequency response of the sample is computed as the quotient of sample and reference spectra. A sensor device can now be designed to have a distinct spectroscopic characteristic which is modified by the sample material. As seen in chapter 2.1 a film at one side of a parallel-plate waveguide (PPWG) changes the transfer function and therefore the frequency response of the PPWG. For measurements in the frequency domain, a resonator can be integrated. The resonant frequency of a waveguide-based resonator depends on the refractive index of its environment. If dielectric material is brought into the E-field of the resonator its resonant frequency decreases. Comparing the spectra of the sample measurement and the reference measurement (empty resonator), the resonant frequency appears shifted. This frequency shift is therefore a measure for the amount or refractive index of the sample material.

Various waveguide-based sensor devices have been investigated, such as a PPWG with a single cavity and integrated microfluidic channel[Men09], metallized groove structures[Nag05] or a corrugation[Nag06] inside a PPWG as photonic band gap resonators, and a prism coupled THz waveguide sensor[Rau05] which is actually a special design of attenuated total reflection (ATR) a technology also being used for THz-spectroscopy[Hir04].
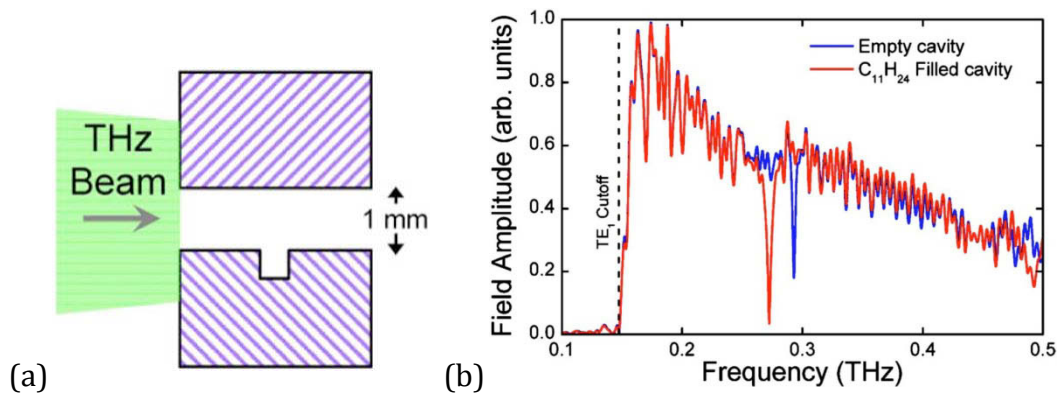
Figure 2-2 (with permission from [Men09]): (a) Sideview of the parallel-plate waveguide sensor with cavity (472 µm width, 412 µm depth) in the lower plate; (b) Frequency response of the sensor with empty and filled cavity (Undecane $C_{11}H_{24}$, n ≈ 1.41).

The setup of Mendis et al.[Men09] is depicted in Figure 2-2 (a). A cavity in one side of the PPWG acts as a narrowband band-stop filter as shown in Figure 2-2 (b) at 0.3 THz. When the cavity is filled with dielectric Undecane its resonant frequency decreases approximately by 20 GHz. The sensor is not sensitive in means of film-thickness (more than 400 µm), but the design of the gap as a microfluidic channel enables integration in a fluid process or even lab-on-chip configurations.
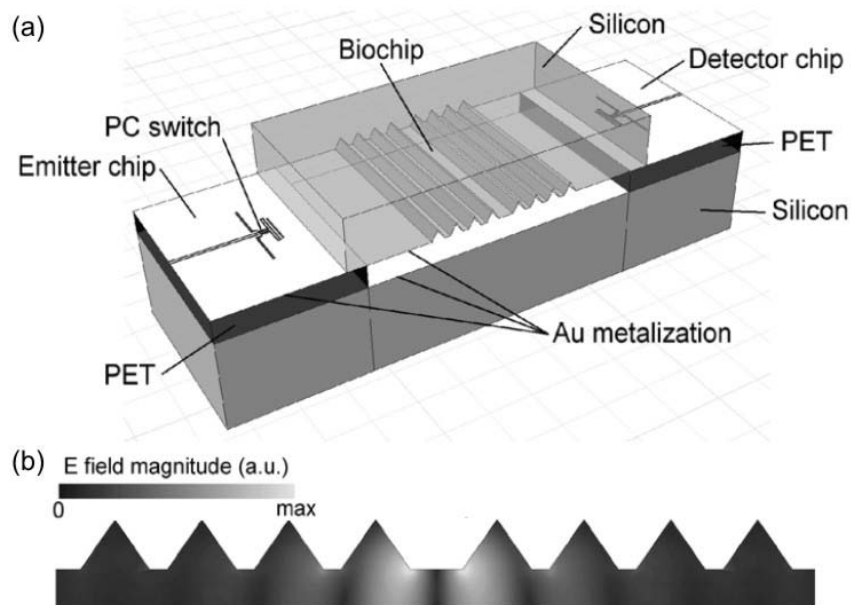
Figure 2-3 (with permission from [Nag06]): (a) Drawing of the modular setup including THz-emitter and -detector and the silicon parallel-plate waveguide (planar bottom-plate and biochip top-plate); (b) E-field distribution inside the waveguide.

A more complex resonator structure is the corrugated waveguide by Nagel et al.[Nag06] as depicted in Figure 2-3(a). Instead of a single cavity the top plate has a corrugation of eight equally spaced v-shaped grooves with a periodicity break in the middle. This photonic structure has a resonance resulting in a narrow transmission band at 501 GHz. Again, by deposition of dielectric material inside the resonator the resonance is shifted to a lower frequency. In this case the material is deposited selectively on all grooves and the middle four grooves, respectively. The numerical simulation reveals, that covering the middle grooves

only results in a frequency shift almost as large as covering all grooves. The reason for this is the distribution of the E-field in this resonator. Figure 2-3(b) shows, that the almost entire energy of the E-field is concentrated at the edges of the middle grooves. Material deposited here has a maximal effect, whereas a deposition at positions with a low field magnitude has a lower effect. The field concentration enables a smaller amount of material to manipulate the full field. Hence, the application of resonators increases the sensitivity because the required amount of material is reduced.

This approach contains a few interesting facts which will recur later in this work: A resonator is used to enhance the sensitivity of THz-spectroscopy and the E-field distribution suggests localized deposition of sample material at areas of higher strength to maximize the impact. Both features will be adressed in the FSS-biochip design in chapter 4. The modular design enables reusage of the complex and expensive source and detector components while the biochip to which the sample is attached can be exchanged seperately. This detachment of the biochip from the THz-spectroscopy hardware will be extended in this work to a fully independent biochip and read-out unit. Additionally, the biochip is technologically simple, thus allowing mass-usage and single-use applications. The biochip developed in chapter 4 is also designed in regard to a cost-efficient fabrication.

Other waveguide approaches for THz-sensing include plastic wires[You09] and tubes (Anti-Resonant Reflecting Hollow Waveguide ARRHW)[You10] and strip-line resonators in dipole[Nag02] and circular[Har04] configuration. The main disadvantages of waveguide-based sensors devices are their need to couple the THz-radiation into and out of the sensor device at defined ports and the fact they do not envision sensing different samples on one sensor. To avoid the port alignment, but enable sensors being capable of sensing sample arrays, free-space accessible devices are preferred.

2.3 **Metal Hole Arrays**

Planar sensor devices with resonators inside or on their surface are easy to handle and can be read-out with any THz-spectroscopy setup. Because of the free-space accessibility of planar devices multiple sensors can be integrated on one device thus enabling automated measurements of sample arrays.

A metal hole array (MHA) is a very simple device with resonance characteristics regarding impinging electromagnetic waves. A metal sheet with a thickness in the range of the sensing wavelength or smaller is structured with a periodic arrangement of circular holes. The hole diameter and the periodic distance are also in the range of the sensing wavelength, thus making them resonators. For sensing with low-frequency THz-radiation the holes can be conventionally drilled in the metal sheet. Miyamaru et al.[Miy10] built a MHA perforating a 300 μm thin metal sheet with 500 μm diameter holes in a triangular lattice with 1000 μm periodic distance. A plane electromagnetic wave impinging on this structure is mostly reflected except for a narrow passband at 0.32 THz. Covering the surface with a dielectric film changes the dielectric environment of the resonators and therefore the resonant frequency. As Figure 2-4 shows, the resonant frequency shifts 20 GHz on loading with a 50 μm Poly-

Propylene (PP) film. Similar to the effect inside the corrugated PPWG, the shift caused by the dielectric loading is stronger closer to the resonator. Five times the film thickness results in only two times the shift.
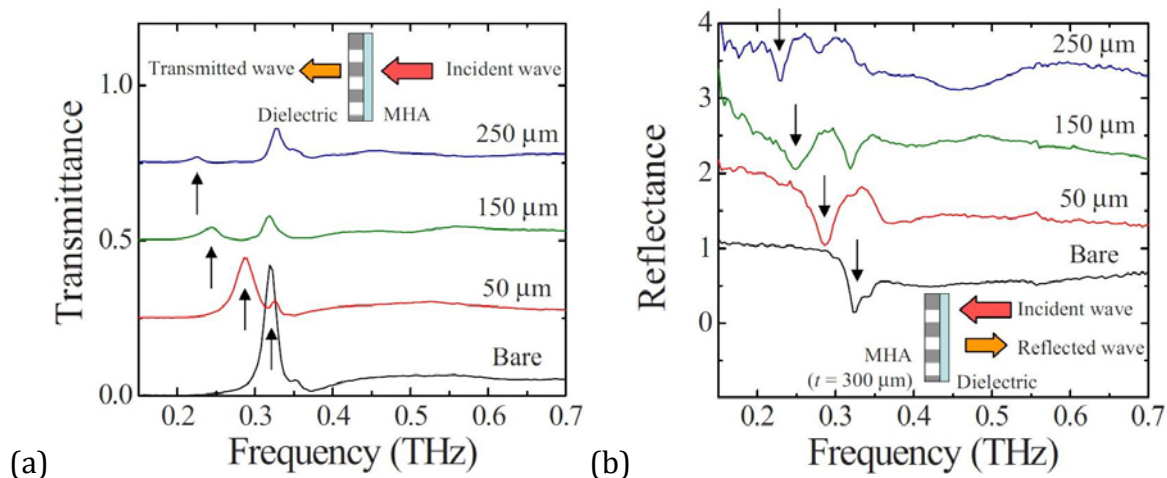
Figure 2-4 (with permission from [Miy10]): (a) Transmittance and (b) reflectance of a metal hole array (MHA) covered with PP-films of different thicknesses. The black arrows point to the MHA resonance.

It is also observed, that the amplitude of the resonance is decreasing with increasing film-thickness. Front- and back-side of the MHA have different resonant frequencies because of the dielectric loading. This resonance mismatch reduces the transmittance and weakens the resonance.[Miy10] Nevertheless this example proves the ability of designing planar sensor devices for thin-film sensing. Measurements are possible in transmission and reflection configuration and with a two-axis movement the device can be used for sample arrays without readjustment of the THz-optics.

A metal hole array can also be combined with a resonator and used for high-sensitivity sensing. From an optical point of view sub-wavelength MHAs excite photons travelling on the surface. Therefore the transmitted and reflected optical spectrum changes its composition. A periodicity break acts like a cavity storing the surface photon energy. The cavity in this so called photonic crystal can be designed to achieve very high Q-factors with a small cavity size.[Aka03] The photonic crystal with a cavity can be used as a sensor device for small amounts of dielectric sample material in the same way as the MHA but with a higher sensitivity. Alternatively a cavity with a low Q-factor, and thus a high bandwidth, can be used for absorption spectroscopy of small samples like single molecules.[Gel10]

2.4 Metasurfaces

Metamaterials (MM) are periodic combinations of subwavelength resonant structures which appear to have special frequency dependent bulk material characteristics.[V] An array of metamaterial resonators on a substrate is also known as metasurface or planar metamaterial and can be measured in a THz-spectroscopy setup in transmission and reflection. Like the metal hole array it has resonant characteristics regarding impinging electromagnetic waves.

[V] Metamaterials are discussed in chapter 3.7 on page 23.

But unlike the MHA the resonators are flat in terms of wavelength, so that the resonant frequency is depending on the surrounding materials' refractive indexes.[Munk1] Therefore the shape of the resonance will hardly change when the resonant frequency is shifted due to dielectric loading on one side of the resonators only. A prevalent resonator structure for MMs is the planar double split-ring resonator (SRR), as depicted in the inset of Figure 2-5(a). It exhibits several resonances which are affected by dielectric loading. In the work of O'Hara et al.[OHa08] a resonance at 1.35 THz shifts 2.5 GHz due to an 2.5 μm thin-film of photoresist (n = 1.64). Again, as shown in Figure 2-5(b), the resonant frequency shift does not rise linearly with film thickness. Contrary to the MHA the amplitude of the resonance hardly changes making the planar MM approach superior to the MHA approach. Additionally, with a distinct shift caused by 1.5 μm loading and saturating at 16 μm film-thickness the metasurface is more sensitive. However, the attempts to measure a sub-μm film are not satisfying. A 100 nm thin film of boron trioxide (B_2O_3) can be detected, but since the SRRs are made from 200 nm aluminum the sample is not a flat layer.[OHa08] This corroborates the need for a localized deposition of sample material at places of high E-fields. The double SRR consisting of two concentric rings has a large interaction area between the two rings. Smaller field concentrations are achieved with the structure investigated in this work, hence achieving a higher sensitivity.[VI]
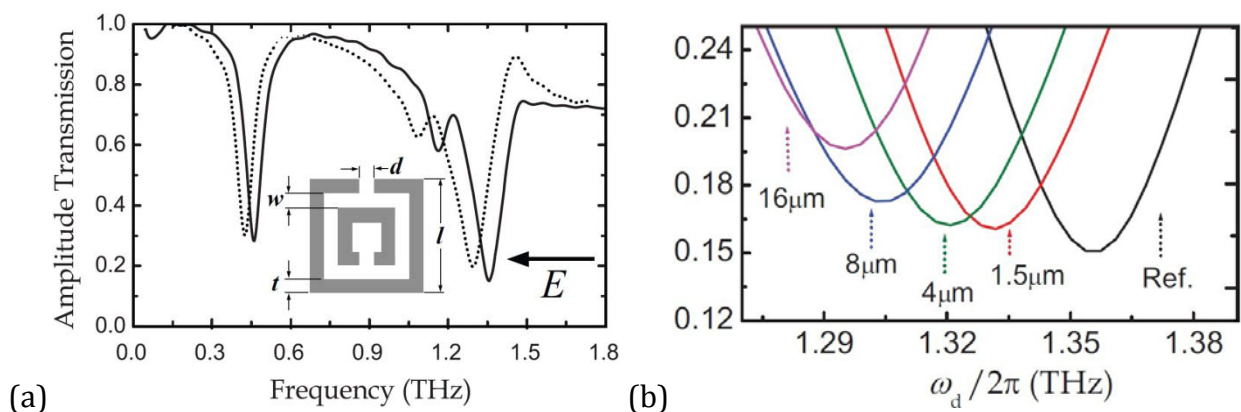
Figure 2-5 (with permission from [OHa08]): (a) Transmission of a metasurface without (solid trace) and with (dotted) 16 μm photoresist film. (b) Detailed view of the resonance with different film thicknesses.

2.5 "Sensitivity"

The term "sensitivity" is used in the relevant literature to describe how strong a sensor's reaction on sample material is. However, no comprehensive definition of "sensitivity" exists. The different sensors and applications include individual parameters making it difficult to find a universal definition to enable quantitative comparison.[OHa12]

The most common definition is *frequency shift Δf* divided by *refractive index unit RIU* of the sample. By this, the dependency of a sensor on a change of the material's refractive index is described, but a comparison to a different technology is rarely possible since the amount of sample material varies strongly between the different sensor technologies. The sample

---

[VI] See chapter 3.5 E-field Concentration on page 21.

amount is actually a critical figure for comparison. Flat sensor designs, such as the metasurface and the split-ring biochip presented in this work, are highly nonlinear and saturate at different film thicknesses. The metasurface has a larger $\Delta f/RIU$ than the split-ring but the minimum required film thickness is larger. With this simple definition the metasurface is more sensitive although the split-ring is capable of detecting a much lower thickness. This example shows, that "sensitivity" is even used in different ways: For sensor response (e.g. $\Delta f/RIU$, $\Delta f/\mu g$) as well as for threshold (e.g. minimal detectable thickness, minimal detectable refractive index).

Regarding the detection of DNA binding-states the primary aim of this research is to reduce the required thin-film thickness to measure smaller amounts and shorter DNA strands. The split-ring resonator being the core component of the biochip is optimized for a high sensitivity meaning that the frequency shift Δf is maximized for a reference thin-film which is assumed to represent a DNA film functionalized to the surface (chapter 4.2). This procedure increases the response for thin-films of similar dimensions and material properties.

3   <u>Split-Ring Resonator Arrays</u>

> Split-Rings are planar resonant structures which have gained a lot of interest recently, especially in conjunction with metamaterials research. In this chapter the functionality of the split-ring resonator (SRR) is explained and as a special case the asymmetric double-split ring (aDSR) is developed being the basic element of the proposed biochips. Important aspects which lead to the biochip design, such as material and substrate influences and the localized E-field concentration are discussed in detail.

As discussed in chapter 2 the sensing of DNA molecules can be realized similarly to the detection of dielectric material. DNA sample material can be deposited on a biochip forming a thin quasi-homogenous film with a thickness in the nanometer range corresponding to the molecule size. Instead of covering the full chip surface the material can be deposited on limited sections, thus forming sample spots a few nanometers thin and micrometers wide only.[I] Therefore the biochip has to be made very sensitive to react on such a small deposition. A common realization is measuring the detuning of a microwave resonator: When dielectric material is brought into the resonator's E-field the resonant frequency decreases. This frequency shift depends on the amount and the permittivity of the material as well as the exact position in the E-field, due to its inhomogeneous distribution. This technique was successfully demonstrated at THz-frequencies with DNA sample material in a bulk deposition on a microstrip resonator.[Nag02] The detection of small frequency shifts (caused by smaller amounts of material) requires a resonator with a high Q-factor because the movement of steeper flanks in the spectrum can be recognized at a lower S/N.

In this work the resonator being investigated is a frequency selective surface (FSS) actually being a two-dimensional array of resonant elements. For a "good" FSS a resonant element should be small compared to wavelength, why loop types are recommended.[Munk1] Additionally, those elements can be designed operating from narrow- to wide-band. Well known structures of this type exhibit ordinary resonance characteristics with comparably low Q-factors. Achieving a higher Q-factor thus requires extraordinary resonance modes such as the "closed mode" in asymmetric double-split rings.[Pro03]

3.1   <u>Frequency Selective Surfaces</u>

In the microwave domain a frequency selective surface (FSS) is an array of resonant metallic structures on a surface (or in some cases free-standing, e.g. metal hole arrays). One element of the periodic array is called a unit cell containing a resonant element and spacing to the neighboring elements. A FSS acts like a filter regarding incident electromagnetic waves. Hence it can be used to selectively transmit or reflect frequency bands. Besides scientific applications[Win99], FSSs have been used for antenna reflectors[Mar19, Varda] and radomes[Wu, Munk1] to separate or select the desired frequency and reject other signals which would raise the noise power or produce distortions. The strongest advancements of FSS came with military

---

[I] See chapter 6.3.1 DNA-Functionalization on page 75.

interest in radar counter measures reducing the radar cross section (RCS) of vehicles, namely the stealth technology.[Munk1] Today the most widespread application is the door of a microwave oven,[Wu] keeping decimeter wave radiation inside while enabling the user to look through in the visible regime.

The FSS resonance is primarily shaped by the resonant element in the unit cell. Interactions between the elements result in modifications of the resonances. The full surface appears to exhibit the element resonance behavior because of the periodic arrangement. The strength of the resonance depends on the spacing between the elements. If the distance between the elements is too large, radiation can pass the surface without interacting with the resonators. The far-field resonance of the FSS will therefore be weaker than the element resonance. Depending on the element geometry reducing the distance may also affect inter-element influence requiring element resizing to maintain the resonant frequency.

The biochips are read-out with freely propagating radiation focused on the chip surface with the direction of propagation being perpendicular to the surface. Therefore, the radiation can be considered a plane wave (TEM-mode) when impinging on the FSS. Generally, FSS characteristics depend on the angle of incidence of the radiation. Refraction causes narrowband components of the radiation to change the direction of propagation. The frequencies of these, so called, grating lobes depends on the periodic distance between the elements. Because of the fixed 0° angle from the perpendicular no grating lobes will be excited, except for the onset grating lobe also called Wood's Anomaly: Due to the periodic arrangement and synchronous excitation of the resonating elements a wave will be propagating along the surface if the excitation wavelength equals the element distance.[Munk1] This additional resonance feature is not suitable for the sensing of the desired small samples but for full surface coverings only. To avoid interaction between the element resonance and this effect, the size of the unit cell is designed sufficiently smaller than the resonant wavelength. By this, the resonances are separated in frequency and can be utilized independently.

(a)   (b)
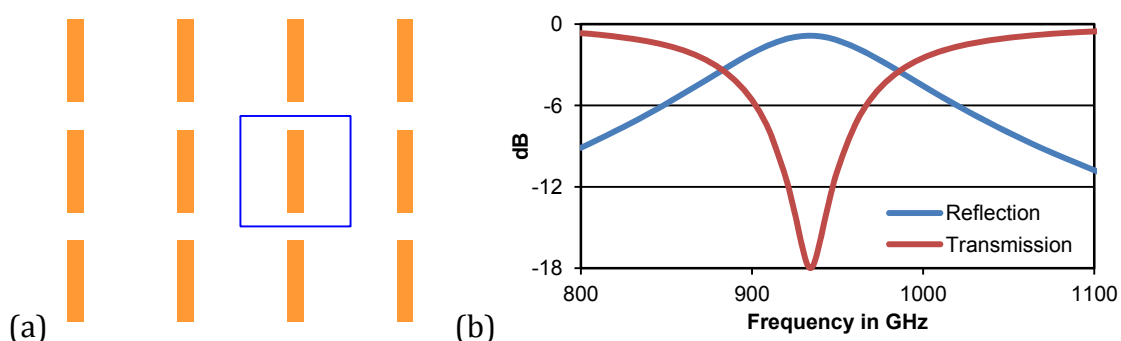
Figure 3-1: (a) FSS with 150 µm long λ/2-dipoles (orange) with depiction of the unit cell (blue) and (b) corresponding reflection / transmission diagram (orthogonal incidence, E-field polarized along dipoles).

One of the simplest forms of a FSS is a dipole-array such as the example shown in Figure 3-1(a). An electromagnetic plane wave impinging in perpendicular direction experiences a filtering effect if the E-field is polarized along the dipoles. The FSS resonant frequency is lower

than the dipole resonant frequency due to capacitive coupling to neighboring elements and because the effective length[Heilm] of a dipole antenna is larger than its mechanical length. The length of the example $\lambda/2$-dipole elements is 150 µm corresponding to a resonant wavelength of 300 µm or 1 THz resonant frequency, respectively, but with an effective FSS resonance at 934 GHz. Transmission and reflection of this FSS, shown in Figure 3-1(b), are almost complementary. Only little losses occur due to the low thickness of the metal. But with a Q-factor $Q_\omega \approx 10$ the resonance is not sharp enough for sensitive detection.

The resonant frequency of a simple FSS element, such as the $\lambda/2$-dipole, depends linearly on its size. An element that is optimized for a certain purpose can be adopted for any other frequency by simply scaling all measurements with the ratio between the actual and the desired resonant frequency. Deviations are caused only if the ratio of line width to thickness is changed. The scalability of the biochip FSS is discussed in chapter 4.9.

3.2   Split-Ring Resonators

The split-ring resonator (SRR, Figure 3-2(a)) was originally presented as a high-Q magnetic resonator in the UHF-band.[Har81] It is used as a planar element in array configurations for various applications: In a concentric double configuration (Figure 3-2(b)) it was assembled as an array to build a material with an artificial bulk permeability[Pen99] and used to demonstrate a negative index of refraction in a so called metamaterial.[She01] Single[Saf07] and concentric double[Lai08] SRRs have also been used to build band filters in microstrip technology. Thin-film sensing capabilities have been presented for the single SRR[Dri07] and the asymmetric double-split ring resonator (aDSR, Figure 3-2(d))[Deb07/this work] in the THz-range and the infrared[Lah09], respectively.

(a)   (b)   (c)   (d)
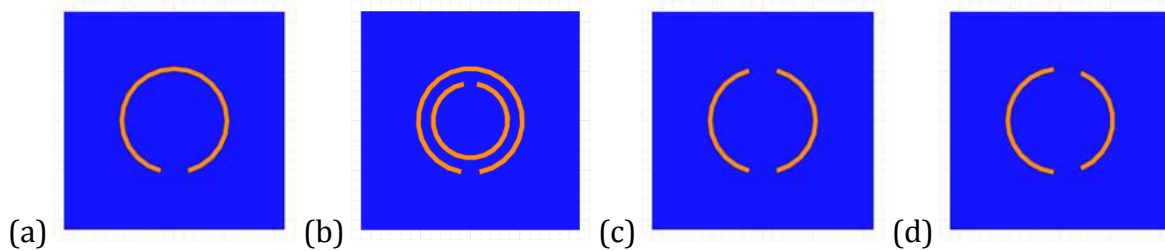
Figure 3-2: Evolution of the split-ring resonator: (a) single split-ring (SRR), (b) concentric double split-ring (dSRR), (c) symmetric double-split ring (DSR), and (d) asymmetric double-split ring (aDSR).[II]

In principal, a split-ring is a circular structure with a gap. Because of this gap the resonance behavior depends on the polarization direction of the incident E-field. With the predominantly used polarization across the gap (in Figure 3-2 from left to right) a strong magnetic moment appears near resonance[Mar05] implicating usage for metamaterial design.[Gay02] Extended freedoms for designing the electric and magnetic dipole resonance are achieved with the concentric double split-ring resonator.

[II] The notation of the rings in Figure 3-2(b) and (c) varies depending on publication and author. They are mostly called a "double split-ring" without differentiation. Actually, (b) shows two rings with one split each, while (c) is one ring split twice. Hence, the author chooses to discriminate by moving the hyphen and using different abbreviations: (b) is a double split-ring resonator (dSRR) and (c) is a double-split ring resonator (DSR).
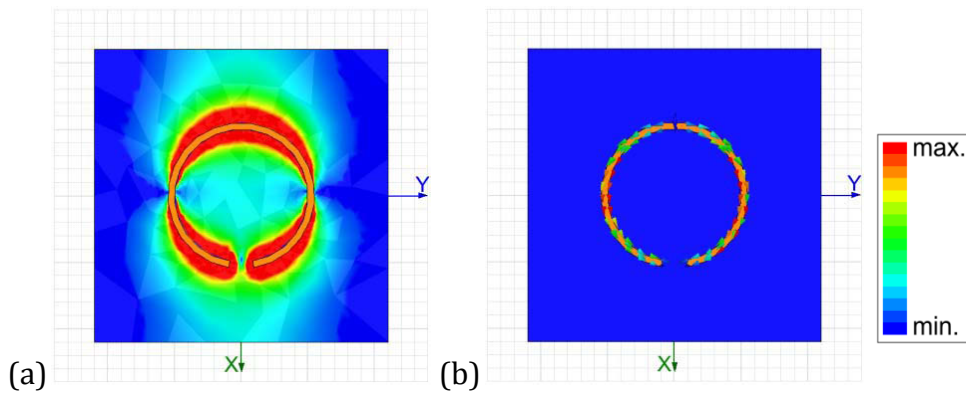
Figure 3-3: (a) E-Field magnitude and (b) surface current vector along the SRR with excitation polarization along X-axis.

Contrary to this, for an exciting E-field polarization along the uninterrupted ring (in Figure 3-2 from top down) the SRR appears to be similar to a straight dipole. Figure 3-3 depicts the E-field distribution and the corresponding surface current at the first resonance (base-mode). Both resemble those of a pair of $\lambda/2$-dipoles. The gap does not affect the resonance since the current is naturally zero at his point. If the ring was closed half the resonant wavelength would approximately be equal to half the ring circumference. The actual resonant wavelength is shorter than the arc length due to the fact that the arcs are not straight but "bent" dipoles. Additionally, the field can hardly exceed the arc length because the other arc's field with the same polarity is in its way.
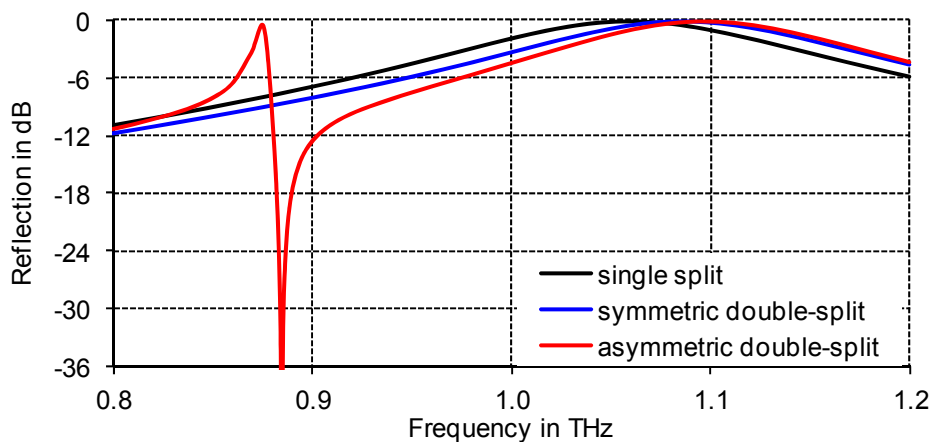
Figure 3-4: Reflection of split-ring resonator based FSSs with different types of split-ring resonators; Base-mode at 1060 GHz / 1090 GHz and dual resonance feature (DRF) at 880 GHz. (HFSS simulation, pec in vacuum)

Figure 3-4 depicts the reflections of FSSs composed of the resonators shown in Figure 3-2(a, c, and d). All rings have an inner and outer radius of 50 μm and 55 μm, respectively, and all gaps are 20° wide. Each gap of the aDSR has a 4° offset. Losses and substrate are not considered at this point. The simulation assumes a freestanding resonator in vacuum made of a practically perfect electronic conductor (pec) with a conductivity of 10^{30} S/m. The unit cell containing one resonator has periodic boundary conditions. Hence the results are valid for a 2D-array of infinite extend. The SRR exhibits a broadband resonance at 1060 GHz. The symmetric DSR shows a similar spectral behavior. The two arcs of the DSR are slightly shorter than the corresponding two sections of the SRR resulting in a slightly higher resonant

frequency. Moving both splits to the right side breaks the symmetry regarding the x-axis. The broad base-mode of the asymmetric DSR is almost identical to those of the symmetric case. Additionally, a dual resonance feature (DRF) appears at 880 GHz with a full reflection and a full transmission close in frequency. The flank between these extrema promises to be steep enough for sensitive sensing configurations.

Different explanations for the origin of this resonance feature exist in literature including closed modes / trapped modes[Pro03, Fed07], analog of electromagnetically induced transparency (EIT)[Pap08], Fano resonance[Sin11], a resonance hybridization model[Lah11], and antenna pair interaction[Deb07/this work].

The aDSR can be considered a ring with two gaps or a set of two arcs with identical center. Figure 3-5(a) depicts the E-field of the aDSR at the maximum of the dual resonance feature. Both arcs exhibit field distributions similar to those of a $\lambda/2$-dipole. For comparison a structure with straight dipoles of corresponding length and distance has been investigated.[Deb06] This earlier work proves that the explanation utilizing dipole behavior is consistent. The only deviation is found in the coupling strength between neighboring elements, which is much stronger between the straight dipoles as shown in Figure 3-5(b), whereas the aDSR has a stronger coupling between the two arcs of the same resonant element.[III]

(a)   (b)
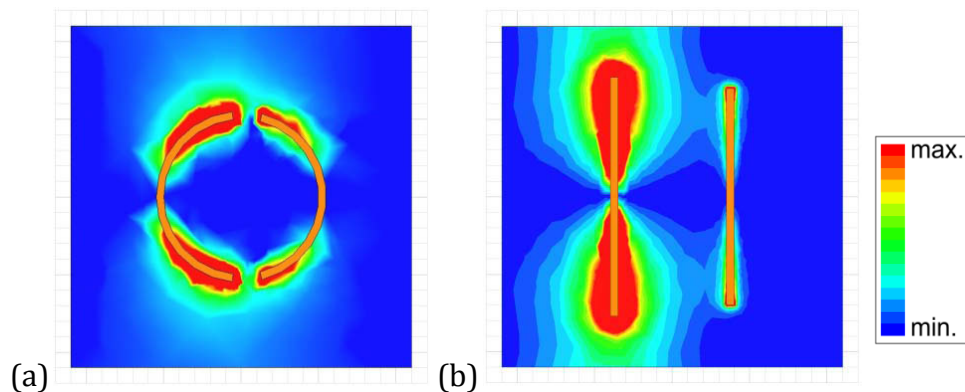
Figure 3-5: E-field magnitude of a FSS element at the maximum of the dual resonance feature of the (a) aDSR and (b) double dipole structure.

A closer look at a single arc is given in Figure 3-6. The exciting plane wave is electrically polarized in x-direction (from top down). The current distribution indicates a $\lambda/2$-dipole-like mode, as introduced above. The simulation is performed in vacuum without substrate, keeping $\varepsilon = \varepsilon_0$ real and therefore the dielectric displacement D proportional to the electric field E. The E-field vectors pointing from the lower to the upper end of the arc follow a curved trace completing the arc to a circle. This field distribution suggests arranging two arcs on a circle for effective coupling. A second arc positioned along this E-field would be linked by the displacement causing a current to flow in the same direction, which is in the same rotational direction as in the primary arc, but opposite to the plane wave excitation polarization. To

---

[III] The dipole pair structure is inferior to the split-rings in means of resonance strength. However, it is being investigated[Mat10] and will be advantageous as soon as applications reach much shorter wavelengths e.g. in the visible where its straight edges can be manufactured more easily than the round edges of the split-ring.

depict both quantities at a maximum, in Figure 3-6 the phases of surface current (J) and E-field differ by 90°, as given by Maxwell's Equation

$$rot\ \mathcal{H}(\vec{r},t) = \mathcal{J}(\vec{r},t) + \frac{\partial \mathcal{D}(\vec{r},t)}{\partial t} \tag{3-1}$$

for time-harmonic fields ($\mathcal{F}(\vec{r},t) = Re[F(\vec{r}) \cdot e^{j\omega t}]$):[Balan]

$$rot\ H(\vec{r}) = J(\vec{r}) + j\omega D(\vec{r}). \tag{3-2}$$

(a)   (b)
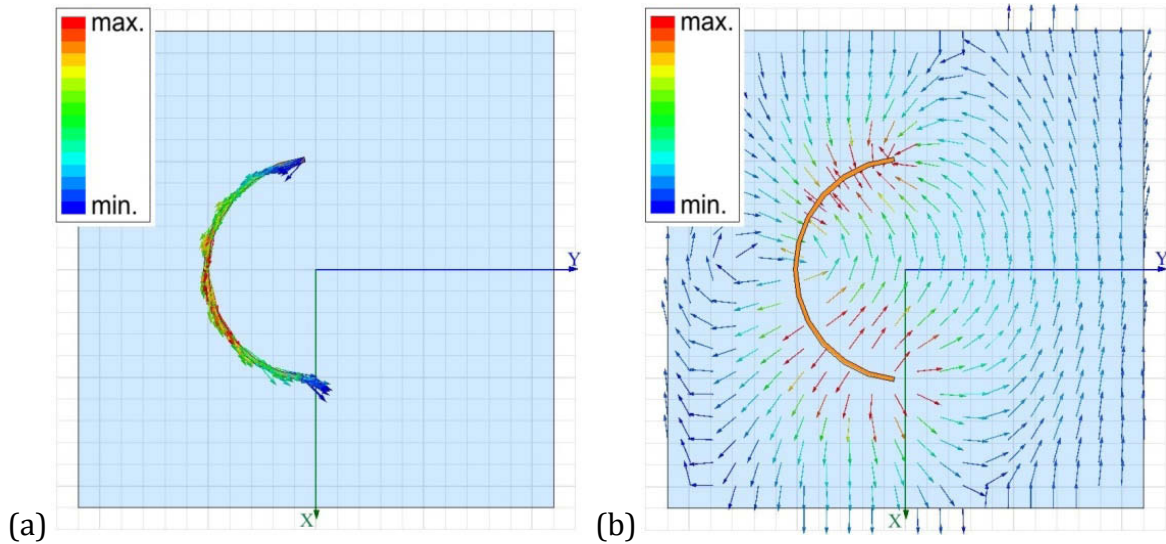
Figure 3-6: Single arc of the aDSR in resonance: (a) surface current vector and (b) electric field vector with a 90° phase difference.

875 GHz   885 GHz   890 GHz   1090 GHz

DRF below zero   DRF zero   DRF above zero   base-mode
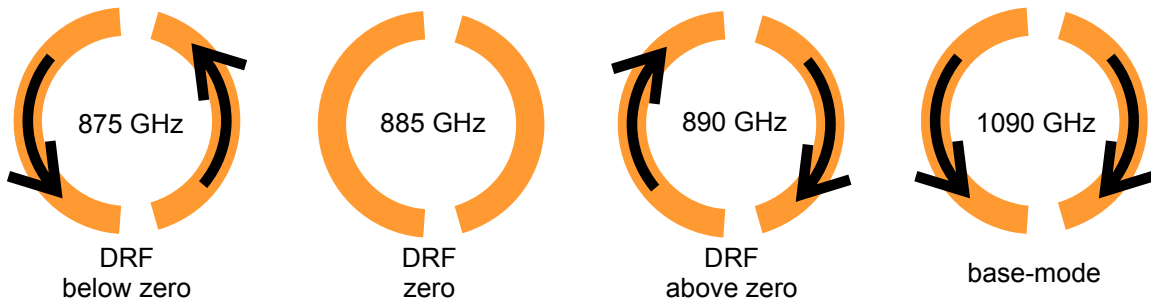
Figure 3-7: Current directions in an aDSR at the maximum (875 GHz), the zero (885 GHz), and the shoulder at the high frequency side (890 GHz) of the dual resonance feature (DRF), and at the base-mode (1090 GHz). (Excitation polarization is from top down.)

For the full aDSR structure with two arcs this means that each arc gets excited by the impinging plane wave and by the field of the other arc. The strength of the latter one is strongly depending on frequency and with the two arcs having different resonant frequencies, because of their different lengths, this leads to circular currents in the ring structure, as depicted in Figure 3-7. The long arc in resonance at 875 GHz excites a current in the short arc which is stronger than the primary current caused by the plane wave. As a result the direction of the short arc current is opposite to the polarization direction of the incident wave. When the short arc is in resonance at 890 GHz the same effect takes place vice versa. The strength of the short arc resonance is significantly weaker because of the length ratio of the arcs. Between

the two resonance modes where their strength is equal the currents cancel out each other at 885 GHz. Without a current the impinging wave passes the structure unhindered and the reflection spectrum has a zero. In distance to the DRF the currents are directed as in the base-mode, in both arcs following the direction of excitation polarization. Thus, the spectral feature at 880 GHz is a superposition of the resonances of the interacting arcs and therefore called a dual resonance feature (DRF).

The above simulations are performed with idealized parameters to qualitatively describe the aDSR behavior with a full reflection and a zero. However, several relevant properties such as conductivity, substrate, and grid configuration affect the shape of the DRF, especially the formation of the zero.

3.3 Conductivity (Gold at 1 THz)

The theoretical maximum and minimum of the DRF are at extreme values because of the almost perfect conductivity (σ_{pec} = 10^{30} S/m) of the ring material used in the HFSS simulation. From a practical point of view gold is chosen as material for the split rings because it is highly conductive, non-corrosive, and stable at room temperature. The material parameters for the quasi-optical THz-regime are computed from the complex dielectric function via Drude model:[Joh72, Maier]

$$\varepsilon_r^* = \varepsilon' + j\varepsilon'' = 1 - \frac{\omega_p^2 \tau^2}{1 + \omega^2 \tau^2} + j \frac{\omega_p^2 \tau}{\omega(1 + \omega^2 \tau^2)} \tag{3-3}$$

$$\varepsilon_r^* = 1 + \frac{j\sigma}{\varepsilon_0 \omega} \tag{3-4}$$

with plasma frequency ω_p and electronic impulse relaxation time τ. Transposing equation (3-4) for the conductivity σ results in

$$\sigma = j\varepsilon_0 \omega (1 - \varepsilon_r^*). \tag{3-5}$$

With plasmon frequency ω_p = 1.37·10^{16} Hz and damping frequency ω_τ = 1/τ = 4.05·10^{13} Hz [Ord83], [IV] the real parts of the dielectric function and conductivity exhibit an almost constant value for frequencies from 100 GHz to 1 THz.[Deb06] These values are used for the THz-simulations in this work:

$$\varepsilon_{r,AuTHz} = -1.12 \cdot 10^5 \tag{3-6}$$

$$\sigma_{AuTHz} = 4.01 \cdot 10^7 \; {}^{S}\!/_{m} \tag{3-7}$$

Figure 3-8 depicts the reflection of the same FSS as above with different materials assigned to the aDSR structure. Changing from perfect conductor (pec) to gold the overall shape of the spectrum stays the same with the broad resonance not changing at all and the DRF still

---

[IV] Plasmon frequency and damping frequency are given in [Ord83] as frequency in wavenumbers, but denotet with "ω" (ω=f), whereas here "ω" denotes the angular frequency (ω=2πf) and is given in Hertz.

appearing. Both DRF extrema become more moderate. The steep part of the flank still reaches 11 dB within 5 GHz. Further lowering of the conductivity reduces the steepness of the flank significantly.
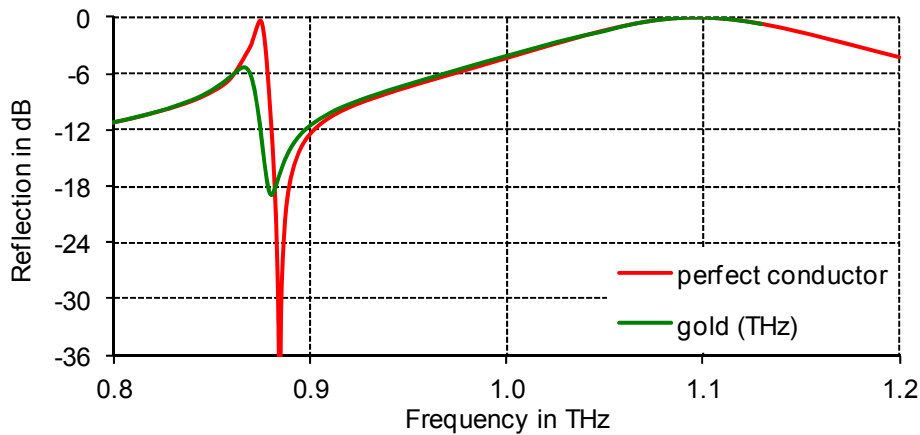
Figure 3-8: Reflection of an aDSR based FSS with the different conductor materials perfect electronic conductor (pec) and gold (with THz-parameters).

3.4 Substrate Influence

The aDSR based FSS above is assumed to be freestanding metal structures in vacuum. In practice a substrate is required on which the split rings are arranged. The metal thickness is very small compared to wavelength, but the substrate is in the order of wavelength. Therefore the split rings can be assumed to be at the interface of two half-spaces. Regarding the resonators the total surrounding media has to be taken into account as one effective medium. With a dielectric substrate ($\mu_r = 1$) in vacuum ($\varepsilon_r = 1$) the effective refractive index and permittivity can be approximated for microwave[Munk1] as well as THz-frequencies[MDo00]:

$$n_{eff} = \sqrt{\frac{n_{substrate}^2 + 1}{2}} \implies \varepsilon_{r,eff} = \frac{\varepsilon_{r,substrate} + 1}{2} \tag{3-8}$$

Changing the substrate's refractive index causes two significant changes to the DRF. If the structure size is maintained the resonance frequency decreases with increasing n_{eff}. Figure 3-9 depicts the DRF of the same FSS on different substrates. The frequency axis is divided by the effective refractive index to compare the shape of the DRFs for different substrate materials. All DRFs appear at the same f/n_{eff} proving the approximation to be correct. The DRF modulation being the difference between maximum and minimum which is 13 dB for vacuum reduces drastically with rising n_{eff} and looses steepness. Hence a substrate with a low refractive index is required for a good resonance feature.
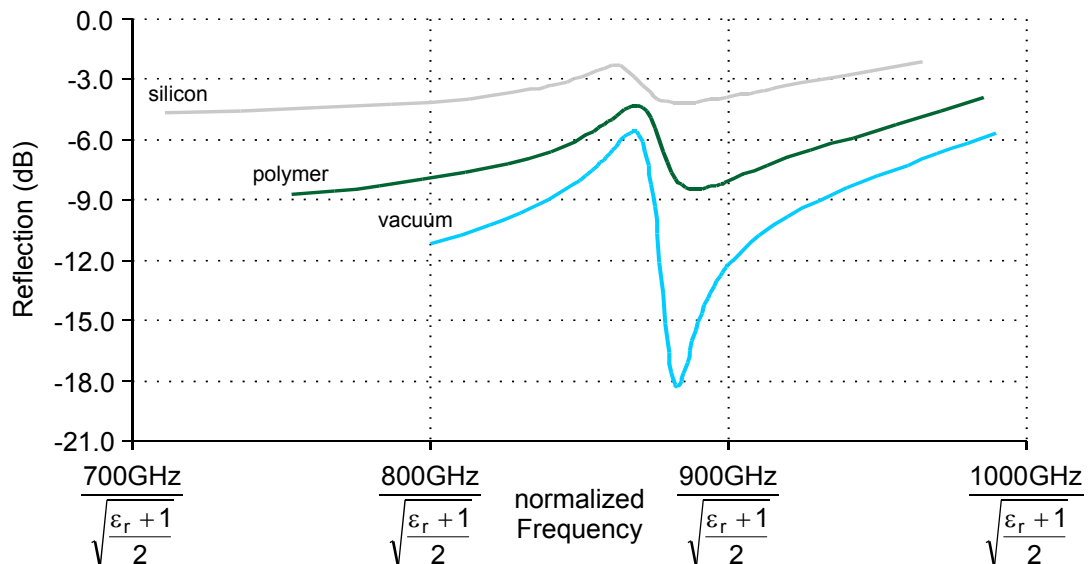
Figure 3-9:[Deb08/this work] Dual resonance feature of an aDSR based FSS on different substrates ($\varepsilon_{silicon} = 11.9$, $\varepsilon_{polymer} = 3.2$). Frequency is divided by the effective refractive index.

On the other hand, maintaining the resonant frequency and increasing the substrate refractive index reduces the resonator size. Thus a high refractive index can be used to reduce the size of the biochip and therefore the amount of sample material. For a good agreement the substrate can be optimized by configuring the thickness to be half the resonant wavelength. This measure matches the wave impedance thus minimizing the reflection at the substrate surface.

3.5 E-field Concentration

The strong coupling between the two arcs of the aDSR causes the E-field to concentrate at the ends of the arcs. As Figure 3-10 shows, most of the area of the FSS element is free from energy.
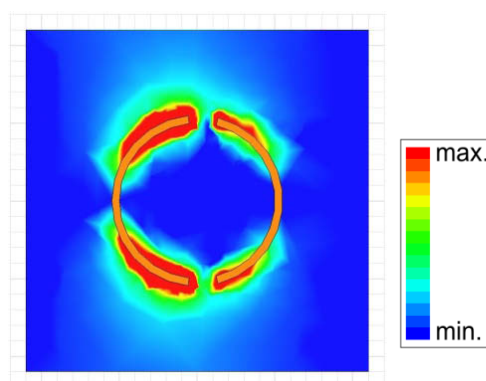
Figure 3-10: The E-Field along an aDSR at maximum reflection (875 GHz) shows a strong concentration of the field at the ends of the long arc.

Depositing dielectric material on the aDSR will cause the resonant frequency to shift to a lower value because the dielectric environment changes and the effective refractive index increases. The field concentration reveals two advantages here. In Figure 3-11(a) the full surface is covered with a dielectric film ($\varepsilon_r = 3.2$) of 10 nm thickness which is $\lambda/34000$ only. With a frequency shift of 5 GHz this extremely thin layer can easily be detected. Instead of

covering the full surface the material can be concentrated at the long arc's end where the E-field is concentrated. In Figure 3-11(b) a small square covering one 64th of the element surface only causes almost the same result with a shift of 4 GHz. Material deposited here interacts with a large portion of energy in the resonator, whereas material deposited at areas of low field amplitudes has almost no effect. This example demonstrates that selective deposition reduces the amount of required sample material significantly and therefore increases the sensitivity. The deposition of DNA-samples selectively at certain areas is possible by the chemical procedure of localized functionalization as discussed in chapter 6.3.1.

(a)   (b)
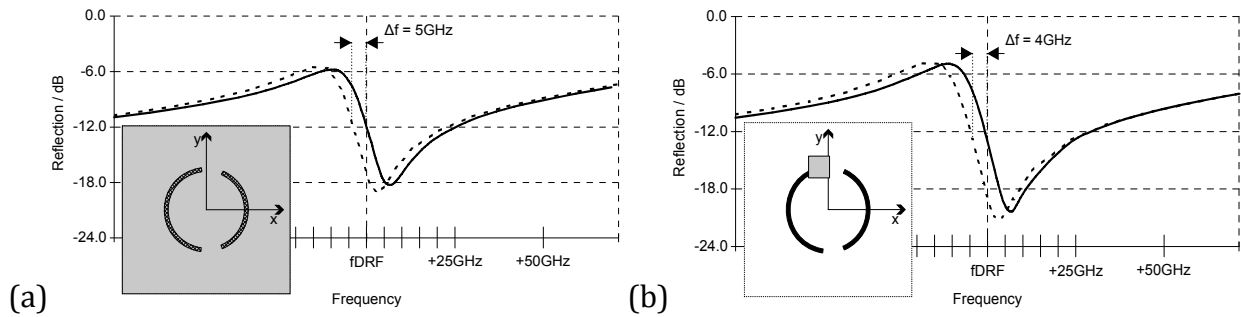
Figure 3-11:[Deb07/this work] Covering (a) the full surface with dielectric material has almost the same effect on the frequency shift as (b) localized functionalization covering only one 64th of the surface.

In addition to the macroscopic investigation of the E-field concentration at the arc ends the distribution within this lobe can be optimized. The E-field at the metal/air interface has its highest enhancement close to the surface. This peak is depending on the material's conductivity and can be increased for submillimeter wavelengths by using a doped semiconductor, such as InSb, instead of gold.[Gel08] As the results will show the conductivity of gold is sufficient for biochips operating at 300 GHz. Thus it will be used due to lower costs and less a complex manufacturing process.

3.6 **Babinet Principle**

An important feature of FSSs, which is made use of in this work, is the Babinet Principle. The theory is valid for idealized structures of infinitely low thickness and perfect conductivity. The idealized aDSRs are positive structures made from conductor and surrounded by loss-less vacuum. To this, a complementary structure can be designed being a conductive plane with apertures shaped like aDSRs. The Babinet Principle states, that if the polarization directions of E-field and H-field are exchanged the reflection spectrum of the positive structure and the transmission spectrum of the complementary structure look identical. The practical advantage is, that with one version investigated the complementary problem is solved, too. Special care has to be taken when a substrate is added, because the two versions of the FSS will then behave vastly differently.[Munk1] The Babinet Principle has been demonstrated on double split-ring resonators[Fal04] and on SRRs in the THz-regime[Bit11]. With dielectric substrate, finite metal thickness, and finite conductivity the result deviates, as shown in Figure 3-12. The amount of transmitted energy is lower through the apertures, but the resonances become sharper and the DRF modulation deeper.
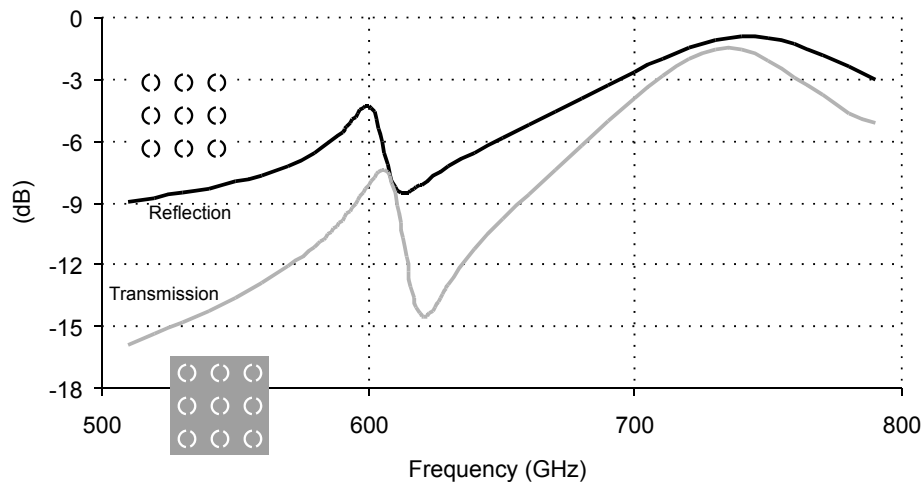
Figure 3-12:[Deb08/this work] Babinet Principle: The reflection spectrum of a FSS and the transmission spectrum of its complementary structure look the same if the polarization orientation of E- and H-field are exchanged. The deviation is due to realistic simulation parameters including finite dimensions, losses, and substrate.

3.7 SRRs for Metamaterials

Split-ring resonators, such as the models discussed above, are the central element in present metamaterials research. In a short excursus SRRs are investigated with regard to metamaterials in the infrared.
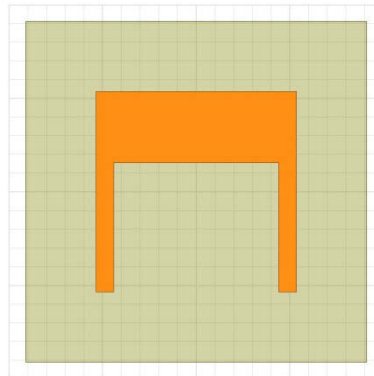
Figure 3-13: Unit cell of a LHM approach at 222 THz (λ = 1350 nm): The SRR has become angular with regard to fabrication capabilities. The SRR side-length is 200 nm.

Metamaterials are artificially manufactured periodic structures smaller than wavelength, macroscopically exhibiting bulk properties "that go beyond those found readily in nature".[Balan] Large interest exists in negative refractive index (NRI) materials, also called left-handed media (LHM) with E- and H-field and wave-vector k forming a left-handed system ($\vec{k} \Downarrow \vec{E} \times \vec{H}$), contrary to the naturally right-handed ($\vec{k} \Uparrow \vec{E} \times \vec{H}$). Hence, the wave-vector (visualized: the propagation of a wave-front) in an LHM is directed opposite to the Poynting Vector. Taken as a "black box", an LHM exhibits both a negative permittivity and negative permeability resulting in a negative index of refraction. The theory conforms with previously known phenomena such as the one-dimensional "backward-wave".[Eleft] Possible technical applications are seen in lens design ("Veselago planar lens"), cloaking, miniaturization of components, and more.[Balan] However, since the experiments inhibit a strong damping of the "negative refracted" signal, the phenomenon might also be explained by scattering from

surface waves in finite periodic structures.[Munk3] In that case the NRI behavior is not only limited to a certain frequency range, but also to distinct directions of propagation and scattering orders.

The first experimental demonstration of a negative index of refraction by Shelby et al. included an array of split-ring resonators.[She01] Johnson et al. did extensive research on split-ring based LHM in the infrared.[Joh06] 3D-simulations of their split-ring shown in Figure 3-13 are performed to visualize the LHM-effect. Unlike the simulations at 300 GHz, simulation results in the infrared depend much stronger on material parameters, especially due to the lower conductivity. The structure partially shows a wave-front propagating "backwards" but most of the radiation is naturally transmitted. Anyhow, the work describes the ability of semiconductors and metals to be used for metamaterials in the infrared.[Joh07/this work]

4 Biochip Design

The design of the biochip being the key component of the THz-biosensing technology is presented in this chapter. First an introduction to the 3D full-wave simulation software HFSS is given and the materials' THz-properties are derived. The chip parameters such as resonator measures, substrate, and array configuration are discussed and the optimal position for sample material deposition is found. Different series of biochips are developed combining different substrate materials (PET, silicon, quartz-glass), target frequencies (300 GHz, 600 GHz), and polarization symmetries (LP, ZS). After a description of the manufacturing process the chapter closes with an experimental verification of the linear scalability of a split-ring FSS.

The biochip is the interface between sample and THz-radiation. It converts material properties of DNA and other dielectric samples into changes of the biochips spectral response which is measured. From a practical point of view the biochip design and the spectroscopy setup configuration are desired to be independent of each other, so that any setup can be combined with any biochip, and both can be developed and optimized independently. If the THz-radiation is emitted and propagating freely through space, it passes through planar sensors such as the biochip, thus "reading" them. It is common to guide the emitted THz-radiation in a quasi-optical THz-beam utilizing parabolic mirrors or dielectric lenses. This guidance ensures that all emitted radiation propagates between THz-emitter and -detector. The beam is focused on the sensor device to drive small operational areas and maximize S/N. Integrating emitter and detector on a sensor device increases the unit price significantly, while the FSS-based biochip is a low-cost product thus enabling single-use application. The macroscopic design and handling of these chips is similar to present analysis technologies, which should aid bringing this technology to the market.

The design of the biochip is developed in several steps, beginning with the concept of a frequency selective surface made of split-ring resonators. For each development step numerical simulations with the commercial software HFSS are performed to maximize the sensitivity. A high sensitivity requires a steep edge in the resonator's resonance feature and a strong frequency shift due to dielectric loading. The latter requires a maximization of the field / sample interaction efficiency. Contrary to the idealized theory in chapter 3.2, the biochip has to be designed with realistic material parameters, such as conductivity (chapter 3.3) and substrate (chapter 3.4), and the manufacturing capabilities have to be taken into consideration.

4.1 Simulations with HFSS

The numerical simulations in this work are performed with the software 'HFSS' from Ansoft (since 2010 part of Ansys) versions 10 to 13. HFSS solves Maxwell's Equations in the frequency domain. Given a three-dimensional model with material parameters, defined boundary conditions, and field excitation it computes the electromagnetic fields of the model.

HFSS employs a numerical solver technology based on the finite element method which, in general, follows four steps: discretization of the model in finite elements, selection of interpolation functions, formulation of the system of equations, and solving the system of equations.[Jin]

The first step in the HFSS solution process is the discretization of the model in tetrahedron-shaped finite elements. Generating the mesh being a 3D-grid of tetrahedra is the challenging part of the simulation of the proposed biochip. Reason for this is the adaptive solution process in which HFSS maximizes the computation efficiency. The tetrahedra can be configured in different sizes. They have to be smaller than wavelength to simplify the solution equations and their edges must not exceed the dimensions of adjacent model parts to apply boundary conditions. With nanometer-thin samples the smallest tetrahedra are also a few nanometers in size only. However, the free space above and below the biochip is more than half a wavelength in height, to reach into the resonator's far-field. Dividing the full model space of several hundred micrometers into nm-small elements results in a prohibitive amount of data exceeding the memory of the available computers[I] and therefore in unfeasibly long computation times or program abortion. The adaptive solution process computes several solutions refining the mesh from one try to the next. In regions adjacent to small model parts or strong changes of the fields, such as the sample in the E-field concentration of the resonator, the tetrahedron size is reduced. On the other hand, regions of large parts and small field quantity changes, such as the vacuum above and below the biochip, are meshed with large tetrahedra sized up to several hundreds of micrometers (maximal one third of the wavelength, to assure correct solution modes). This adaptive meshing enables a very good approximation of the detailed part of the simulation while reducing the hardware requirements efficiently.

The simulation of the biochips is done to quantify the shift of the resonant frequency of a resonator upon loading it with dielectric material compared to the unloaded case. This comparison requires identical models and meshes for both simulations, loaded and unloaded case. Therefore the loading is always modeled but the material is set to vacuum for the unloaded case and the mesh of the loaded simulation is reused. The field quantities are noted at the vertices and in the middle of the edges of each tetrahedron. Depending on the complexity of the model and the relation from model size to wavelength different interpolation functions are used applying 6, 20, or 45 unknowns per tetrahedron.[hfss] The solution equation is then assembled from excitation vector, boundary conditions and the solution matrix being a combination of the basis functions of all elements.

The absolute values inhibit a certain error which is kept below 2% by verifying the overall energy in the simulated model. As long as the square sum of the output S-parameters differs from the input power more than 2%, the mesh is refined and an additional solution step is computed. Different HFSS versions are used for the simulations in this work and the mesh algorithm is developed from version to version sometimes resulting in slightly different

---

[I] The computers used are a single-core Athlon64 workstation with 4 GB RAM and Windows XP x64 Edition and a server with two Dual-Core Xeon CPUs, 32 GB RAM and Windows Server 2003 64bit.

absolute values for the same model. This uncertainty is acceptable, especially since the model is idealized in several details, which also might result in a deviation of the absolute value. HFSS is a powerful software package and for example able to handle nanometer-thin layers at millimeter-long wavelengths. However, a few inaccuracies remain. The biochips are partially structured by wet-etching resulting in curved edges. Since the exact shape of the curvy edges is not known the edges are simulated with idealized orthogonal shape. Additionally, surface roughness of the materials, such as gold and silicon, although known, is not taken into account. Both aberrations are acceptable, for they are significantly smaller than model dimension and wavelength. Modeling them would be unreasonably cumbersome in terms of effort and infrastructure. Anyway, an exact modeling is impossible due to the statistic distribution of the etching and surface roughness.

One limitation of hard- and software leads to a systematic error made in the simulations. The biochip is designed as a resonator array, but in HFSS only one resonator is modeled. By applying periodic boundary conditions to the lateral sides of the model, an infinitely large array is assumed. With this setup the resonator and especially the interaction of the fields with the sample can be investigated. Edge effects of a real finite array are neglected for the development of the biochip. In a separate simulation set an investigation of the edge effect is performed in chapter 4.6.2 proving the acceptability of this simplification. The excitation driving this periodic model also has to be periodic. A plane wave at perpendicular incidence is chosen, because it very well resembles the focused THz-beam in the focal point, again neglecting edge effects.

HFSS was designed as a tool for developing high-frequency products, such as antennas, connectors, and printed circuit boards (PCB). An assistive feature for the simulation of frequency selective surfaces was implemented in version 10 for the first time providing the S-parameters of periodic structures. The materials database clearly verifies the target audience being developers, not researchers. Almost all material parameters have been measured at 9.4 GHz and many are commercial PCB materials. Since microwave materials are usually specified by their permittivity and loss tangent[Pozar] the required materials for the simulations have been added to the database in this way with values measured at THz-frequencies taken from publications.

4.2 Simulation Parameters for DNA

The most significant aspect in the research on the biochips is the reaction on loading the resonator with DNA. Size and position of the DNA film are carefully chosen in the simulation model. Unfortunately the material parameters for DNA are not well known. Hence, the most significant aspect of this research is also the greatest uncertainty adding an experimental character to this work.

Measurements of the complex permittivity of DNA have been performed by various research groups from approximately 1 Hz to 70 GHz, showing stable values above 10 kHz, but indicating a strong change at 10 GHz.[Höl08] Additionally, the measurements summarized in

[Höl08] have been performed with DNA in solution, whereas the THz-biochip here measures dry DNA strands bound to the surface.

In the THz-regime several approaches for the detection of large biomolecules, such as DNA, proteins, and bacteria, have been investigated.[Mar08] In some work, detection limits and binding detection capability are explored and relations between materials are determined,[Mic02, Men04, Che07] but absolute values for the permittivity or index of refraction are not attained. In other work, first results from TDS measurements indicate a refractive index $n < 1.5$ with a strong dependency on humidity and a moderate declining with rising frequency.[Mar00] Reproducible TDS measurements on 30 µm thick layers of dried DNA on sapphire substrate confirm these results,[Bru00] as plotted in Figure 4-1. The error increases towards lower frequencies limiting the reliable results to values above 600 GHz. In other work, using different DNA strand, much higher values around $n \approx 1.7$ are determined by the same measurement technique for frequencies of approximately 300 GHz to 700 GHz.[Par05]
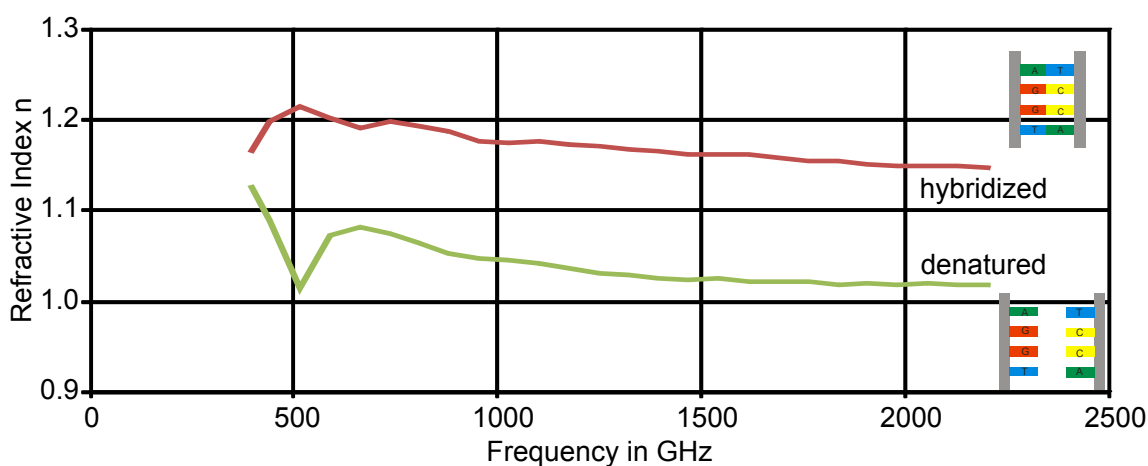
Figure 4-1 (data from [Bru00]): Real part of the refractive index of hybridized (red) and denatured (green) DNA, measured with THz-TDS.

Smaller amounts of DNA have been detected with a stripline dipole resonator, by shifting the resonant frequency by 20% upon a 80 nm thin loading.[Nag02] Simulations of this measurement configuration, assuming the refractive index shown above, do not agree with the results from [Nag02].[Bar03] No measureable frequency shift is expected from the simulation for the same configuration. Raising the DNA layer thickness by a factor of 375, results in a 3% shift. Thus, the measured shift is approximately 2600 times larger than the simulated. A possible reason would be a high conductance of thin films, which was actually reported along a strand to be 100 kS/m in a DC measurement.[Fin99]

A sensor based on a stripline racetrack resonator was presented in [Nag03] by the same group as the stripline dipole. In contrast, the racetrack is functionalized, which means that DNA is bound to the metal surface of the resonator only, whereas the dipole was loaded with a bulky film covering more area than the resonator. The racetrack resonator shifts approximately 1% due to loading with 20 basepair long DNA. This is a much lower shift than those of the dipole, but the amount of sample material was reduced by approximately the

same ratio as the shift, resulting in an identical sensitivity and therefore indicating approximately identical properties for bulky and functionalized DNA-films.

Film Thickness (resembling 20 basepairs)	t_{DNA} = 100 nm
Permittivity	$\varepsilon_{r,DNA}$ = 2.6
Dielectric Loss Tangent	$\tan\delta_{DNA}$ = 0.001
Conductivity	σ_{DNA} = 100 kS/m

Table 1: Electrical properties of DNA as used in the HFSS simulations.

Since the correct values cannot be obtained, an alternative way for estimating the DNA influence is chosen. The racetrack resonator is simulated varying the sample thickness and permittivity. The simulations do not agree with the measurements. A 1% resonant frequency shift is seen for a 1 μm thick layer with a permittivity of $\varepsilon = 4$. In accordance with this, in [Nag03] the resonator's reaction on a covering with a 1 μm thick film of photo-resist is measured and simulated. The resulting frequency shift caused by this polymer layer is comparable to the shift caused by the thin DNA film. Combining own simulation experience with private discussions with authors of [Nag03] leads to a compromise for the DNA simulation parameters, listed in Table 1. The DNA film is modeled significantly thicker, allowing for a better combination with the comparably large wavelength. Permittivity and dielectric loss are adapted to polymer properties. Different simulations are performed for DNA with and without conductivity. Actually, the conductivity overrides the dielectric effect, as plotted in Figure 4-2. The simulations which state to compare the empty chip with "DNA loading" are performed with the parameters given in Table 1.
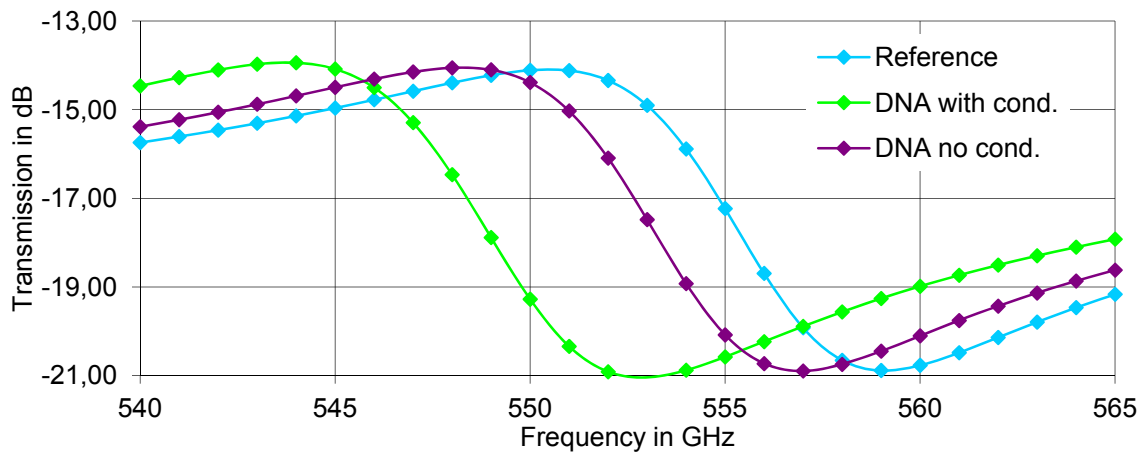
Figure 4-2: Simulated transmission of a complementary aDSR based biochip (blue) with sample material DNA as specified in Table 1, modeled with (green) and without (purple) conductivity.

These considerations culminate in the fact that, as already mentioned in chapter 2, the detection of a DNA film is practically the detection of a dielectric thin-film. Therefore, some simulations to evaluate the sensitivity are made with polymer (PET) loading and the technology is validated with a measurement of a thin PMMA film.

4.3   The Asymmetric Double-Split Ring Resonator (aDSR)

The asymmetric double-split ring resonator (aDSR), as introduced in chapter 3.2, is the starting-point for the biochip development. The biochip characteristic is almost entirely defined by the resonator dimensions, while the array influence is chosen to be comparably low as discussed in chapter 4.6. The design parameters of the aDSR depicted in Figure 4-3, are optimized for a maximal steepness of the flank in the dual resonance feature DRF (Figure 4-4) with regard to technical capabilities. All parameters are analyzed by HFSS simulations and selected results are discussed in the following:
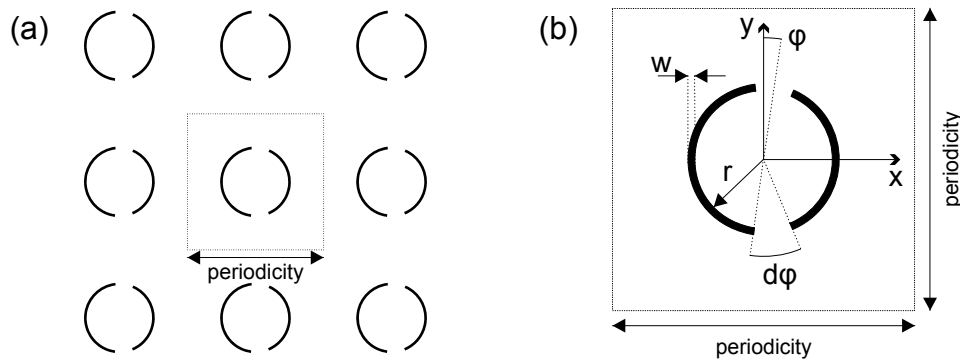
Figure 4-3:[Deb07/this work] (a) Schematic section of the first version of the aDSR FSS and (b) one resonator with denotation including radius r, gap offset angle φ, gap angle dφ and arc width w. The structure consists of conductive arcs (black) in vacuum.

The ring radius r is the central parameter for adjusting the resonant frequency. A wavelength equal to $2\pi \cdot r$ corresponds to a frequency between the base-mode and the DRF. For initial research it is set to 50 µm corresponding to approximately 1 THz. The distance depends strongly on the gap angle since the resonance is proportional to the arc length. Hence, varying the gap angle dφ moves the DRF along the frequency axis. The shape of the feature is hardly affected. Increasing the gap angle from 10° to 40° increases the height of the DRF flank from 11.2 dB to 17.5 dB, as shown in Figure 4-5(a). The steepness has its maximum at 20°. Larger angles make a more moderate steepness while smaller angles reduce the height only. Figure 4-5(b) shows the maximum of the absolute value of the DRF's derivative, for different gap angles normalized to the value of the 20° version.
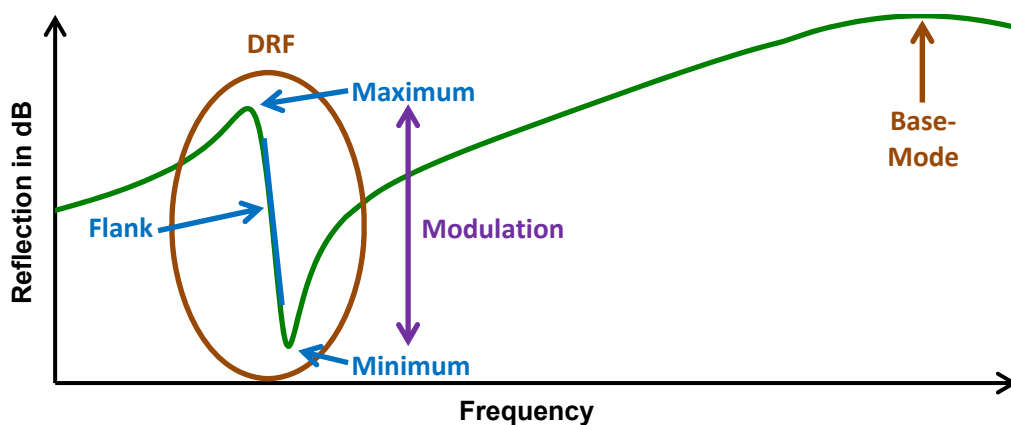
Figure 4-4: General reflection spectrum of the aDSR with resonance feature denotations.
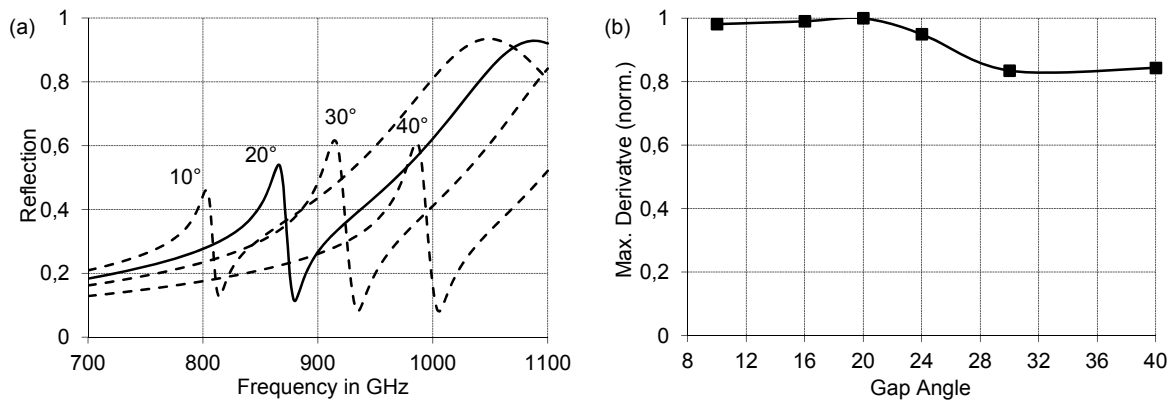
Figure 4-5: Optimization of gap angle dφ: (a) Reflection DRF and (b) highest steepness of the DRF flank (maximum derivative $-\partial R/\partial f$) for different dφ.

The offset angle has a much stronger effect on the DRF. For $\varphi = 0°$ the structure is symmetric and the DRF is not excited at all. Increasing this angle causes the feature to appear right away. The modulation increases constantly but the steepness exhibits a distinct maximum for an angle of 4°. A large offset angle separates the arc's resonances. Therefore they are developed stronger but with a higher distance in frequency, resulting in a higher modulation but lower steepness. Figure 4-6 shows the DRFs for different offset angles φ and the maximum of the absolute value of the DRF's derivative normalized to the 4° version.
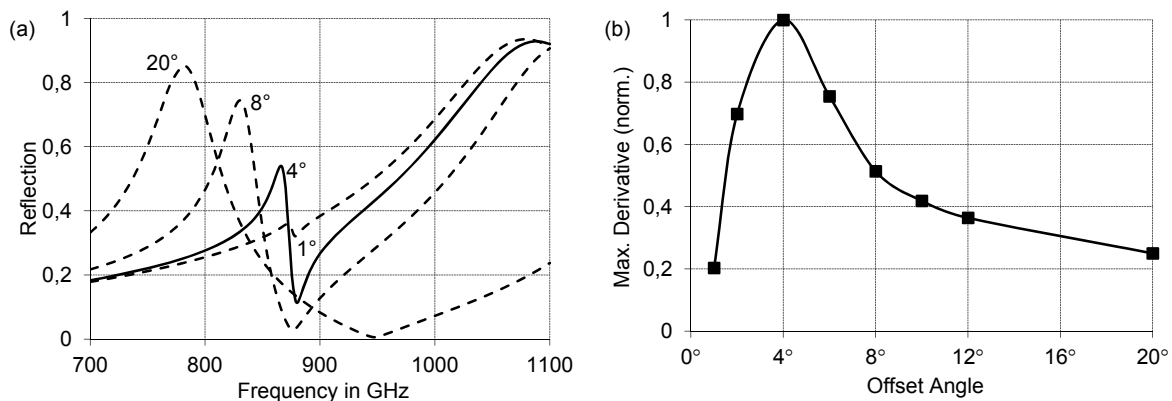
Figure 4-6:[Deb07/this work] Optimization of offset angle φ: (a) Reflection DRF and (b) highest steepness of the DRF flank (maximum derivative $-\partial R/\partial f$) for different φ.

Metal thickness and width of the arcs are determined by several considerations. From a theoretical point of view a perfectly conducting infinitely thin wire would be optimal. For practical reasons gold is chosen as conductive material, as discussed in chapter 3.3. On the one hand it is suitable to have a high thickness enabling a high current. On the other hand a thin metal layer can be treated as a two-dimensional structure. Gold is deposited on dielectric substrates by sputtering and electron beam vaporization, respectively. These physical vapor deposition (PVD) technologies deposit homogeneous thin-films with a low surface roughness. However, it is desired to have a thickness larger than skin-depth to receive most of the incident radiation. For highly conductive material the skin-depth δ can be computed from the conductivity by [Pozar]

$$\delta = \sqrt{\frac{2}{\omega\mu\sigma}} = \sqrt{\frac{2}{2\pi f \mu_0 \sigma_{AuTHz}}}. \tag{4-1}$$

For a lowest system frequency of 200 GHz the corresponding skin depth $\delta = 178$ nm. The biochip is actually built with 200 nm providing sufficient conductivity along the aDSR arcs. Compared to wavelength this thickness is extremely small. The FSS can therefore be assumed to be a surface feature at the interface of substrate and air. The effective refractive index approximation (chapter 3.4) is valid and there will be no resonance mismatch between front and backside such as with the thick-layer metal hole arrays (chapter 2.3).

The line width w of the rings is desired to be narrow, but it is determined by technological limitations. The radius r of the split-ring is actually the inner radius of the metal line, corresponding to an inner circumference which defines the resonant wavelength. The outer circumference of an arc with the same angles is larger, thus corresponding to a larger resonant wavelength. The effective resonance is a superposition of all resonances appearing within the metal line. Therefore, the wider the line becomes the broader the resonance will be. Limited by the available photo-lithography and lift-off technology, the line width was determined to w ≥ 5 μm for the positive aDSR structures.

4.4 Substrates

A FSS made of a 200 nm thin gold layer requires a substrate for mechanical support. The influence of a dielectric substrate is discussed in chapter 3.4. It is advantageous to use a material with a low permittivity to maintain the DRF steepness. The effect of the substrate on the frequency spectrum of the free-standing FSS is taken into account by the effective permittivity ε_{eff} being the mean value of substrate and air permittivities:

$$f_{substrate} = \frac{f_{freespace}}{n_{eff}} = \frac{f_{freespace}}{\sqrt{\varepsilon_{r,eff}}} \tag{4-2}$$
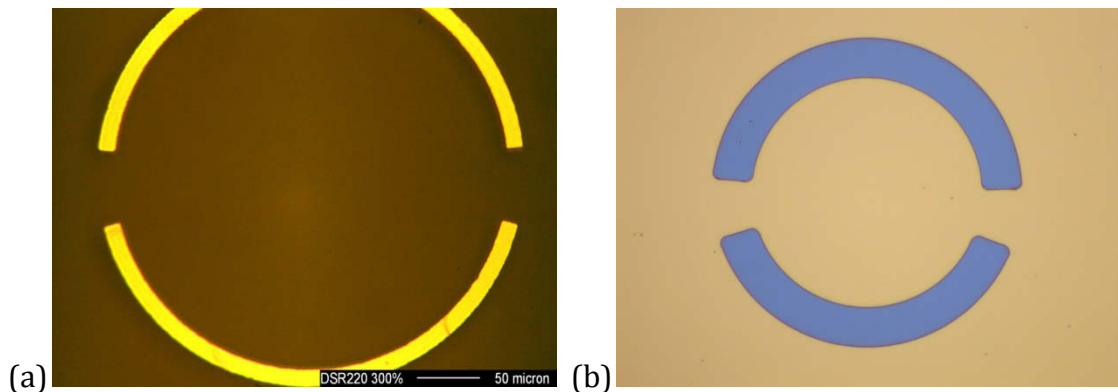
Figure 4-7: Microscopy picture of (a) an aDSR on PET- foil with 150 μm radius and 15 μm width and (b) a complementary aDSR on silicon wafer with 56 μm inner radius and 20 μm width.

The first series of aDSR FSSs is produced on PET-foil as discussed in appendix-chapter 8.3. PET has a comparably low permittivity $\varepsilon_{PET} \approx 2.2$.[Pozar] An aDSR with the DRF at 240 GHz is

shown in Figure 4-7(a). The sharpness gradient in the picture is a result of undulation of the foil caused by heating for lithography steps. The poor mechanical stability of these FSS on PET disqualifies this technique for commercial biochip application.

Better mechanical durability is achieved on silicon substrates due to the comprehensive experience in producing gold structures on wafers. The structure size is half of the size on PET for the same resonant frequency. This is advantageous in means of sensitivity, since a smaller amount of sample material is required with a smaller resonator. Figure 4-7(b) shows a complementary aDSR of the second series with the DRF at 270 GHz. At the Institute of Semiconductor Electronics, RWTH Aachen, the technology for manufacturing the biochips is developed for silicon substrates first. Then it is transferred to quartz-glass because three significant considerations disapprove silicon: Commercially it is a matter of cost. High-resistivity silicon is more expensive than quartz-glass, more than twice as much for the wafers used in this project. From a research point of view quartz-glass is advantageous for inspection. With the optically transparent glass the interface between metal and substrate can be inspected. The undercut feature which is discussed in chapter 4.5 enables the deposition of sample material on the interface side of the gold layer. This can optically be inspected through the glass substrate. Additionally, the optical transparency is advantageous for the manufacturing technology. Lithography exposure is done from the backside of the biochip utilizing the metal layer as the mask, as discussed in chapter 4.8.

Quartz-glass (fused silica) being the amorphous form of quartz is chosen as substrate material for the biochip. The integration of different polarization directions on one biochip requires the use of an isotropic material, disqualifying crystalline quartz whose birefringence properties[Cas09] are in the order of permittivity variation of DNA hybridization states[Bru00]. The material properties of quartz-glass are approximated for the 200 to 500 GHz region from [Gri90] which are in good agreement with more recent measurements[Naf07]:

Permittivity	$\varepsilon_{r,glass}$ = 3.81
Dielectric Loss Tangent	$\tan\delta_{glass}$ = 0.0001

Table 2: Material properties of quartz-glass for the lower THz-regime.

In addition to the reflection / transmission properties of the aDSR the biochip's spectral behavior is influenced by the impedance mismatch of substrate and air. A wave impinging on a surface of a dielectric material is partially reflected. This reflection can be strong enough to cancel the minimum of the DRF by overlapping. But since the strength of the reflection is depending on frequency this interaction can be avoided to separate the DRF caused by the resonator from the substrate reflection: A lossless dielectric layer is invisible to radiation for a thickness equal to multiples of half the wavelength of the radiation inside the material and has the highest reflection for odd multiples of quarter the wavelength.[vHipp] Hence, a low loss dielectric such as quartz-glass will have a good reflection minimum with a thickness equal to one half of the wavelength. In regard to the frequency spectrum of the developed reader system (chapter 5.3) the DRF center frequency is defined as 280 GHz. The optimal substrate thickness d_{quartz} is

$$d_{quartz} = \frac{\lambda_{quartz}}{2} = \frac{\frac{c_0}{\sqrt{\varepsilon_{r,quartz}}}}{2 \cdot f} = \frac{\frac{c_0}{\sqrt{3,81}}}{2 \cdot 280\text{GHz}} = 274\mu\text{m} .$$

(4-3)

Glass slides with this low thickness are difficult to handle because they can easily break. For cost-efficient biochips the commercially available standard size of 500 μm is chosen. This thickness is close to the second best theoretical value of 548 μm. Alternatively available 750 μm thick slides are much closer to 5/4 of the wavelength at 685 μm and are therefore unfavorable.

4.5 <u>Sample Position and Complementary FSS</u>

In the surface plane the E-field distribution of the aDSR in resonance shows a strong concentration close to the arc ends, as discussed in chapter 3.5. To maximize the effect of a sample on the resonant frequency it is deposited here. A closer look at the cross-section reveals a large part of the E-field being inside the substrate. Figure 4-8(a) depicts arc ends on substrate and the capacitance distribution in analogy to a parallel-plate capacitor (with plate area A and distance d) with capacity [Böhme]

$$C_{pp} = \varepsilon_0 \varepsilon_r \frac{A}{d} .$$

(4-4)

The capacity C_{slot} is marginal. Simulations show that a dielectric thin-film deposited here has almost no effect on the resonance due to the low amount. The capacitance, and therefore the E-field, is almost entirely distributed above the metal and below in the substrate. The capacity scales with the permittivity of the material between the plates, or here the arc ends, as equation (4-4) states. With the given symmetry the capacity $C_{substrate}$ is 3.81 times larger than C_{air} and thus only 21% of the E-field is accessible for sample interaction on the top side. An approach to utilize the field concentration below the metal is shown in Figure 4-8(b) introducing the undercut. The substrate is partially removed below the metal leaving the arc ends standing free. Now the sample is deposited at the bottom side of the metal where the larger part of the E-field is, thus increasing the effect on the resonant frequency.
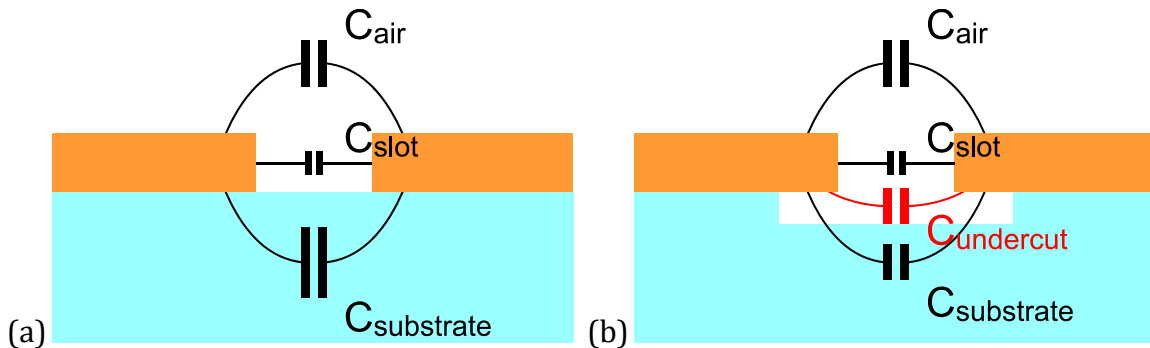
Figure 4-8: Cross-section of the gold FSS (orange) on quartz-glas substrate (blue) with capacitance distribution between arc ends (a) without and (b) with undercut.

The undercut is desired to bare a few micrometers of the lower side of the metal. For a reproducible result the undercut technology is applied to the whole surface. But if the substrate is removed under all metal edges for e.g. 3 μm, a split-ring with 5 μm width is fully

removed from the surface. At this point the development of the biochip discontinues on the positive structure of metal rings, but changes to the complementary structure of ring-shaped apertures in a metal surface. The mechanical stability of the complementary structure is much higher and the undercut feature can be realized. Due to the Babinet Principle all properties can be transferred from the positive FSS, as discussed in chapter 3.6, exchanging E- with H-field polarization direction and transmission with reflection. The transfer of the aDSR from positive to complementary version deviates from the theory due to finite metal dimensions and substrate influence. The new structure is reinvestigated and optimized for a high frequency shift due to dielectric loading in the undercut. The principal design is maintained but the gap angles change to $\varphi = 8°$ and $d\varphi = 22°$.

(a)   (b)
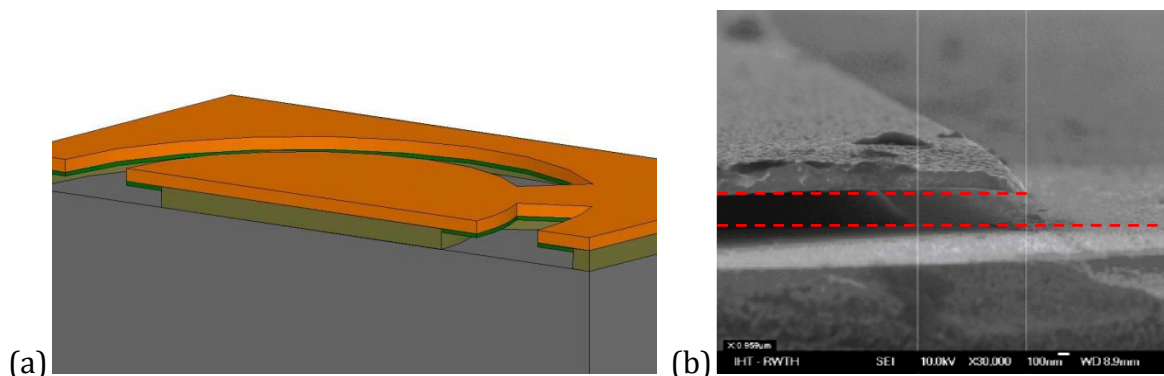
Figure 4-9: (a)[Deb09/this work] Cross-section through a complementary aDSR with undercut on silicon substrate (gray) with oxide layer (SiO_2, brown), metal layer (orange), and sample (green) deposited on the bottom side of the metal. (b) REM picture of the cross-section indicating a 1 µm wide undercut between the vertical white lines. The red dashed lines identify the material layer interfaces.

The second series of biochips is produced on high-resistivity silicon. An Oxide layer is added between substrate and metal to realize the undercut. The structure is shown in Figure 4-9(a) depicting a cross-section of a single aDSR. The high quality of the manufacturing result is seen in the REM picture in (b) with red dashed lines at the material interfaces.

The corresponding DRFs are plotted in Figure 4-10. The aDSR is simulated with two different undercut sizes, 6 µm and 3 µm. Both simulations are performed without and with DNA loading. The results show a strong frequency shift of 8 GHz for the larger undercut. Reducing the undercut and thereby the amount of DNA by half results in a frequency shift of 7 GHz, which is still almost as much as with the double amount of sample material. This comparison confirms the strong concentration of the E-field close to the resonator and proves a 3 µm undercut to be large enough for detection.[Deb09]
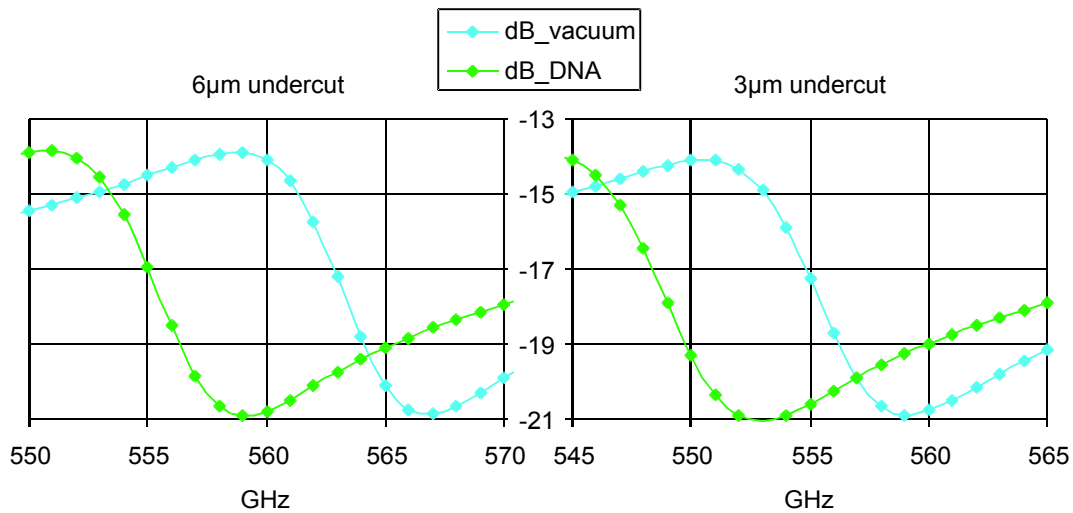
Figure 4-10:[Deb09/this work] Simulated transmission DRF in dB of complementary aDSR biochips (half size: 560 GHz version) on silicon substrate with (green) and without (blue) DNA deposited in the undercut. The frequency shift due to loading of the biochip with a 3 µm wide undercut is almost as large as for the 6 µm undercut.

The third series of biochips is designed on quartz-glass substrates (and with a varied array configuration, as discussed in chapter 4.6). Again, the undercut feature enhances the sensitivity if the sample is deposited there. A cross-section of one aDSR is shown in Figure 4-11 with quartz-glass substrate (blue) and gold conductive layer (orange). The picture also shows two chrome layers (gray). A 10 nm adhesive layer, which is required for technical reasons (chapter 4.8), is inserted between glass and gold. Additionally, a 10 nm cover layer is added to the biochip design. The latter one covers the top gold surface making the gold layer accessible in the undercut and at the aperture edges only. DNA as the sample is deposited on the biochip by functionalization (chapter 6.3.1) being the chemical bonding of DNA strands to an open gold surface. With most of the gold covered by chrome this functionalization is taking place on the bottom side of the gold layer in the undercut and on the aperture edges only. Since the DNA is deposited on the biochip at certain locations only, this technique is called localized functionalization.
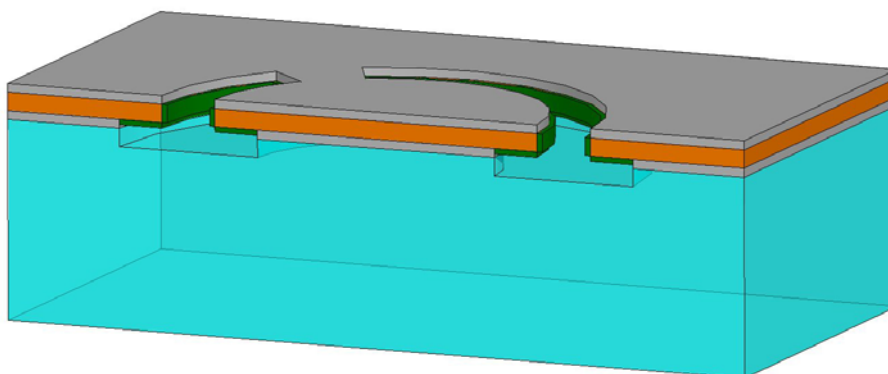
Figure 4-11: Cross-section through a complementary aDSR with undercut on quartz-glass substrate (blue) with gold layer (orange), chrome adhesive and cover layers (gray) and DNA (green) deposited at the bare gold surface. (Layer thicknesses are not true to scale).

The E-field concentration close to the split-ring, as discussed in chapter 3.5, is found again with this complementary structure. A full surface coverage of DNA has approximately the same effect on the resonant frequency shift as a 3 μm wide covering along the aperture edges. The DRF at 280 GHz is shifted 1.6 GHz. Actually with the full surface covering the shift is a little smaller due to the lower surface conductivity. The undercut improves the shifting effect on the DRF as plotted in Figure 4-12. The DNA deposition in the undercut, plotted in green in Figure 4-11, causes a DRF frequency shift of 2.1 GHz which is one third greater than the identical deposition on the top side (orange) of the gold does.
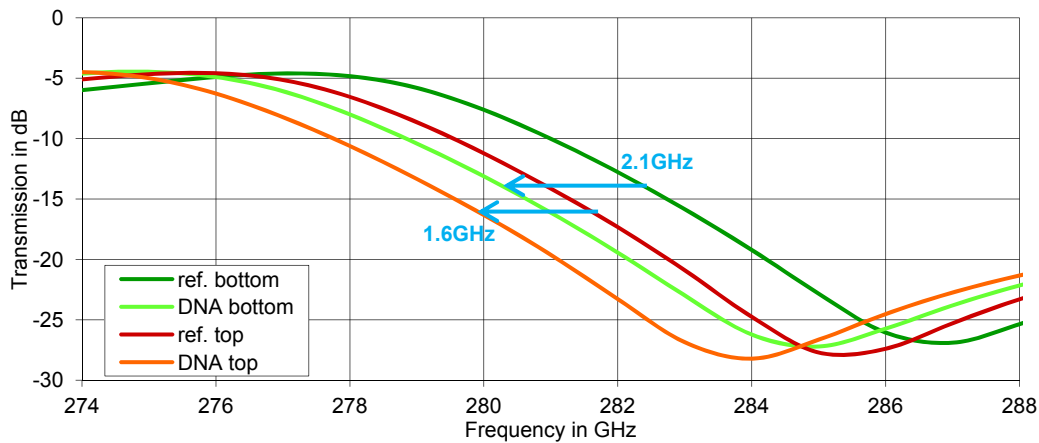
Figure 4-12: Undercut sensitivity: A DNA deposition on the bottom side (light green) of the metal shifts the reference DRF (dark green) 2.1 GHz. An identical deposition on the top side (orange) of the metal shifts the reference DRF (red) 1.6 GHz only. The references deviate due to different FEM meshes for the simulations.

The dimensions of the final biochip design are summarized in chapter 4.7 from which the sensitivity can be derived. The gold layer of the quartz-glass based biochip has an accessible gold surface on the bottom side and the layer edge of $4.73 \cdot 10^{-9}\,\mathrm{m}^2$ per resonator, corresponding to an amount of 0.4 fmol of DNA, as discussed in chapter 6.3.1.

4.6 <u>FSS / Array Design</u>

All resonator parameters discussed above are accountable for the shape and size of the DRF and are optimized for a high resonant frequency shift caused by localized dielectric loading. Two more degrees of freedom exist according the arrangement of the unit cells. The periodicity being the side length of a unit cell and the overall rotation of the ring around its center affect the coupling between neighboring elements and the frequency of Wood's Anomaly.

The optimal periodicity of a FSS is a compromise of sharpness and strength of the resonance. With a smaller periodicity the resonators are closer together. The interaction between neighboring resonators is stronger which reduces the sharpness of the DRF and weakens the E-field concentration. Positive structures are predominantly capacitively coupled along polarization direction, resulting in a lower resonant frequency with lower distance. The corresponding effect in the complementary structure is inductive coupling of the apertures. Hence a sharp resonance requires a large periodicity. The fill-factor on the other hand

describes how many resonators are present in the vicinity of the exciting radiation. With fewer resonators per area more radiation can pass the FSS without being affected. This results in less distinct minima in the transmission spectrum. Hence a strong resonance requires a small periodicity.
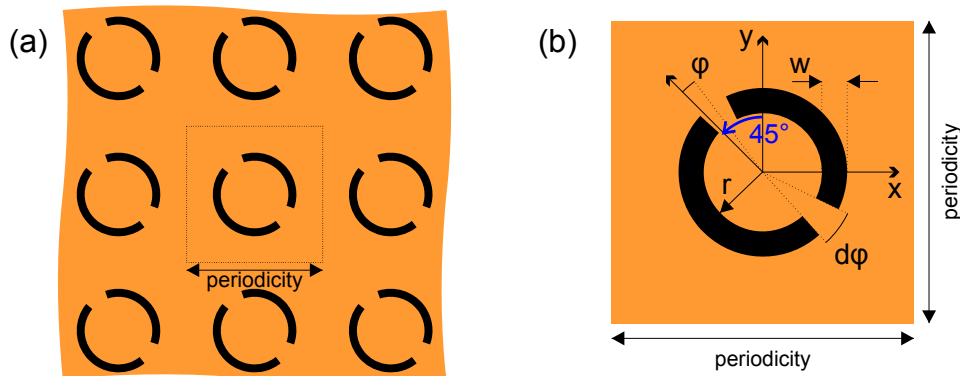
Figure 4-13: (a) Schematic section of the final version of the complementary aDSR FSS and (b) one resonator with denotation including radius r, gap offset angle φ, gap angle dφ and arc width w. The design is rotated counter clockwise by 45° compared to the first version (Figure 4-3) and has slightly different parameters. The structures are slits (black) in a gold layer (orange) on quartz-glass.
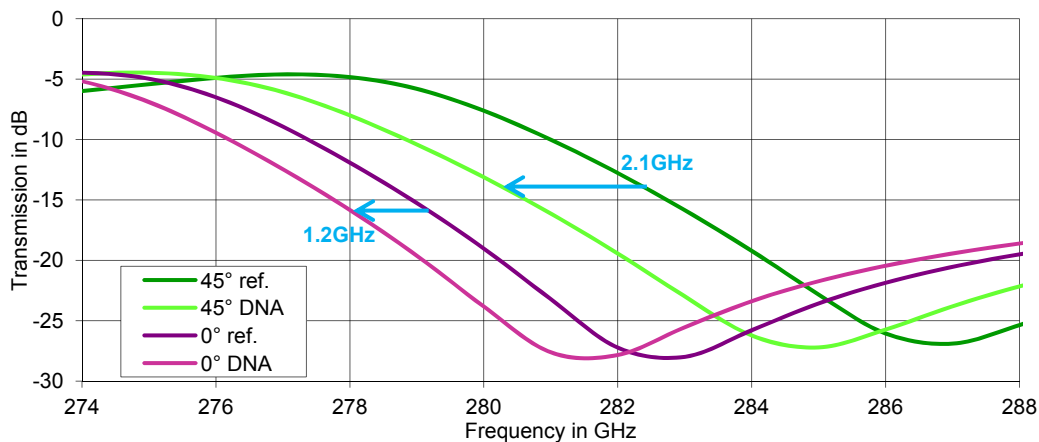
Figure 4-14: DRF of the complementary aDSR FSS with aperture orientation along (purple) and 45° off (green) the grid orientation.

Contrary to the initial positive aDSR FSS shown in Figure 4-3 the final complementary version has the resonators rotated by 45° as depicted in Figure 4-13. The excitation plane wave is magnetically polarized along the aperture arcs, in accordance to the Babinet Principle. Because of this rotation the distance to neighbor elements in direction of polarization is larger. Therefore the coupling between these neighbors is weaker and the DRF appears at a higher frequency. In the rotated pattern the neighbor elements in direction of the unit cell periodicity are closer than the diagonal ones of the initial structure. Coupling between the closer elements reduces the sharpness of the DRF slightly. But the overall coupling of one resonator to its neighbors is lower resulting in a stronger frequency shift due to dielectric loading, as shown in Figure 4-14. Apertures oriented along the grid (0°) have a stronger and sharper DRF with 23 dB modulation over 9 GHz, while the 45° rotated pattern has only 22 dB

over 11 GHz. The frequency shift caused by localized deposition of DNA of 1.2 GHz for the 0° pattern is almost doubled to 2.1 GHz with the rotated design.

Decreasing the periodicity to improve the fill-factor will raise the DRF maximum closer to 0 dB but also reduce the steepness. Increasing the periodicity is disadvantageous with regard to Wood's Anomaly which corresponds to the periodic appearance of elements along the polarization direction. Due to the 45° rotation the wavelength λ_{WA} of Wood's Anomaly is a factor of square root of two larger. From the initial FSS the periodicity is rescaled for every development step regarding DRF frequency or substrate refractive index. The final 280 GHz version on quartz-glass has a periodicity of 416 μm. Wood's Anomaly appears at

$$\lambda_{WA} = \sqrt{2} \cdot periodicity \ = \sqrt{2} \cdot 416\mu m = 588\mu m. \tag{4-5}$$

Considering the effective permittivity for the FSS

$$\varepsilon_{r,eff,quartz} = \frac{\varepsilon_{r,air} + \varepsilon_{r,quartz}}{2} = \frac{1 + 3.81}{2} = 2.4 \tag{4-6}$$

results in a frequency of Wood's Anomaly

$$f_{WA} = \frac{\frac{c_0}{\sqrt{\varepsilon_{r,eff,quartz}}}}{\lambda_{WA}} = 330 GHz. \tag{4-7}$$

This frequency is just above the available spectrum of the biochip reader (chapter 5.5). It is unfavorable to have the anomaly in the measured range as it will destabilize the measurement. Therefore the periodicity is not increased.

4.6.1 Polarization

The biochip is designed for a fixed polarization direction. The complementary aDSR structures exhibit the DRF for an impinging plane wave polarized magnetically parallel to the aperture arcs, as depicted in Figure 4-15(a). With an excitation rotated by 90° a different mode is excited and other resonance features appear. In contrast, the center-symmetric (ZS) design shown in Figure 4-15(b) is independent of the polarization direction. The unit cell contains four rings arranged symmetric with respect to the center point. In this configuration the apertures of every second ring only are in direction of polarization. Hence, every second ring only is in resonance at a time, which results in weaker DRF extrema as with a lower fill-factor. Additionally, the stronger coupling of neighbor elements results in a lower resonant frequency. A redesign with closer distance between the resonators and a smaller radius achieves a DRF comparable to the linearly polarized (LP) design. The modulation is reduced but the flank becomes steeper, as plotted in Figure 4-16. The frequency shift due to DNA loading is 1.3 GHz only. Since the polarization of the biochip reader is at a fixed angle the linearly polarized (LP) design is sufficient for the biochip application.
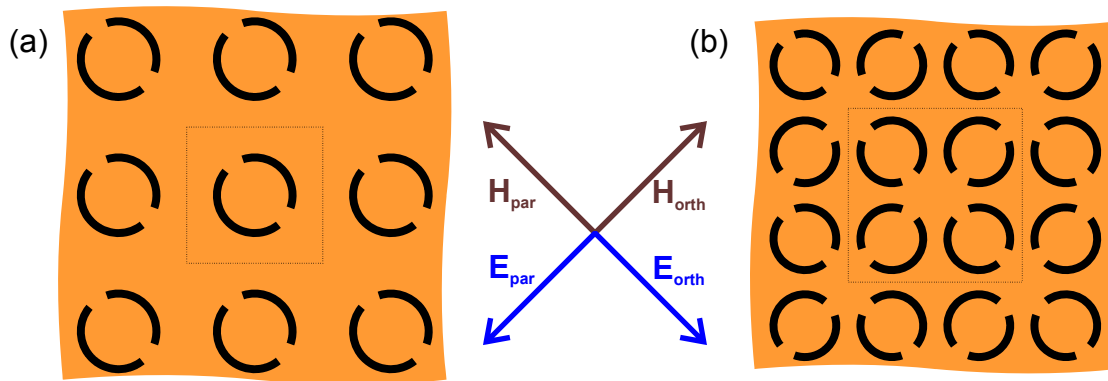
Figure 4-15: (a) Linearly polarized (LP) and (b) center-symmetric (ZS) FSS designs with polarization directions of the incident E- and H-fields (blue / brown arrows).
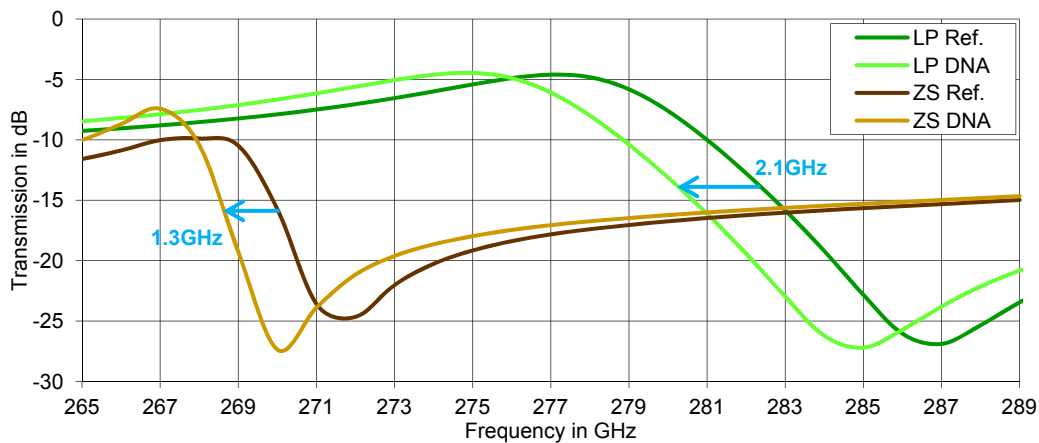
Figure 4-16: DRF of the complementary aDSR FSS with linearly polarized (green) and center-symmetric (brown) arrangement at parallel excitation (H_{par}).

The ZS-design is considered an alternative for local referencing. Several aDSR arrays are separated on each chip for the investigation of different samples. One array is left untreated for the reference measurement. This way of referencing is valid for a homogenous manufacturing result only. If the size of the rings varies over the biochip, e.g. because of lithography or etching time tolerances, the different arrays have differing resonant frequencies. In this case the ZS-design is advantageous. If the parallel oriented rings only are loaded with sample material, the orthogonal oriented of the same array provide a reference at the same position with polarization rotated by 90°. The disadvantage of this technique is the selective material deposition on every second ring only, which requires more effort than the deposition of a full array of resonators. Additionally, DNA functionalization and hybridization require rinsing of the array with water and a buffer solution, respectively. By this, sample material might get into the reference rings thus falsifying the reference. This contamination may be avoided with a separate reference array, but not with alternating ring mapping.

4.6.2 Finite Array

Finally, edge effects have to be considered. The simulations assume an infinite periodic arrangement of FSS unit cells with an infinite plane wave excitation. Technically, the biochip as well as the THz-beam waist, are finite.
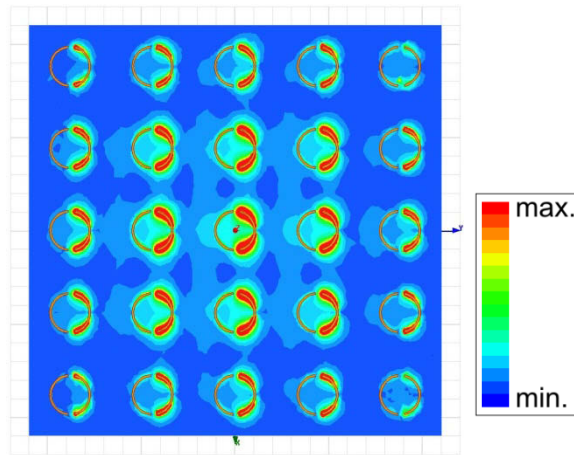
Figure 4-17: E-field distribution on the finite 5 x 5 array (1100 µm square) without substrate by Gaussian Beam excitation at 920 GHz with 500 µm beam waist (FWHM).

If the beam waist exceeds the chip width the radiation partially passes without interaction. Then the resonance feature is smaller because the DRF minimum will be superimposed with the bypassed radiation. If the beam waist is smaller than the chip, all radiation is interacting with the resonators and the spectral behavior is expected to be almost identical to the periodic case. The measurements in chapter 6.1 approve this theory on sufficiently large arrays, whereas the simulation can only be used to investigate small arrays, such as a 5 x 5 array of positive aDSRs without substrate, which are discussed in chapter 3.2.[II] Figure 4-17 shows the E-field distribution of this array for a Gaussian Beam excitation focused on the center of the array with a beam waist at full width half maximum (FWHM) of 500 µm. The 1100 µm square array is more than two times larger. All resonators are excited in the correct mode, shown here at the high-frequency end of the DRF, but with different currents. The circular beam profile can clearly be reconstructed from the strengths of the E-field concentration lobes. The spectral response is similar to the periodic case, as plotted in Figure 4-18, but decreased approximately 6 dB. A part of the radiation passes the array since the resonators at the edge are not perfectly excited.
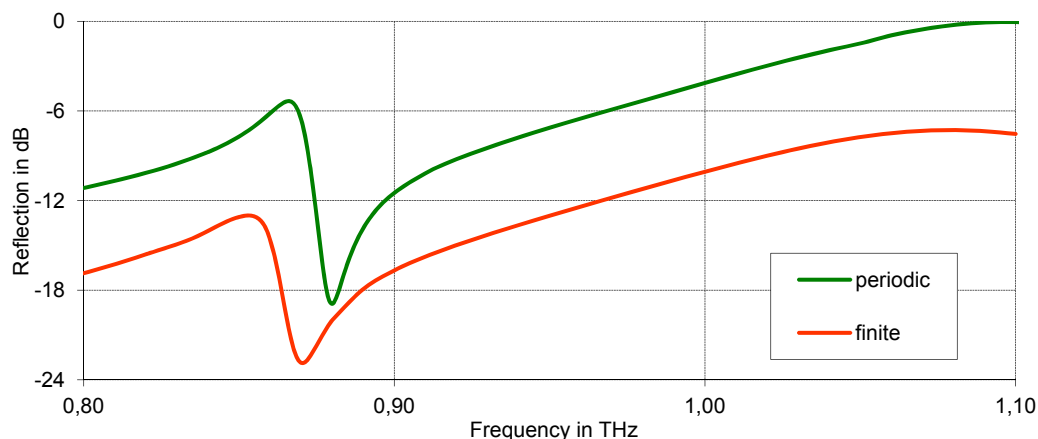
Figure 4-18: Simulated reflection spectrum of the positive aDSR FSS without substrate for the unit cell with periodic boundary conditions (green) and the finite 5 x 5 resonator array with Gaussian Beam excitation.

[II] The simulation of finite arrays requires much larger models and more complex boundary conditions than the periodic case. Thus, unfortunately, the available computers can solve simplified models only.

The FSS frequency response is primarily shaped by the split-ring, however interaction with neighboring elements has significant effect on the shape of the resonance feature, as discussed above. A single aDSR illuminated with a beam of the same diameter as the split-ring exhibits a slightly different spectral behavior compared to the FSS. But an array of 3 x 3 resonators with a corresponding beam size resembles the FSS spectrum good already. For the biosensor it is desired to require as little sample material as possible. Therefore measurement setup is designed to have a narrow THz-beam focus and the active array on the biochip is approximately the same size. With a focus diameter of less than 2.5 mm (chapter 5.4.1) a 5 x 5 array is illuminated with a small part of the beam passing by the chip only. The transmission spectrum shows almost no deviation from the transmission spectrum of an array much larger than the beam.

In addition to Wood's Anomaly, surface waves which are reflected at the edges might propagate back across the finite array. These surface waves are to be considered for some types of antenna array, but not for the split-ring FSS, due to the fact that they require a periodic distance smaller than half the wavelength.[Munk2] For the simulated array they appear below 680 GHz and for the 280 GHz biochip on quartz-glass below 230 GHz, which is, alike Wood's Anomaly, just outside the frequency range of the biochip reader.

4.7 280 GHz Biochip Technology

In total, eight versions of biochips are designed and produced. All combinations of substrates (silicon and quartz-glass), polarization configurations (linearly polarized LP and center-symmetric ZS) and operating frequencies (280 GHz, 560 GHz) are investigated.

(a)   (b)
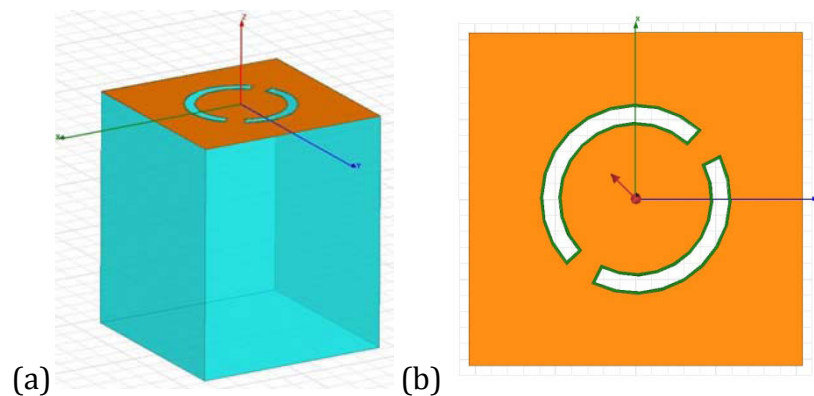
Figure 4-19: HFSS depictions of the aDSR showing (a) a 3D-model of the complementary aDSR in the gold layer (orange) on quartz-glass substrate (blue) and (b) a 2D-image from the bottom side without substrate but with sample (green). The direction of the E-field polarization is depicted in (b) by the red arrow.

The 560 GHz designs are essentially the 280 GHz designs scaled to half the size. Because of manufacturing issues for the biochips and the worse operating stability of the 550 - 600 GHz reader setup, the technology is surveyed at this frequency marginally only in chapter 4.10. The linearly polarized design is optimized individually for both substrates and the center-symmetric design for quartz-glass, with parameters summarized in appendix-chapter 8.2. The silicon based chips are a development step only towards the quartz-glass based chips which

provide a higher usability. The chips for the 280 GHz technology are produced with a sufficient homogeneity rendering the center-symmetric design unnecessary. Hence, the experiments with samples are performed with the DRF at 280 GHz LP only, in the biochip reader setup presented in chapter 5.3 at approximately 240 – 320 GHz.

gap angle	$d\varphi = 22°$
offset angle	$\varphi = 8°$
inner radius	$r = 96$ µm
aperture width	$w = 20$ µm
gold thickness	$t = 0.2$ µm
undercut depth	$ud = 0.5$ µm
undercut length	$ul = 3$ µm
periodicity	$p = 416$ µm

Table 3: Dimensions of the complementary aDSR with undercut on quartz-glass substrate.

Figure 4-19 shows HFSS views on the simulated model. The unit cell is depicted without surrounding elements and boundary conditions. Due to the large aspect ratio the undercut cannot be recognized, but it is clearly displayed in the cross-section figures in chapter 4.8. Corresponding to Figure 4-13 the parameters of this design are listed in Table 3 and the transmission is plotted over the full measurement range of the biochip reader in Figure 4-20.
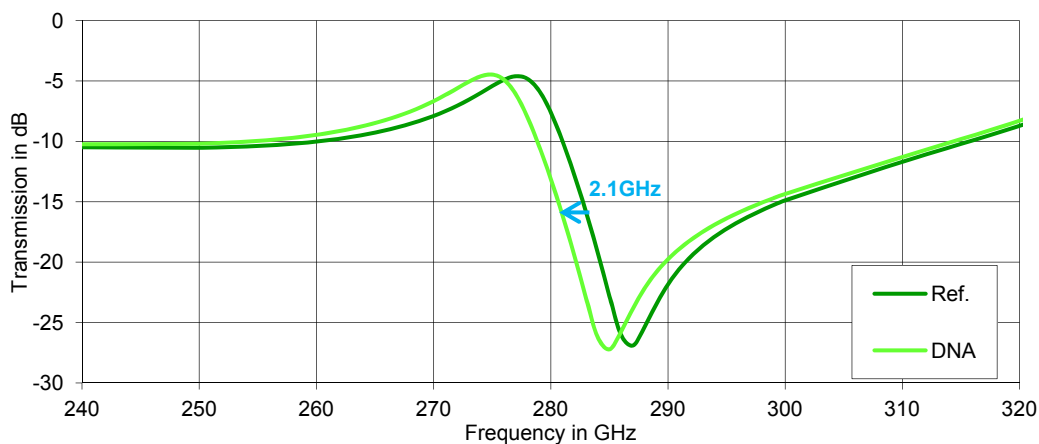
Figure 4-20: Simulated DRF of the complementary aDSR FSS without (dark green) and with (light green) DNA sample.

4.8 Biochip Production Process

The technology for the production of the biochips is developed by a project partner, the Institute of Semiconductor Electronics (IHT) at the RWTH Aachen. The production logs for the silicon and the quartz-glass based chips are included in appendix-chapter 8.3.
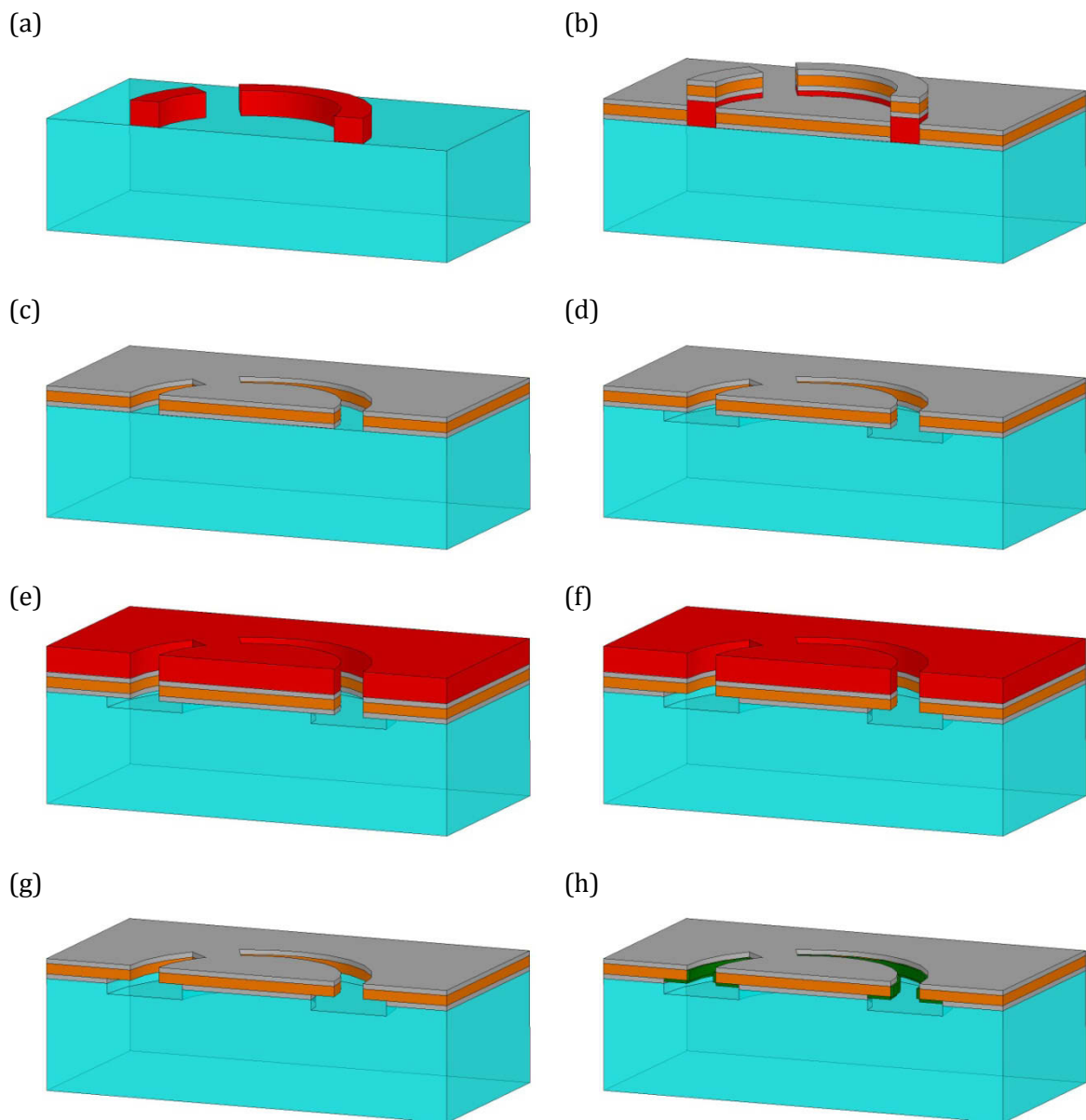
Figure 4-21: Production steps of the biochip depicted at a cross-section (not true to scale) through an aDSR with quartz-glass substrate (blue), chrome (gray), gold (orange), photo resist (red), and DNA sample (green).

The basic steps are depicted in Figure 4-21 with ideally shaped corners and edges. (a) First the positive FSS-structure is deposited in photo-resist on the clean substrate by photo-lithography. (b) Second the metal layers are deposited by electron beam physical vapor deposition (EBPVD / "e-beam evaporation"), which is a simple and common technology to deposit clean thin-films.[Haefe, Irene] Three layers are deposited successively beginning with 10 nm of chrome. This adhesive layer is required to stabilize the gold layer which otherwise does not bind to the substrate strong enough. 200 nm of gold are deposited as conductive metal layer and for DNA functionalization. A second 10 nm chrome deposition as a cover layer prevents the sample DNA from binding on the top side of the biochip. (c) The third step is a lift-off process removing the photo-resist and thereby the metal deposited on it. The advantage of the lift-off over etching is the simplification of the processing step. Only one resist removal process structures all three metal layers at a time. Additionally, steeper and

cleaner edges can be achieved.[Campb] The result is a substrate with a complementary FSS on top consisting of a 220 nm metal screen with aDSR apertures. (d) Step four is a wet etching process of the substrate to generate the undercut below the metal screen. For the silicon chips a separate oxide-layer with a defined 500 nm thickness is generated on the surface. Thus etching will not go deeper into the substrate than 500 nm, but might go farther horizontally generating a wide undercut. On amorphous quartz-glass in general etching is an isotropic process. Therefore the undercut sidewall becomes a slope. By adjusting etchant concentration and temperature the shape of the slope can be affected,[Frans] thus resulting in an undercut being wider than deep. (e) A second lithography process makes step six. Photo resist on the top-side of the chip is exposed from the backside utilizing the metal screen as lithography mask. The exposed part is removed leaving a resist layer on the metallic screen but the undercut accessible. (f) The sixth step is the bearing of the gold surface in the undercut. The chip is wet etched to remove the chrome in the undercut. The cover layer is not affected due to protection by the resist layer on the top-side. Only the edge in the split-ring aperture gets in contact with the etchant. But since the etching lasts only long enough to remove the 10 nm thin adhesive layer the cover layer edge will not be harmed more than this. Compared to the 3 µm wide undercut these 10 nm can be neglected. (g) After removing the resist from the topside the biochip production is finished. (h) Finally, the DNA sample material is deposited on the chip by the technique of localized functionalization (chapter 6.3.1). Prepared with a special linker the DNA connects to the gold surface only, even if the chip is fully dipped in sample solution.
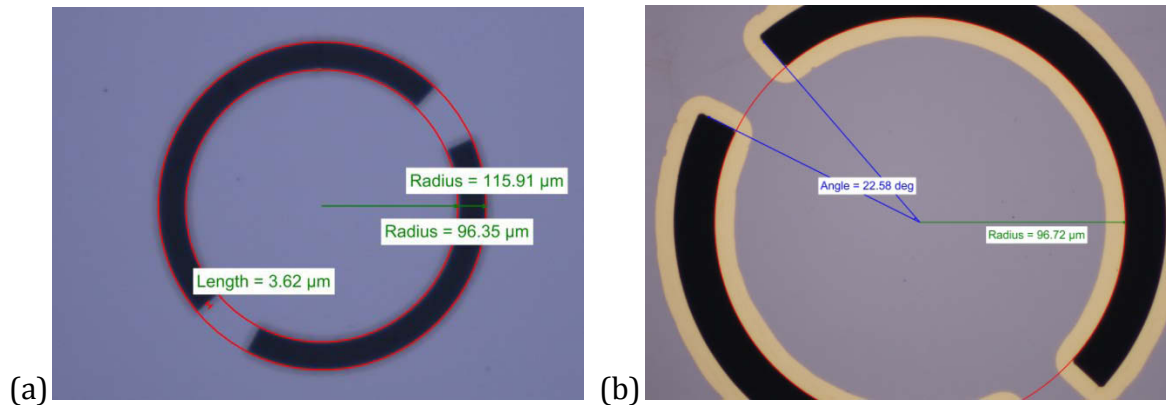
Figure 4-22: Microscope pictures of the bottom-side of an aDSR on quartz-glass with different magnifications. The measured dimensions meet the design comparably good.

Microscope pictures of the third series of biochips, which is the first series on quartz-glass show one aDSR in detail in Figure 4-22. The exemplary plotted radii and gap angle are in good agreement with the design. Only the undercut with a measured length of 3.62 µm is about 20% wider than planned. The shape of the ring agrees very well, but the edges of the adhesive layer are not perfectly straight. The process of etching 10 nm of chrome happens within a second and cannot be stopped in an instant plus the edge is not clean as a result of wet etching. Hence, the edge of the adhesive layer shows little irregularities.

The biochip is desired to be a single-use article, as usual in medical diagnosis. For research applications the production costs are high. A set of 100 biochips costs 90€ per chip excluding

establishing the production process.[III] For mass-usage an industrial microsystems production reduces costs significantly. A set of 100.000 pieces is available for 9.81€ per chip.[IV]

4.9 **Linear Scalability**

It is shown in chapter 3.2 that the resonant frequency of a split-ring resonator primarily depends on its mechanical measures due to its dipole-like resonance behavior. The frequency of the DRF is depending on the ring radius, but the shape is formed by the ratio of the arc lengths and the ratio of arc width to wavelength. Rescaling all lateral parameters by a constant factor will therefore result in a resonant wavelength scaling with the same factor. In an early stage of this research the scalability of a complementary aDSR FSS is validated. The FSS is a 400 nm gold layer on PET foil. This technology (see appendix 8.3 for details) is discarded in favor of quartz-glass substrates to improve reliability.
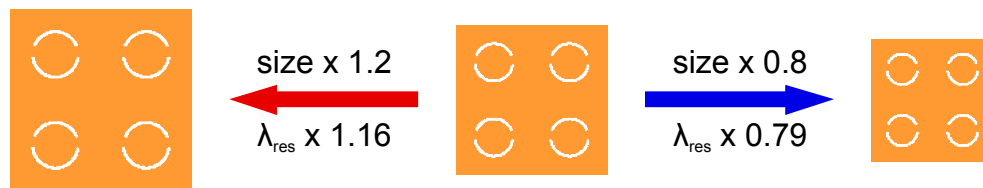
Figure 4-23: Linear rescaling of the FSS shows only little deviation of the measured resonant frequency.
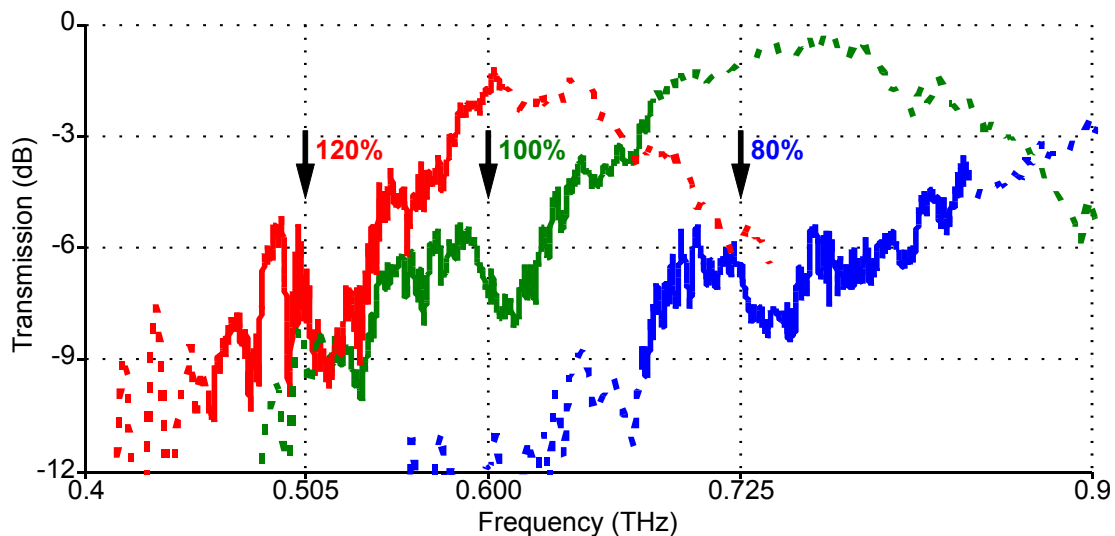
Figure 4-24: TDS measurements of the DRF for different rescaled FSSs on PET-foil with a low S/N below 500 GHz.

The scalability is depicted in Figure 4-23 with a section of a 600 GHz reference FSS in the middle. Downscaling all measures to 80 % reduces the measured DRF wavelength to 79 %, which is a very good agreement. Upscaling to 120 % moves the wavelength to 116 %. This deviation has two possible reasons. The outer radius of the split-rings is slightly smaller than expected due to manufacturing tolerances. Hence the ratio of arc width to wavelength changes compared to the reference FSS resulting in a modified DRF shape. Additionally the measurement exhibits comparably strong interferences at the 120 %-DRF, as seen in Figure

---

[III] Quotation by AMO GmbH, Aachen, 28.06.2011.
[IV] Quotation by iX-factory GmbH, Dortmund, 29.09.2009.

4-24. Taking into account the comparably low quality of the FSS due to the instable substrate and the low S/N for frequencies below 500 GHz of this TDS setup, the measurements are a good verification for the scalability of the complementary aDSR FSS.

4.10 Adapted Version for 560 GHz

In an early stage of the research underlying this work two possible operating frequencies were considered: 280 GHz and 560 GHz. Due to the good scalability of FSS, as discussed in the preceding chapter, the biochip is initially designed and optimized for 280 GHz. On the lithography mask, additionally to the 280 GHz design, a 560 GHz design is included being the same drawing rescaled to 50 %. In the production process the substrate etching is performed with the same parameters for both frequencies resulting in identical undercut lengths at different ring circumferences. Therefore, the area of the bare gold surface in the undercut of the smaller resonators is half as large as in the 280 GHz design, but with four times as many resonators per area. However, the 560 GHz radiation focus has a diameter half the size of the 280 GHz focus, reducing the active biochip area to one fourth. Hence, doubling the frequency doubles the sensitivity, as the required amount of sample material is cut in half.

A biochip reader similar to the 280 GHz setup discussed in chapter 5.3 is built for 560 GHz. Most of the components are identical, except the transmitter multiplier chain goes x6x2x3 and the receiver is a subharmonic mixer on the 36th harmonic. The research concentrates on the 280 GHz technology for two main reasons. The produced 560 GHz biochips show stronger inhomogeneities, which requires tighter processcontrol. Additionally, the reader setup behaves less stable, especially regarding ambient influences.
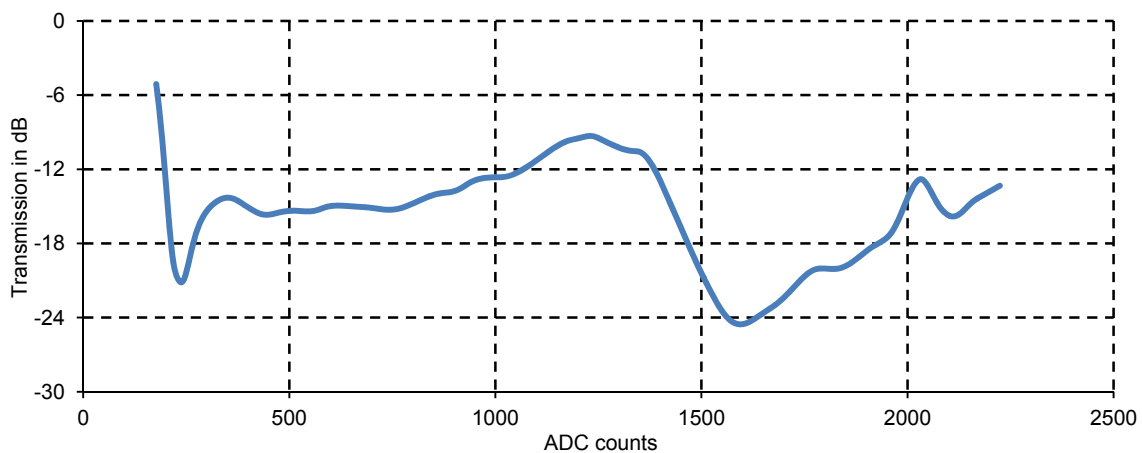
Figure 4-25: Measurement of the 600 GHz biochip with the corresponding reader. The x-axis is scaled in ADC counts, as the frequency could not be calibrated before this experiment.

The transmission of a 560 GHz biochip is plotted in Figure 4-25. The FSS parameters are identical to the 280 GHz design (Table 3), except the inner and outer radius and the periodicity are scaled by 50%. Although the measured data is already smoothened the trace is still ripply and strong interferences appear at ADC counts 250 and 2000. The frequency axis for this setup was not calibrated at the time of the experiment. The spectrum is expected to

approximately range from 540 GHz to 610 GHz which would determine the DRF frequency at 580 GHz. This is only 4% higher than the expected 2·280 GHz.

5 Biochip Reader

The biochip reader built for the readout of the presented biochips is a fully electronic THz-spectrometer based on microwave technology. This chapter first gives a general overview of THz-spectroscopy which is dominated by laser driven setups for research applications. Then selected topics of high-frequency technology are introduced leading to the fully electronic reader setup. The functionality of the reader is explained and different THz-path configurations for reflection and transmission measurements are evaluated.

One aim in the course of this research was to actually build up a system to demonstrate the functionality of THz-thin-film sensing with frequency selective surface (FSS)-based biochips and an affordable and easy to use biochip-reader. The biochip is designed with regard to everyday use. Its 2D-array allows the examination of several samples or different applications on a single chip. The biochips can be manufactured in existing microchip factories and require a few work steps only. Hence, the biochips are low-cost devices, which qualifies them for single-use applications, e.g. DNA characterization. To allow mass-usage of the biochips an appropriate machine for read-out is required. A biochip reader biotechnical and medical laboratories consider to buy has to meet the classical requirements. The acquisition and operation costs have to be low which includes low power consumption and a small size. The handling has to be easy to run it with a high throughput. Additionally, both aspects require a low maintenance system.

The designs of biochip and reader are independent of each other. The interface is a focused THz-beam. Due to this separation different biochip designs can be used without adapting the reader and the biochip can be read-out with different reader systems. There is no limitation to time- or frequency-domain, biochip materials or a special kind of THz-emitter or detector. Improvements from either area which are generated by new technologies can be applied to the system.

5.1 THz-Spectroscopy

THz-spectroscopy is a technology evolving very fast in the past 20 years. A search in Thomson Reuters's Web of Knowledge[websk] results in 12 hits only until 1990, but almost 500 hits within 2010.[I] Regarding to these results the first widely tunable spectrometer, ranging from 100 GHz to 1 THz, was presented by Helminger et al. in 1983.[Hel83] Earlier experiments with submillimeter spectroscopy for absorption line measurements had less bandwidth but achieved frequencies above 300 GHz as early as 1954.[Bur54] The spectral line measurement being the first and most important application for THz-spectroscopy[DLu03] requires both high resolution and high bandwidth. The klystron-pumped setups with harmonic mixers have a high resolution but could not achieve higher frequencies and the photovoltaic InSb detector is sensitive to power only and exhibits a low signal-to-noise ratio (S/N). Recently, microwave components, such as multipliers and mixers, utilizing semiconductor diodes have become

---

[I] Query: „(terahertz OR THz) AND spectroscopy" in topic

available at THz-frequencies and were used for building heterodyne THz-detectors and for other applications as discussed in chapter 5.2.3.

Several other approaches of THz-spectroscopy make use of various physical phenomena. Optical rectification and difference frequency generation (DFG) make use of frequency mixing in nonlinear optical media.[Lee, Pel09] Electron acceleration is used for pulse generation and electron beams are manipulated to generate continuous-wave (cw) THz-radiation in a backward wave oscillator (BWO) and a free electron laser (FEL).[Lee] Gas lasers[Shu11] and quantum cascade lasers (QCLs)[Bel09] also exist in the THz-regime but are not convenient for spectroscopy because of their extremely small bandwidth. THz-detectors are predominantly thermal sensors such as bolometers, Golay cells, and pyroelectric devices,[Lee] and more recently thermal microelectromechanical system (MEMS) multipixel sensors.[Tao11] These devices are broadband but have a slow reaction speed and cannot provide phase information. Field effect and compound semiconductor transistors have been realized for THz-signal detection[Nag11] and reached an operating frequency of 650 GHz in CMOS technology[Öje09]. They are more likely required to satisfy the demand for evolving THz-communication technology[Kle11] rather than spectroscopy due to comparably narrowband operation.

The most common THz-setup is the Time Domain Spectroscopy (TDS) driven with a short-pulse laser.[Bax11] The femtosecond laser pulses excite THz-pulses in the emitter and trigger the detector. Since the probe-pulse impinging on the detector is much shorter than the THz-pulse the THz-transient can be reproduced completely by varying the time delay between pump and probe pulse. Figure 5-1 depicts the TDS-layout with two different combinations of THz-emitter and –detector. Both, the photoconductive (pc) antenna[vEx89] and the crystal emitter, such as the low-temperature grown Gallium-Arsenide (lt-GaAs) film,[Gup91] generate coherent broadband THz-radiation. In both cases the polarization direction is defined by an applied DC-bias. On the detector side the pc-antenna as well as the electro-optic (eo) crystal with photodiodes[Zha02] measures the electric field strength. With a modulated emitter and a lock-in amplifier the measured signal provides both amplitude and phase of the transmitted THz-signal. Both detectors have a comparable sensitivity but the difficult micro-fabrication of the pc-antenna and the linearity and higher bandwidth of the eo-detector make the latter one the favored device.[Pla05]

Both types of emitter radiate into free-space. The THz-radiation is collimated and focused on the sample with parabolic mirrors or dielectric lenses. Hence, emitter and detector can be exchanged and the setup can be used not only for spectroscopy but also to drive various THz-devices and with a movable sample-holder for imaging. A wide range of extensions and modifications of THz-TDS has been presented for all kinds of applications,[Wit07, Bax11] too extensive to be summarized here.
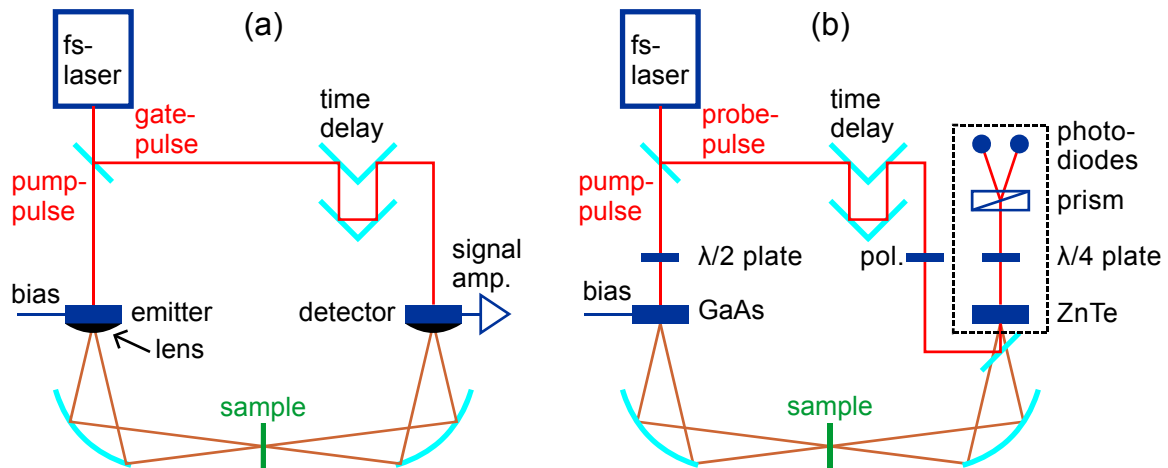
Figure 5-1 (adapted from [Sak05]): Draft of TDS setups with (a) photoconductive antennas and (b) nonlinear crystals as emitter and detector.

The recovered THz-pulses transmitted through samples are compared to reference pulses of the empty THz-path. The time delay is used to determine refractive indexes of materials, as presented in chapter 2.1. By Fourier-Transform the pulses are transferred to the frequency domain to compute the frequency response of a sample. Depending on the type of emitter and detector TDS usually covers a frequency range from approximately 100 GHz to a few Terahertz. With shorter excitation pulses bandwidths of more than 30 THz and frequencies above 100 THz have been reported.[Bax11] Actually, narrowband spectral features are more challenging for TDS. With pulse durations of a few picoseconds high frequencies are achieved, but in regard to Fast Fourier Transform (FFT) theory a high frequency resolution corresponds to a long measurement time. To achieve a resolution of $\partial f = 100$ MHz a measurement time of $t = 1/\partial f = 1000$ ps is required, but after a few tens of picoseconds mostly noise is sampled. Cutting down measuring time zero-padding, being the adding of 0 values at the end of the measured data, is a common method to increase the frequency resolution of short-time measurements.[Zhang] Zero-padding does not contain real information and is actually a smoothening of the transformed data. However, it may be useful for technical reasons to supplement the time data to a certain length. Depending on the implemented FFT algorithm commercial software requires amounts of values equal to a power of 2.

THz-TDS setups with lt-GaAs-emitter and eo-detector have been used for the characterization of the biochips in this work. With their large bandwidth and flexible usage the TDS measurements provided helpful information throughout the development progress of the biochip. However, due to the high cost, large size and extensive maintenance TDS setups are not qualified for everyday use as a biochip reader.

5.2 **Microwave Spectroscopy**

In microwave technology the transmission and reflection behavior of a device is described by its scattering matrix, or S-matrix. S-parameters being the components of the S-matrix are determined by exciting one port of the device after another and measuring the transmitted and reflected waves at each port. With regard to this the biochip practically is a two-port device with the metalized surface being port 1 and the substrate surface being port 2, as

depicted in Figure 5-2. The scattered part of the THz-radiation is small enough to be neglected due to the low biochip thickness and the perpendicular incidence of the radiation.
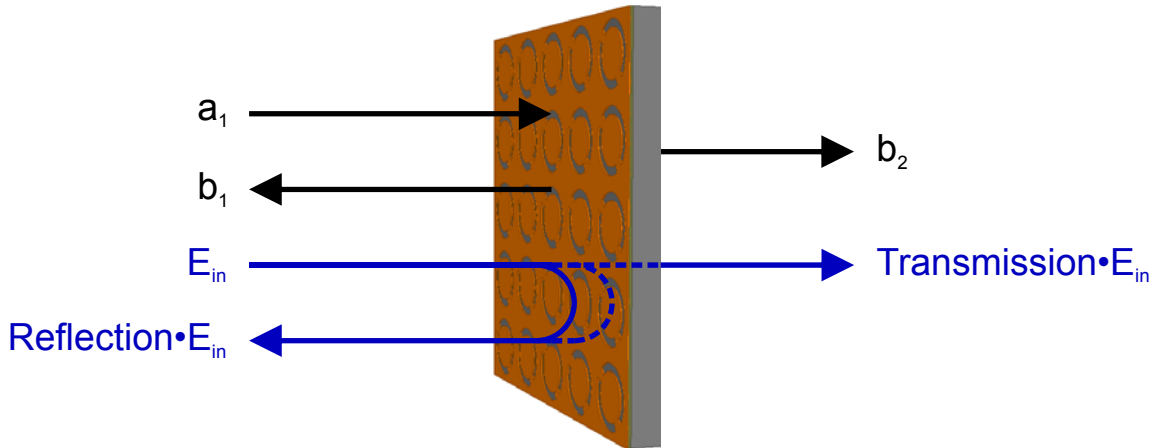
Figure 5-2: Incident (a_1) and outcoming (b_1, b_2) waves of the biochip and *Transmission / Reflection* nomenclature for unidirectional forward measurement.

The biochip does not require a bidirectional measurement, but is measured in forward direction only. The different evaluated biochip-reader setups in this work include reflection and transmission configurations. In all cases the TEM-mode of the THz-beam propagates in perpendicular direction to the biochip surface to excite all resonators in-phase. In transmission configuration the outcoming wave b_2 is detected in the receiver. The transmitted E-field equals the incident E-field times *Transmission*. Accordingly, measuring the reflection the detected E-field equals the incident field times *Reflection*. The microwave notation is given in equation (5-1) and the corresponding optical notation in equation (5-2) with non-measured elements grayed out:

$$\begin{bmatrix} b_1 \\ b_2 \end{bmatrix} = \begin{bmatrix} S_{11} & S_{12} \\ S_{21} & S_{22} \end{bmatrix} \cdot \begin{bmatrix} a_1 \\ a_2 \end{bmatrix} \tag{5-1}$$

$$\begin{bmatrix} E_{reflected} \\ E_{transmitted} \end{bmatrix} = \begin{bmatrix} Reflection & n/a \\ Transmission & n/a \end{bmatrix} \cdot \begin{bmatrix} E_{incident} \\ n/a \end{bmatrix} \tag{5-2}$$

The individual reflection and transmission coefficients at the material interfaces inside the biochip are not investigated. *Reflection* and *Transmission* can be considered the products of all reflection and transmission coefficients, respectively. Additionally, in a classical microwave measurement setup the device under test (DUT) is usually matched to the connecting waveguides. However, in a free-space setup a wave impedance mismatch between air and sample cannot be avoided broadband. Impedance matching can be realized with a polymer matching-layer. It would be sufficient for the narrowband resonance feature of the biochip, but it would reduce the sensitivity, influence the resonance behavior, and be an additional work step in the measurement preparation. Hence, in the free-space configuration the surface reflections become part of the device characteristic which is thus valid for air filled environment only.

Reflection and *Transmission* describe the actually left-over E-field amplitude which was reflected and transmitted and are therefore given in decibel (dB) with negative values. The corresponding microwave quantities *return loss* and *insertion loss* describe how much amplitude actually got lost when reflected and transmitted. The values in dB are the same as for *Reflection* and *Transmission* but with inverted sign.[Pozar]

The absorption within the biochip is kept low by choosing adequate materials. However, losses on the THz-path of the reader are caused by water absorption. Automatic calibration, as discussed in chapter 5.3.2 and equation (5-4), respectively, removes this influence by referencing. Quick changing of the ambient conditions will falsify the calibration and water lines become visible, requiring recalibration.

5.2.1   Network Analyzer

Generally, a network analyzer is used to measure the S-parameters of devices such as the biochip. Figure 5-3 depicts the principle design of a network analyzer for free-space accessible test devices in transmission configuration. For linear DUTs a baseband signal is generated, up-converted to the microwave regime and emitted through an antenna. After transmission through the DUT the microwave radiation is collected by an antenna, down-converted to the baseband and detected. With the known setup characteristic or a reference measurement the transmission parameter S_{21} can be derived from the detected signal. The DUT is broadband investigated by sweeping the signal generator frequency.
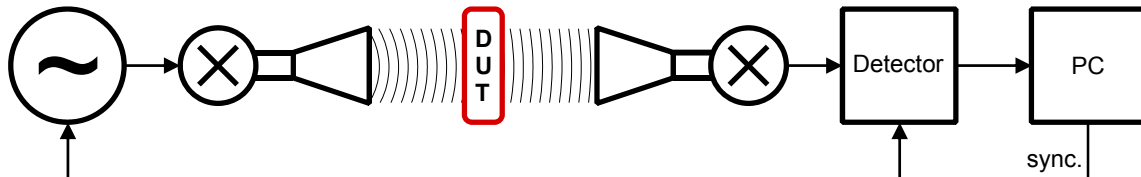
Figure 5-3: Principle of a microwave network analyzer with synchronized signal generator and detector, microwave mixers and horn antennas, and computer for control and analysis; Simplified to transmission (S21) measurement of the device under test (DUT).

In direct detection configuration, e.g. with a thermal detector, only the amplitude of the transmission can be computed. A vector network analyzer (VNA) applies heterodyne detection to measure amplitude and phase of the detected signal. By determining the complex S-parameters it enables Smith-Chart display, transfer to the time-domain and higher precision.[Thumm]

The biochip reader performing a spectral analysis of the biochips is actually a network analyzer. To keep the acquisition costs low a voltage controlled oscillator (VCO) is used instead of a synthesizer to generate the baseband signal. A subharmonic mixer is used for heterodyne detection using the same baseband signal. The intermediate frequency (IF) is quasi-generated by utilizing the time-delay of the THz-radiation during the fast frequency sweep, as explained in chapter 5.3.1. The transmission is recovered digitally in amplitude and

phase, thus enabling software signal processing and automatic calibration. With this small number of components a compact and low-maintenance reader system can be built.

5.2.2 <u>Microwave Technology</u>

In the past decade improvements in Schottky diode technology[Mae08] made conventionally designed microwave components, such as multipliers and mixers, become available at THz-frequencies,[rpg, vdi] thus enabling tunable coherent THz-sources and -detectors.

Building high-frequency oscillators becomes more difficult with increasing frequency due to the small thickness of quartz crystals.[Zinke2] To achieve a good stability and low noise it is therefore suitable to generate a lower fundamental frequency and use a multiplier to mix harmonics.[Pozar] The biochip reader works on the 18th harmonic of the baseband in the Ku-band at 12.5 – 18.3 GHz. At this frequency range a comparably cheap VCO can be used for signal generation. The baseband signal is converted to the W-band at 75 – 110 GHz by an active sixtupler. An isolator at the output protects the amplifier from backward waves. Finally, a passive tripler converts the signal to the THz-regime at 225 – 330 GHz going below one millimeter wavelength. The block diagram of the source is shown in Figure 5-4.

x6   75 - 110   x3
12.5 - 18.3   225 - 330
GHz   GHz   GHz
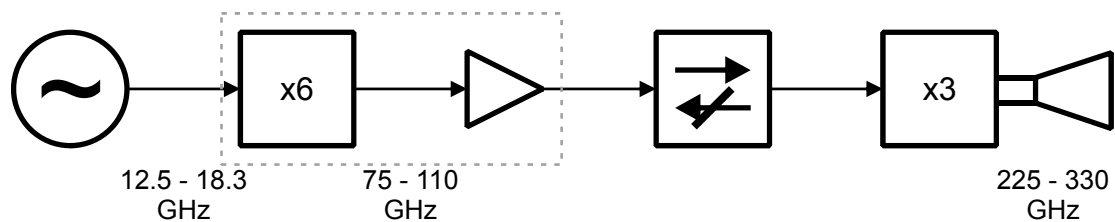
Figure 5-4: Block diagram of the biochip reader THz-source: A local oscillator generates the baseband (Ku) which is converted to the W-band by a sixtupler and amplified. After an isolator a tripler generates the mm-band radiation emitted through a horn antenna.

Heterodyne detection is realized with a subharmonic mixer providing a higher spectral resolution compared to TDS. Recent THz-frequency mixers for heterodyne detection mostly apply Schottky diodes and are coupled by rectangular waveguides (for RF) and cables (for LO). Earlier versions of mixing and multiplying devices utilized the nonlinear reactance of varactor diodes implying the need for idle networks to generate other than second order harmonics and products.[Penfi] In contrast, nonlinear resistive Schottky diodes generate all harmonics and products with the disadvantage of a conversion efficiency decreasing with rising order, as described by the power relationships of Page & Pantell.[Pag58, Pan58] Because of their fast conductivity mechanism at the metal-semiconductor junction Schottky diodes are suitable for high-frequency applications.[Zinke2] Superconductor-insulator-superconductor (SIS) devices are mainly used in astronomy applications due to antenna coupling and hot-electron-bolometers (HEBs) can be used for heterodyne detection with small bandwidths and at low temperatures only.[Siz10]
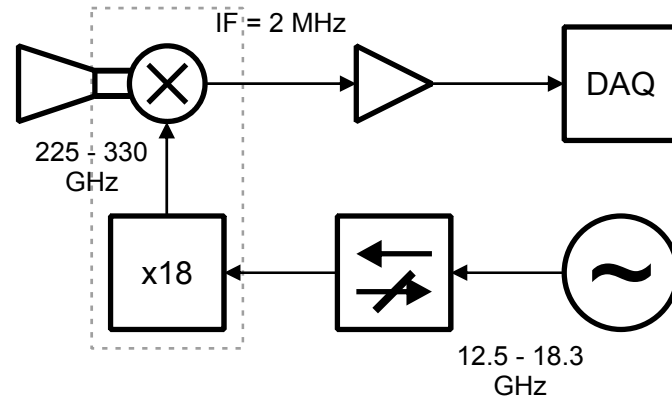
Figure 5-5: Block diagram of the biochip reader THz-detector: The 18th harmonic of the baseband signal from the local oscillator is mixed with the received THz-radiation. The intermediate frequency (IF) is amplified and digitized. An isolator blocks baseband reflections.

The biochip reader detector (Figure 5-5) uses a Schottky diode-based subharmonic mixer mixing the THz-frequency with the 18th harmonic of the baseband. The resulting intermediate frequency (IF) at 2 MHz is amplified and digitized for software signal processing. Baseband reflections from the mixer not being matched are blocked at the mixer input by an isolator. This protection measure is essential in order to maintain coherence. Both, detector and source of the biochip reader are driven with the same baseband oscillator. Any reflection on the baseband cabling could result in an interference causing phase errors.

5.2.3 THz-Applications with Microwave Technology

The commercial availability of electronic and waveguide based THz-components recently led to a variety of experiments transforming microwave applications to the submillimeter range. Similar to the biochip reader some of these are designed with multiplier chains and heterodyne detection, such as the following two examples.

The work of Jastrow et al.[Jas10] is shown in Figure 5-6: A wireless digital data transmission setup is build with almost 300 GHz carrier frequency and a classical heterodyne receiver with independently operating transmitter and receiver. The local oscillator generates a frequency of 16.4 GHz which is first multiplied by 9 then doubled and mixed with the modulated IF to become a broadcast signal with 295 GHz center frequency. The receiver is built in the same way with LO and multiplier, except for a slightly different LO frequency to reduce phase noise. The subharmonic mixer recovers an intermediate frequency which can be demodulated with the applied TV analyzer. The work demonstrates the possibility of a high data rate transmission at one millimeter wavelength. The considerably low noise floor is a good result, since multipliers increase phase errors.[Jas10] The system shows a good transmission quality for 64-QAM on short distances and a usable 8-PSK transmission over a distance of 52 m.[II]

[II] Digital modulation methods: 64-QAM – quadrature amplitude modulation with 64 carrier states shifting amplitude and phase; 8-PSK – phase shift keying with eight carrier states shifting phase only, but with constant amplitude.
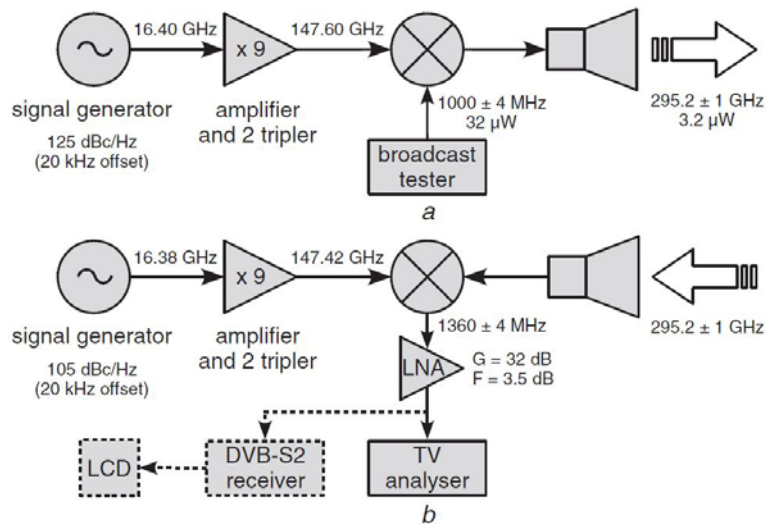
Figure 5-6 (with permission from [Jas10]): *a* Source and *b* detector of a 300 GHz digital data transmission test setup for TV broadcast. © [2010] IEEE.

A slightly modified concept for mm-wave reflection measurements is used by Kapilewich et al.[Kap10] to build a radar imaging system for security applications. As shown in Figure 5-7 THz- source and -detector are as well multiplier chains with a GHz baseband generator. Two significant changes are noticeable. The system uses only one synthesizer for both source and detector and there is no modulation except for the LO frequency sweep. Heterodyne detection with a subharmonic mixer is enabled the same way as with the biochip reader (see chapter 5.3.1), but the received signal is evaluated after FFT in time domain only. The time-of-flight is used to determine the distance to the target while the height of the FFT peak describes the reflection intensity. By mechanically scanning a scene, this system can be used for 3D-imaging, e.g. for revealing hidden metallic objects on people.[Kap10] Compared to the biochip reader this radar uses a very small baseband bandwidth. Thus it is capable of long detection ranges up to tens of meters but not of spectroscopic applications. Additionally the biochip reader uses fewer components and exhibits a much higher S/N.
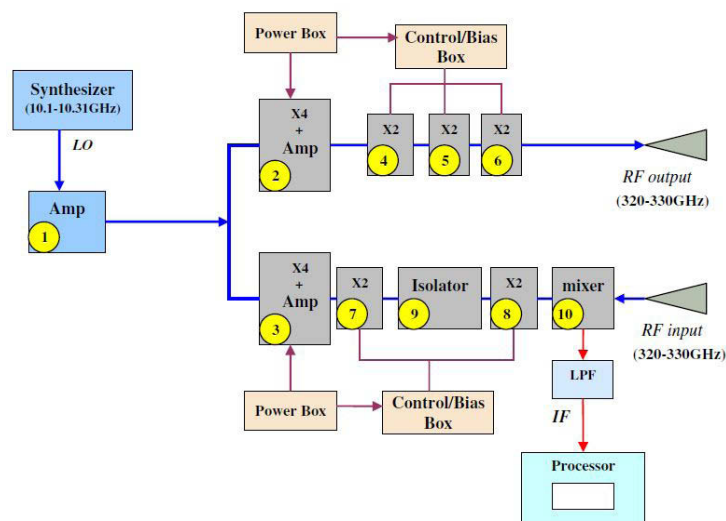
Figure 5-7 (with permission from [Kap10]): 300 GHz imaging radar with one oscillator for source and detector.

Other approaches of imaging with THz-electronics aim to increase imaging resolution[Coo08] and acquisition speed[aWe09]. The technology found its way into atmospheric observation and astronomy[Sch99] and is used for the measurement of gas emission spectra[Oh09]. Further potential is seen in rectenna applications[Has11] and digital holography for nondestructive material test[Hei11].

5.3 **Biochip Reader Setup**

The biochip reader is intended to be a compact, low cost, and easy-to-use system to demonstrate the market-readyness of THz-biochip technology. Commercially available compact-size THz-spectrometer systems, such as the fiber-coupled Picometrix T-Ray 4000®[pic] and the closed Zomega mini-Z[zom] are laser-based TDS systems with an insufficient frequency resolution, comparably slow sweeping speed, and high cost. The interferometric Emcore PB7200 with two fiber-coupled DFB-lasers and photomixer detector features a good resolution of 100 MHz but exhibits long measurement times with one second per frequency for a comparable S/N.[Log11] This system is compact, light-weight, easy-to-use, and being battery-powered even portable, hence meeting most of the requirements. But with a measurement time of 17 minutes for 100 GHz bandwidth it is way too slow.

The biochip reader[Deb11/this work] on the other hand is a fully electronic microwave system operating in the frequency domain. To cover a certain bandwidth a frequency sweep is performed tuning the source periodically. The system is built upon a Synview T-Ranger 300 which has been modified and enhanced in hard- and software for optimal biochip read-out.

5.3.1 **Hardware**

The THz-radiation is generated by harmonic mixing of a local oscillator (LO) signal. The LO signal, or baseband, ranging from 12.5 GHz to 18.3 GHz is generated by a voltage controlled oscillator (VCO). Within one frequency sweep of a measurement the frequency is increased linearly over time forming a ramp with consecutive measurements resembling a sawtooth. The voltage ramp driving the VCO is generated in software and D/A converted. However, the VCO is not perfectly linear. To ensure a linear increase of the frequency the VCO output is sampled for calibration. The software compares the sampled frequency to the theoretical value and compensates the voltage ramp.

The VCO signal is used to drive both the THz-source and THz-detector, referred to as transmitter (Tx) and receiver (Rx). Using only one baseband source reduces system cost and size. Additionally, the VCO is significantly cheaper than a synthesizer, however, on the cost of stability. But since the baseband is provided to transmitter and receiver simultaneously distortions affect both parts leaving their relation stable. A scheme of the high-frequency part of the reader is shown in Figure 5-8.
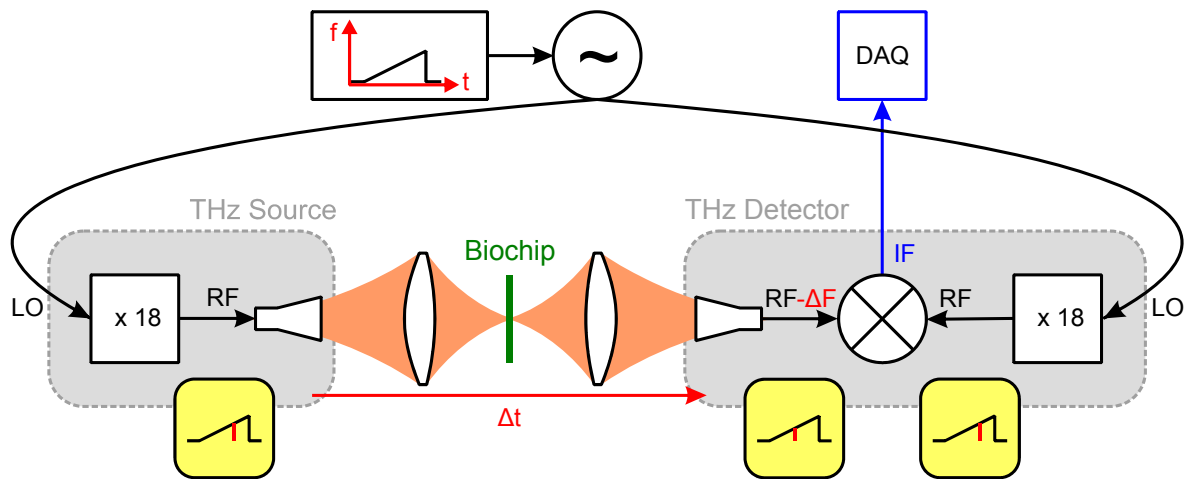
Figure 5-8: Biochip reader scheme: One LO feeds source and detector. The THz-radiation is focused on the biochip by lenses. The insets (yellow) depict the different signal runtimes allowing quasi-heterodyne detection.

The LO signal is multiplied to the THz-regime in transmitter and receiver as explained in chapter 5.2.2. The biochip transmission is recovered in amplitude and phase by quasi-heterodyne detection. A regular heterodyne detector mixes the received radio frequency RF with a slightly lower reference RF to generate an intermediate frequency IF. In the case of identical LO signals for transmitter and receiver the IF is zero or DC, respectively. The biochip reader uses identical LO signals which however are time variant due to the frequency sweep. A DC output is achieved for identical signal runtimes for received and reference RF from the oscillator to the receiver mixer. Considering feed cables with the same length, the THz-path actually is a delay causing the received RF to arrive at the receiver later than the reference RF. As depicted in Figure 5-9 a time delay Δt along the VCO ramp corresponds to a frequency difference Δf which by mixing becomes the intermediate frequency IF.
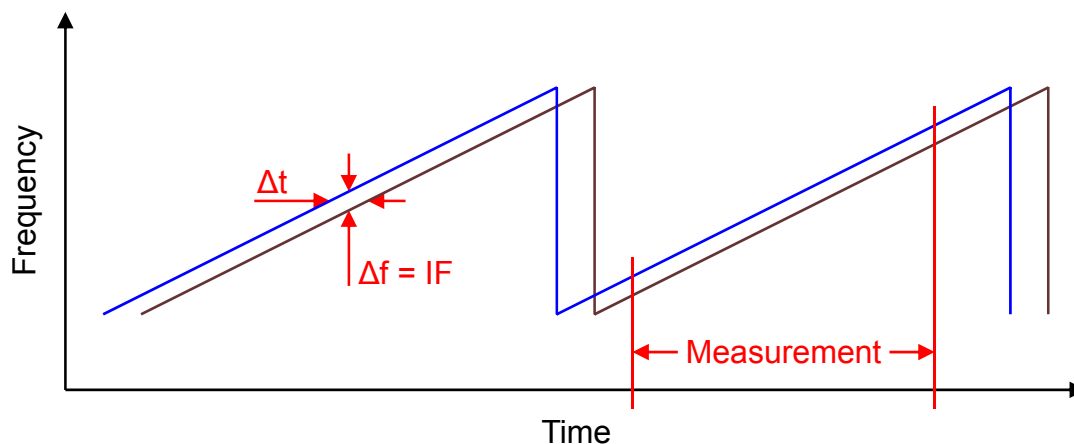
Figure 5-9: THz-frequency ramps at the receiver mixer: The received signal (brown) which travelled the quasi-optical THz-path arrives later than the reference signal (blue). Both ends of each ramp are cut off.

The intermediate frequency is sampled with a National Instruments data acquisition system (DAQ) at a sampling rate $f_T = 10$ MS/s. The transmitter is fed with a longer cable than the receiver to increase the delay Δt and therefore the IF. Experimental optimization for a high S/N of the THz-measurement results in an IF with $f_{IF} = 1.8$ MHz. Due to the sampling

theorem the required sampling rate, or Nyquist rate, is $f_N \geq 2f_{IF} = 3.6$ MHz. But phase noise and nonlinear group velocities broaden the IF peak with spectral components up to almost 5 MHz. The oversampling avoids aliasing from these distortions and reduces noise.[Lüke]

Each frequency sweep is digitized in 240 μs with 2400 samples, of which the 2048 center samples are extracted as measurement data, as depicted in Figure 5-9. The beginning and the end of the data contain false frequency information and trigger artifacts and are therefore cut off. A section of the sampled raw data is shown in the upper trace of Figure 5-10.
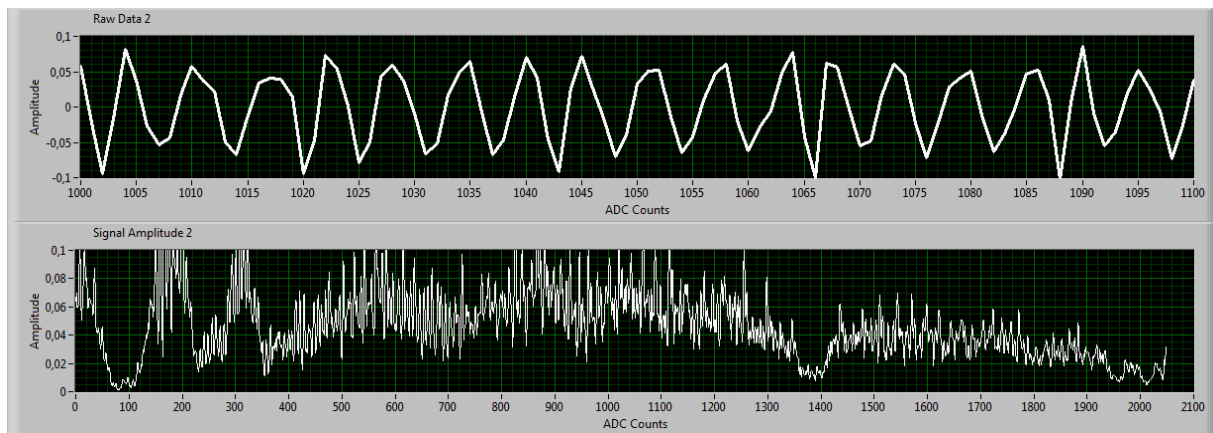
Figure 5-10 (LabView Screenshot): Intermediate frequency IF (upper trace, 100 samples) and system THz frequency response (lower trace, center 2048 samples).

The system is designed for an LO frequency range from 12.5 GHz to 18.3 GHz corresponding to a RF frequency range of 225 GHz to 329 GHz. The final demonstrator system performs a shorter frequency sweep to avoid distortion, interferences, and amplitude breaks at certain frequencies. Although all components are commercially available the setup is an experimental system. The THz-components are not fully characterized and do not exhibit a constant efficiency over the full frequency range. The lower trace of Figure 5-10 shows the amplitude of the measurement data without a sample. The strong amplitude variation along one frequency sweep is caused by the frequency dependent behavior of the THz-components. The signal breaks at ADC count such as 100 and 1400 result in a low S/N at the corresponding frequencies. Therefore the biochip resonance frequency is located in the middle of the measurement where a stable amplitude prevails. The technology is set up to measure small resonant frequency shifts, hence reducing the bandwidth is advantageous to decrease system noise and improve THz-frequency resolution.

The specifications of the final demonstrator version of the biochip reader are given in Table 4. Compared to THz-TDS systems the bandwidth of the biochip reader is rather small. However, it is several times broader than the biochip's resonance feature. The frequency resolution on the other hand is much higher than in classical TDS setups and the sweep speed being the bandwidth per sweep time is orders of magnitude higher.

Frequency Range	244 – 318 GHz
Bandwidth	74 GHz
Frequency Resolution	31 MHz (raw data) < 0.5 GHz (filtered data)
Sweep Time Full Measurement Time	240 µs per ramp 110 ms (100 averages, incl. signal processing and output)
Sweep Speed	> 300 THz / s
Signal-to-Noise	> 50 dB

Table 4: Spectrometer Specifications

The performance of THz-TDS systems is improved with asynchronous optical sampling (ASOPS). The source and detector laser beams are generated in two different lasers with different repetition rate. The varying time between the impinging pulses substitutes the mechanical delay stage resulting in much shorter measurement times. The high-speed setup by Klatten et al.[Kla09] features 6 THz bandwidth at 1 GHz resolution with 500 µs sweep time resulting in a high sweep speed of 12,000 THz/s. The measurement time can even be reduced by the similar electronically controlled optical sampling (ECOPS).[Kim10] Both systems are built with two Ti:Sapphire lasers making the setup extremely expensive and large. The ASOPS system can be made cheaper and smaller replacing one laser by a semiconductor disk laser (SDL).[Geb10] However, this option offers only 3 GHz resolution and is still too complex for commercial applications.

A more promising technology is cw-photomixing, also known as optical heterodyne conversion. Two optical beams are mixed in a semiconductor crystal to generate their difference frequency in the THz-range. A high-precision photomixing setup with two fiber-coupled distributed feedback (DFB) lasers[Den08] has been used for spectroscopic investigations of solids[Rog10] from 60 GHz to 1.8 THz at a resolution of 1 MHz with 3 Hz measurement rate. The system would be sensitive enough for biochip readout but its spiral antenna structures at source and detector at not polarization preservative and the two near-IR DFB-lasers with interferometric stabilization are too expensive. A similar setup with a different crystal and laser configuration provides even more bandwidth but requires more maintenance due to its free-space configuration.[Tan09] Other setups are used for spectroscopy[Sun10] and thickness determination[Sch10] with poor frequency resolutions of a few Gigahertz.

Lasers at telecom wavelength are more and more included into research setups due to their small size and lower price.[Bax11] Applying fiber-coupling for low maintenance could make photomixing an interesting technology for commercial spectroscopic applications such as a biochip reader.

5.3.2 Software Signal Processing

The intermediate frequency is processed on a PC in a LabView software environment.
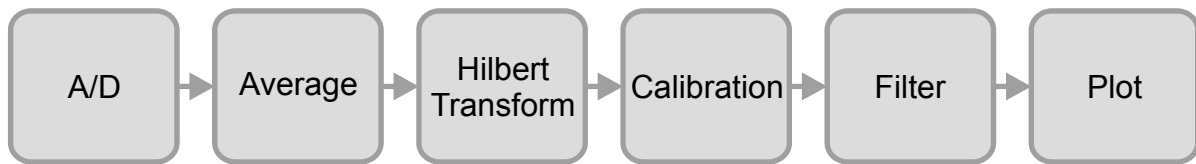
Figure 5-11: Software Blockdiagramm

The sampled raw data is cut off at beginning and end, as described above. A series of consecutive measurements is recorded to improve S/N by averaging. The raw data is the time-discrete real part of the IF. The imaginary part is computed by Hilbert Transform to obtain the full complex values which are then separated in amplitude and phase.[Oppen] These values correspond to the transmission of the THz-signal because of consequent linear data handling:

$$ADC\ count \sim time \sim LO\ frequency \sim RF \qquad (5\text{-}3)$$

In order to extract the transmission properties of a sample from the measured data the system has to be calibrated with a *match* and a *short* measurement, as described by equation (5-4). The match measurement, which is a measurement with a blocked THz-path, represents an offset caused by noise from receiver components and reflections on LO cabling. The short measurement with an empty THz-path contains these distortions plus the THz-path reference. The calibration measurements have to be taken once and are used for all sample measurements as long as the system is stable. Strong variations in the environment such as temperature or humidity affect the THz-path and require rerecording of short and match measurements.

$$Transmission\ = \frac{Sample - Match}{Short - Match} \qquad (5\text{-}4)$$

Finally, each the amplitude and phase data is transferred to a logarithmic scale and a cubic spline filter is applied to smoothen the output signal.

For fine-tuning the THz-frequency axis scaling is computed by a Synview routine: After calibration generating a flat phase spectrum the delay Δt has to be changed mechanically resulting in a phase rising linearly over frequency. The frequency axis increment is computed from the gradient of the unwrapped phase, the absolute value from the distance to the origin. This requires an estimation of the lowest displayed frequency which can be determined from the VCO datasheet with known voltage.

Although not required for biochip readout, the time-signal of the transmission is computed by Inverse Fourier Transform. Since the frequency spectrum (after calibration) is flat the time signal is a peak. The peak is moving along the timescale as material is brought into the THz-path. This feature can be used for rapid determination of a material's refractive index from the time-shift with known thickness.

5.4 THz-Path Setup

The THz-radiation is generated and recovered in closed components with WR-3 waveguide[III] out- and inputs, respectively. Horn antennas are attached for impedance matching and directivity. Different configurations of THz-paths are evaluated for optimal biochip readout.

5.4.1 Quasioptical Transmission Setup

The direct transmission configuration with Tx and Rx horn antennas is set up with bi-convex Teflon lenses in 4f-configuration, as depicted in Figure 5-12. The lenses with a 2:1 image scale are positioned with the biochip and the horn antenna feeds at their focal points corresponding to a distance of 73.6 mm from the biochip and 146.2 mm from the horn antennas. With a lens thickness on the center axis of 16 mm the total length of the THz-path is 471.6 mm. The long focal length corresponds to the antenna directivity for an almost full illumination of the 2 inch diameter lenses. The focal length on the biochip side is chosen shorter to reduce the focal point diameter. A numerical aperture of $NA \approx 0.3$ at 1 mm wavelength (300 GHz) results in a focal point diameter $w = 0.61 \cdot \lambda/NA = 2$ mm. Measurements scanning a metal plate with a small aperture confirm an almost perfectly round beam profile with a focus diameter of approximately 2.5 mm.
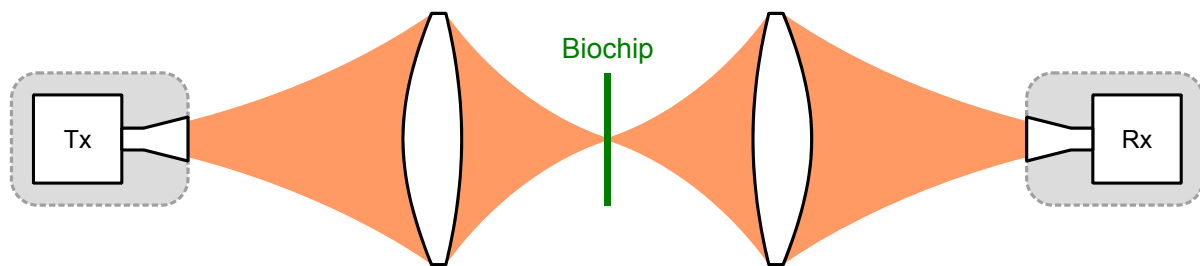
Figure 5-12: Quasi-optical THz-path in 4f-configuration with 2:1 image scale bi-convex lenses.

A convenient Rayleigh length of 3 mm ensures a plain wavefront impinging on the biochip. Multiple reflections in this configuration cause narrowband distortions in the measurement due to standing waves. The low refractive index of 1.44 and the curved surface of the bi-convex lenses reduce these distortions. Pushy ones are further reduced by adjusting the frequency sweep steepness.

This quasioptical configuration works reliably with the biochips used for the measurements in chapter 6. The distance between the lenses is large enough to include motorized linear stages for automated movement of the biochip.

5.4.2 Waveguide Setup

The quasioptical setup described above requires a distance between different sample spots at least as large as the focal point diameter of 2.5 mm. This resolution might be improved with lenses of shorter focal length, thus increasing the difficulty of aligning the quasioptical path. An optimal usage of the THz-radiation would be the integration of the

---

[III] WR-3: EIA notation for a rectangular hollow waveguide with a cross-section of 34x17 mils = 0.864x0.432 mm.

biochip into the hollow waveguide whose cross-section is approximately equal to the area of one pair of biochip resonators. Due to the small waveguide dimensions of 864 μm x 432 μm mechanical realization and handling would be too complex. Instead, the biochip is positioned between the ends of the Tx and Rx waveguide in contact, as depicted in Figure 5-13 (a). For the THz-wave the biochip resonators appear to be inside the waveguide followed by a subwavelength slit being the chip substrate. The reflected wave is measured with a second receiver connected via a directional coupler. The outcoupling of -10 dB reduces the transmitted power by only 10% leaving -10.5 dB or 9% of the Tx power for the reflection receiver Rxr at full reflection. The resonance feature can be distinguished from the measurements. However, distortions are caused by multiple reflections inside the waveguides due to impedance mismatching at the biochip interfaces. The spectrum of these distortions exhibits features with a higher dynamic range than the biochip resonance feature. Therefore, the waveguide setup is unsuitable for the biochip application.
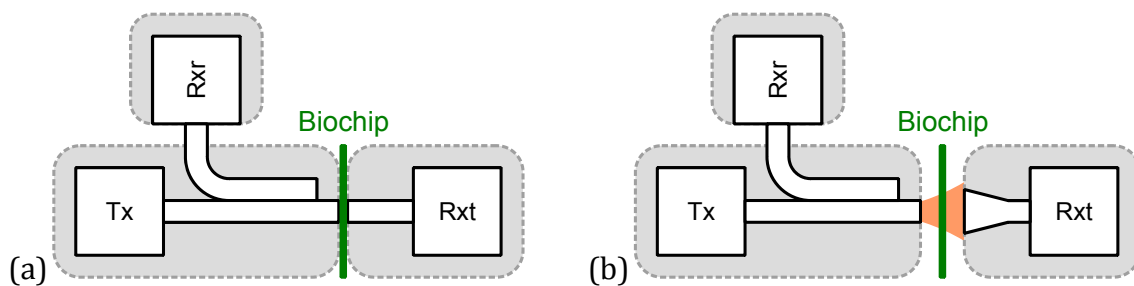
Figure 5-13: Reflection setups with a directional coupler. (a) Waveguide setup: biochip sandwiched between Tx and Rxt waveguide ends without horn antennas. (b) Hybrid setup: biochip in short distance to Tx waveguide end and Rxt with collecting horn antenna.

5.4.3 Hybrid Setup

A combination of the quasioptical and the waveguide setup is realized in order to combine the high lateral resolution with a moveable biochip. Moving the chip in contact to the waveguide causes scratches to the chip possibly damaging resonators or destroying samples. A soft dielectric protection film would avoid scratching but also detune the biochip resonance. Instead, the chip is mounted to a holder without contact but at a subwavelength distance to the THz- components. The transmission is measured applying a horn antenna to collect most of the diverging beam. In this configuration scattering has a huge effect on the amount of collected radiation at the receiver. Errors deriving from small positioning deviations of a few micrometers are amplified by scattering which results in strong distortions. Due to these this setup is not suitable for biochip readout. For collecting the radiation at the receiver a more convenient solution is required to make use of the high resolution from the direct waveguide illumination.
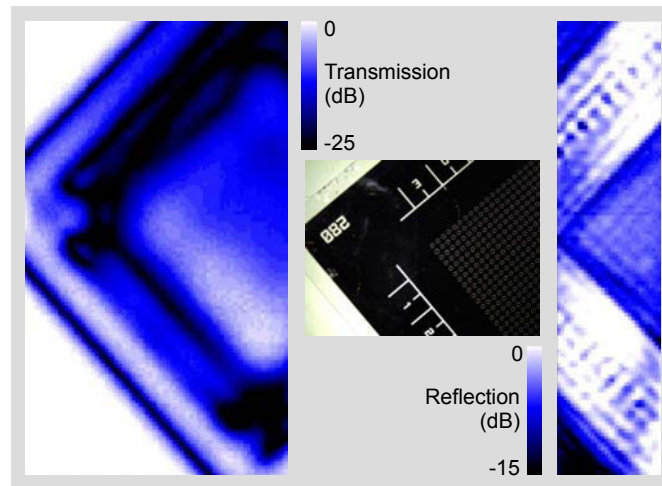
Figure 5-14: Imaging at 275 GHz in 200 µm steps with quasioptical transmission setup (left) and waveguide reflection setup (right); optical photo for comparison (middle), all true to scale.

However, by analyzing the amplitude of a stable THz-frequency the system can be used for subwavelength imaging. Figure 5-14 compares the imaging capabilities of the quasioptical and the waveguide setup. Both pictures show a biochip section of 25 mm height and are true to scale. With its comparably large 2.5 mm focus the quasioptical setup can only roughly distinguish between the closed metal surface and the split ring array. The small waveguide illumination recognizes sharp edges, indicates the small inscription, and shows an interference pattern from the split ring array.

5.5 **Demonstrator Setup**

Finally, the reader setup was reduced to the minimum of required components in order to build a demonstrator. The system is self-calibrating thus eliminating the need for maintenance. With its motorized moveable sample holder the system can automatically read-out sample arrays from biochips. The demonstrator proves that a THz-biochip read-out system can be built as a compact table-top unit on a commercially competitive basis. As shown in Figure 5-15 it consists of five components. Optical and THz-components, motor stages and cabling are mounted on a 30 x 60 cm breadboard. The baseband electronics (LO) are integrated in the DAQ housing with an external amplifier for the VCO. The controller for the motor stages and the laptop complete the setup. With its low overall weight of 20 kg and insensitivity on mechanical vibrations this electrical THz-spectrometer outclasses laser based THz-setups regarding consideration for further development to a commercial product.
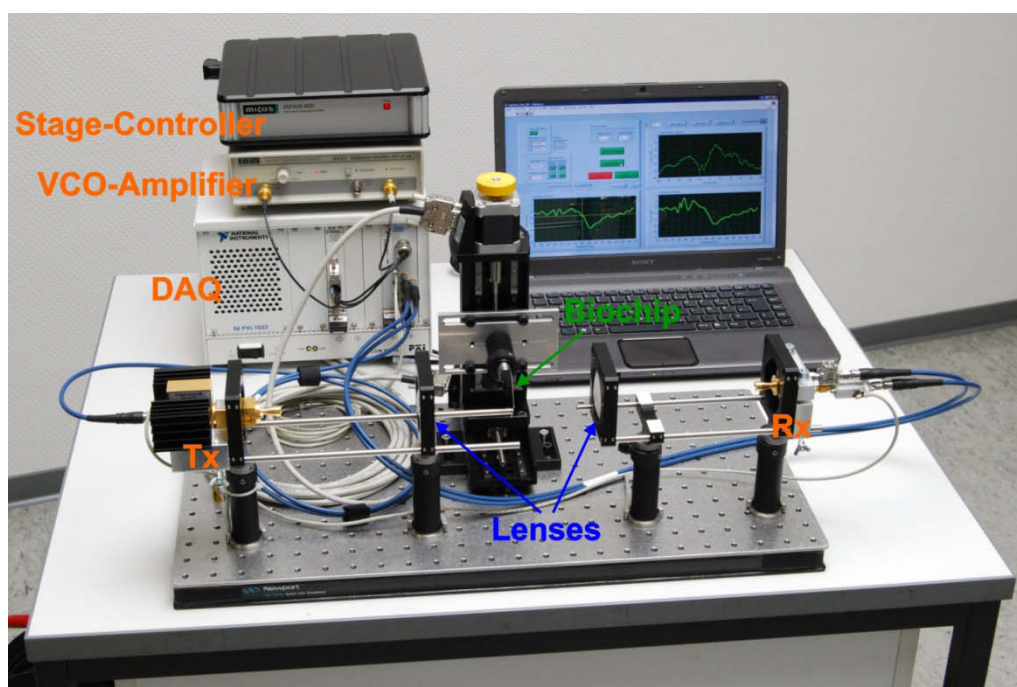
Figure 5-15: Photo of the biochip reader demonstrator setup on a small table. The computer displays the active LabView user interface with a running biochip measurement.

6 Measurements and Results

The transmission of the biochips made of complementary aDSR resonators on quartz-glass (chapter 4.7) is measured with the biochip reader (chapter 5.5). The functionality of the empty chips and the detection of thin-films are confirmed by measurements in this chapter. The detection of DNA succeeded, however it could not be reproduced later in a test series to investigate hybridization states. Reasons for this are investigated and discussed.

In the previous chapters a biochip with a resonance feature at 280 GHz and a biochip reader with a spectral range of approximately 240 GHz to 320 GHz are developed forming a detection technology for minute amounts or thin-films of dielectric material. Two biochips, shown in Figure 6-1, are realized. They are not entirely covered by the frequency selective surface (FSS), but contain labeling simplifying adjustment and handling. With a theoretical FWHM focus diameter of 2 mm for the biochip reader demonstrator setup, the FSS is sufficiently large as a 5 x 5 array of resonators. Figure 6-1(a) depicts a biochip with 25 arrays, enabling the measurement of 24 samples and a reference on one chip. The variation shown in Figure 6-1(b) is one large 29 x 29 array of resonators. Labeling enables a logical division in rows and columns. The inscription "LPQ" identifies the design as linearly polarized (LP) and fit for quartz-glass substrates. "280" stands for the DRF frequency of 280 GHz and the bar at the left corner depicts the orientation of the aperture arcs, hence giving the polarization direction of the magnetic field.

(a)   (b)
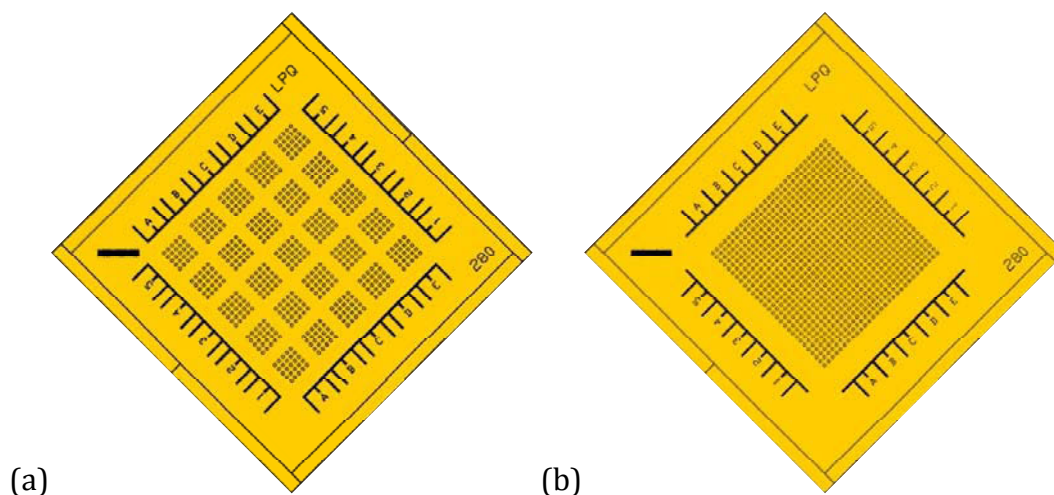
Figure 6-1: Biochip designs with (a) 25 arrays of 5 x 5 resonators and (b) one array of 29 x 29 resonators. Total size is 24 mm x 24 mm. E-field is vertically polarized.

A small set of biochips is produced in July 2009 which is used for a first DNA experiment. For a thorough investigation on DNA-binding detectability a larger set of biochips is required. Unfortunately, in Mai 2010 when the larger series of biochips is produced, technical difficulties disturbed the production process. Partial reconstruction of the clean-room facilities caused contaminations to the infrastructure. At that time the chips are produce with defects and a significant inhomogeneity, respectively. Defects in the metallization are shown

in Figure 6-2(a). Particles in the DI-water contaminated the surface resulting in pinhole-size holes in the metal layers. The chrome-etch process, which is intended to remove the chrome in the undercut, also etches in these pinholes. The result is a "starry sky".

(a) (b)
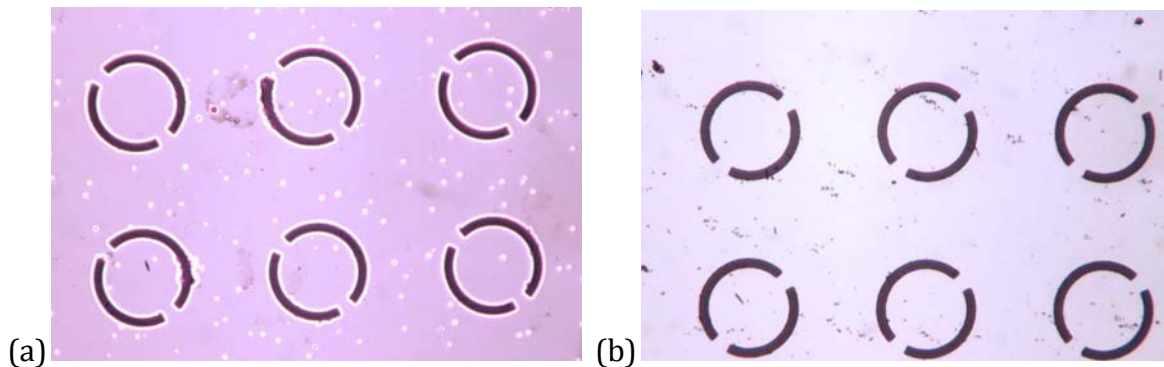
Figure 6-2: Microscope pictures of the biochip, taken from the bottom side, showing the chrome adhesive layer. (a) First set in 2010 after the chrome-etch process, showing defects in the gold layer resembling a starry sky. (b) Third set in 2010 without chrome-etch process.

A closer look at the resonators is taken with a scanning electron microscope (SEM), component of a Helios NanoLab600 focused ion beam (FIB). A defect is shown in Figure 6-3(a) where the metal layer (light gray) is partially torn and folded. The resonator aperture (dark gray) exhibits a good flatness on the undercut ground but a rough slope of the undercut sidewall. A different defect is shown in Figure 6-3(b) where a cross-section view is realized cutting a grove into the chip. The undercut slope appears comparably flat and the undercut is blocked by an unidentified deposition.

(a) (b)

Figure 6-3: SEM-pictures of resonator details showing (a) a rough slope of the undercut sidewall and a part of the metal layer torn and bent, and (b) the cross-section of a resonator side with an almost triangular undercut and an unknown deposition (white) jamming the undercut.

Under these circumstances the verification of the biochip technology is performed with modified biochips. Etching of chrome is omitted. Instead, to generate an accessible gold surface, the chrome cover layer is left out. This modified biochip has the same resonant behavior as the originally designed one. However, the DNA loading is not taking place in the undercut only, but on the full top surface. The modified chip is shown in Figure 6-2(b) where particles or scratches on the glass can be seen, but the overall amount of defects is

significantly reduced. Still a low inhomogeneity is measured, which is made unharmful by averaging over a small area within a larger functionalization spot, as depicted in Figure 6-4(a). The design used for the 2010 measurements is the large array which is logically divided into quarters (Figure 6-4(b)).

(a)   (b)
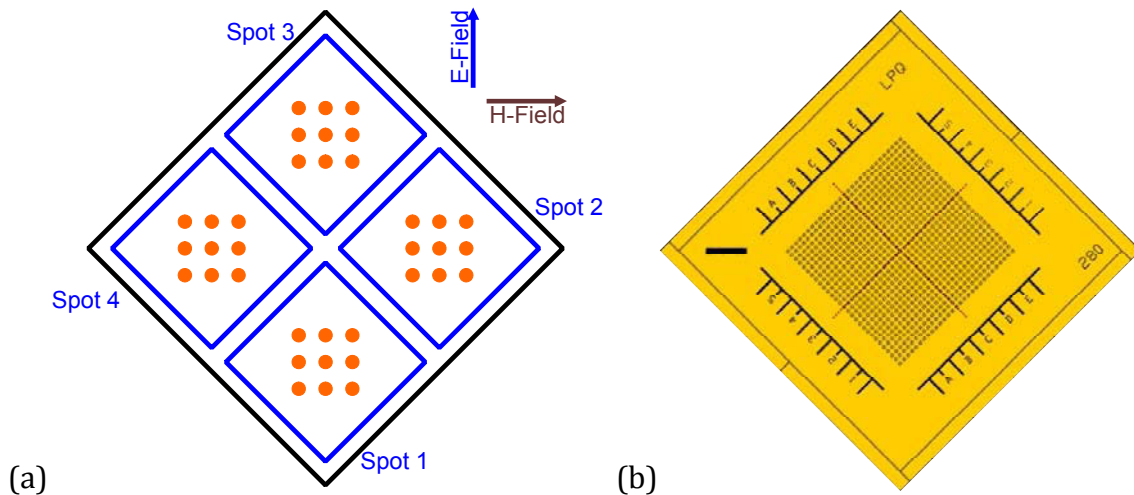
Figure 6-4: Biochip measurement design (a) including 9 measurement focuses (orange dots) per measurement spot (blue square) and (b) corresponding logical division (red lines) of the large array chip.

6.1 **Biochip Design**

The biochips are measured with the biochip reader to compare the resonant behavior with the theoretical and simulated predictions. The measured signal quality and the frequency axis scaling vary between the diagrams, due to reader optimization efforts being performed in parallel.
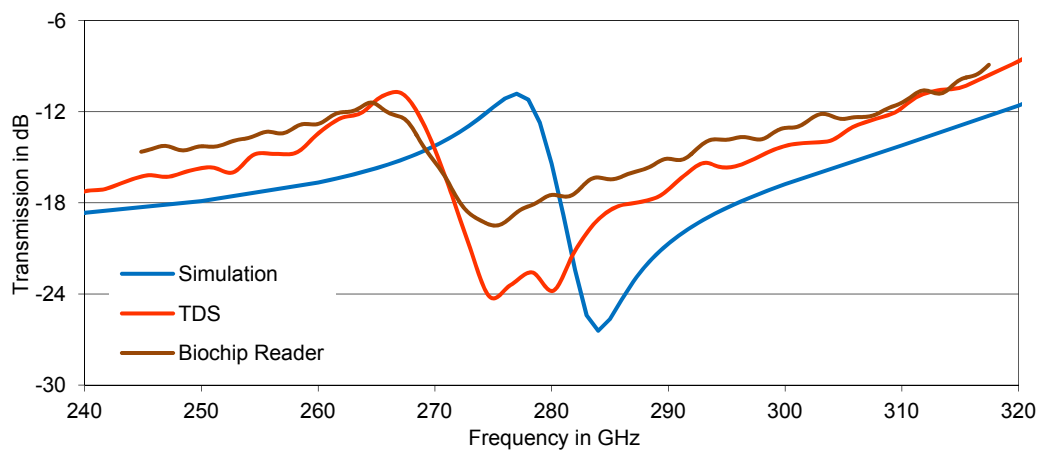
Figure 6-5: Transmission of a complementary aDSR FSS (LP) on silicon substrate. The measurements with the reader (brown) and TDS (red) deviate from the simulation (blue) due to inhomogeneous undercut etching.

The transmission of the 280 GHz chip on silicon substrate is plotted in Figure 6-5. The TDS measurement deviates significantly from the simulation. The DRF appears at a lower frequency and has a lower modulation. Especially the minimum is weaker as the overall spectrum level is higher. Reason for this is a sloped silicon-oxide layer. The undercut size

varies strongly and does not reach its desired depth. Either the oxidation or the oxide etching process failed. Since both are not required for the quartz biochips this problem is not investigated further. The measurement with the biochip reader deviates even more than the TDS. In the early development state of the reader reflections on the THz-path distort the measurements resulting in biochip resonances determined weaker.
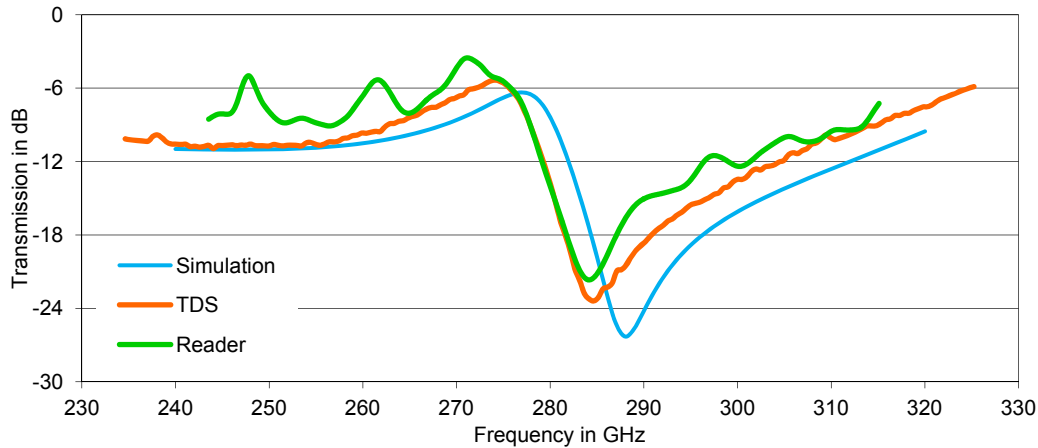
Figure 6-6: Transmission of a complementary aDSR FSS (LP) on quartz-glass substrate. The measurements with the biochip reader (green) and TDS (orange) are in excellent agreement and deviate from the simulation (blue) by less than 3 GHz only.

The biochips on quartz-glass substrates exhibit much better results. The measured and simulated transmission is plotted in Figure 6-6. The measurements by the biochip reader and a TDS setup are in excellent agreement. The DRF appears at the same frequency and with almost identical shape. The reader measurement, however, shows additional peaks caused by multiple reflections on the THz-path, which lead to interferences e.g. at 248 GHz and 262 GHz. The simulation marginally deviates from the measurements due to ideally modeled corners and edges and an assumed infinite extent.
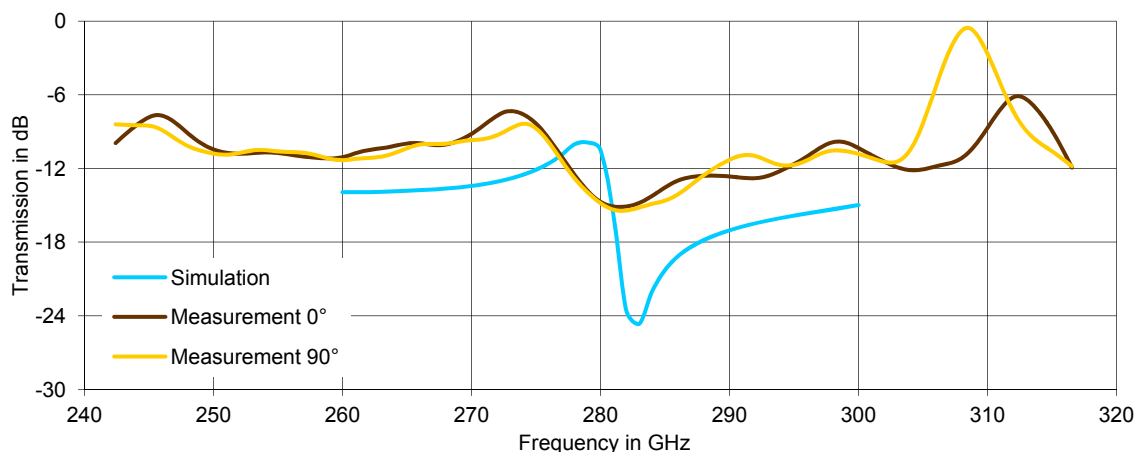
Figure 6-7: Transmission of a complementary aDSR FSS on quartz-glass substrate with center-symmetric (ZS) resonator arrangement. The measurements along and across (dark and light brown) LP-orientation agree very well, but the DRF shape differs strongly from the prediction (blue).

The new biochip technology with the FSS-based chips measured by the biochip reader promises to be sensitive enough to detect thin-films such as DNA. The full DRF flank measures

17 dB over 10 GHz with a steep part of 10 dB over 4 GHz in the DRF center. An expected frequency shift on the order of 1 or 2 GHz (chapter 4.2) can reliably be detected.

The alternative chip design with a center symmetric (ZS) arrangement of the aDSRs is designed to be independent of the polarization direction of the incident THz-radiation. The measurements in Figure 6-7 present the DRF at 277 GHz with a low steepness of approximately 8 dB over 8 GHz, or 2 dB over 1.3 GHz in the DRF center. The measurements with different directions of polarization are in good agreement, but they differ considerably from the simulation.

6.2 **Thin-Film Sensing**

The set of biochip and biochip reader forms a technology to demonstrate the feasibility of measuring dielectric thin-films in the lower THz-frequency-range at a reasonable effort. Although the detection of DNA is the application focused for, the verification of the thin-film sensing capability is done using PMMA as sample material, because its mechanical and dielectric properties are well known.
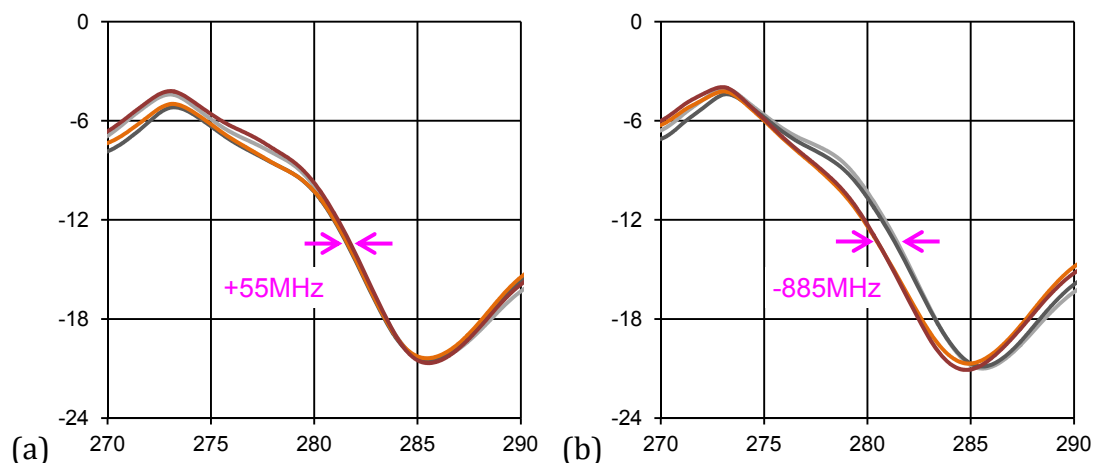
Figure 6-8: Transmission in dB over frequency in GHz of a biochip (a) clean and (b) loaded with a 100 nm thin-film of PMMA. Spots 1 and 2 (light and dark gray) are the references, spots 3 (orange) and 4 (red) are sample spots. The dielectric loading causes a frequency shift of approximately 0.9 GHz.

PMMA in solution is used as photo resist for electron beam lithography. In this liquid form it is deposited as a homogenous film on wafers by a spin-on process. The spin-on parameters given by the manufacturer are used to generate PMMA films on the biochip surface.[I] Half of the surface is covered by adhesive tape, which is removed after PMMA deposition leaving two clean reference spots and two sample spots for measurement. Measurement results of a biochip with a 100 nm film of PMMA are plotted in Figure 6-8. Due to the chip inhomogeneities mentioned above, all chips are measured before sample deposition for comparison. The clean chip in (a) exhibits the DRF with a reduced modulation at 282 GHz. The difference between reference spots and the desired sample spots is +55 MHz in average, which means that the DRF of the empty sample spots appears 55 MHz higher than the

---

[I] The resists from Allresist Gesellschaft für chemische Produkte zur Mikrostrukturierung mbH, Strausberg, are AR-P679.01 for thicknesses < 50 nm and AR-P679.02 > 50 nm.

references'. After deposition (b) the DRFs of the sample spots are in average 885 MHz lower than those of the references. The dual resonance feature shifts approximately 0.9 GHz due to loading with a dielectric film of 100 nm thickness only. This proves aDSRs superior to SRRs whose thin-film detection limit[OHa08] is found at this thickness. The localized field improves the sensitivity and with the sharp resonance feature smaller resonant frequency shifts are detected.

The PMMA spin-on is known to be working on surfaces without topology, but the biochip's metal screen has apertures with a depth of approximately 700 nm (500 nm undercut plus 200 nm metal layer). The topology of a clean and a loaded aperture are controlled by atomic force microscopy (AFM). The depth of the clean aperture is approximately 670 nm (Figure 6-9(a)) whereas in the loaded case it is 635 nm. Assuming a correct 100 nm film on the metal screen the deposition inside the aperture is 35 nm thicker, but the split ring is not filled to the edge. The values for different measured resonators differ marginally only.
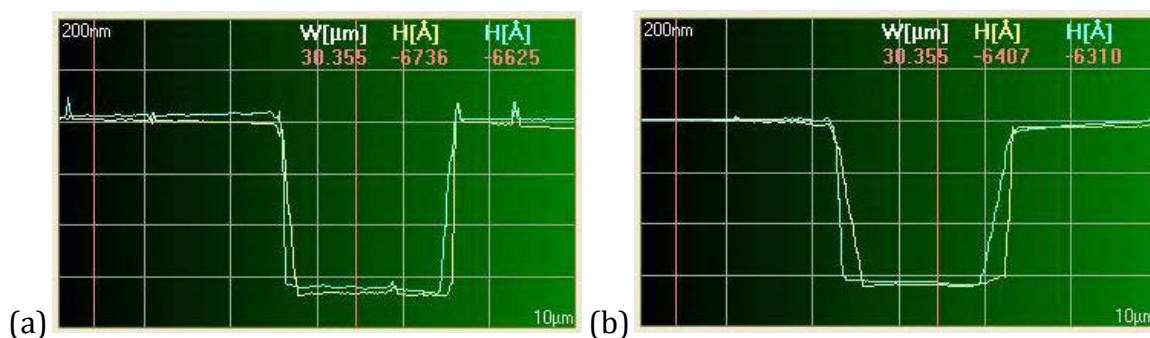
Figure 6-9 (screenshots): AFM measurements of the split-ring topology of (a) a clean chip with an average 668 nm aperture depth and (b) a chip with a 100 nm thin-film of PMMA with an average 636 nm depth.

A set of five biochips is used to measure different PMMA film thicknesses. Due to the filling effect of the split ring apertures, the amount of sample material is not scaling with the film thickness set by the spin-on parameters. The film on top of the biochip achieves the requested thickness, but unless the 100 nm measurement the filling height of experiments with thinner films differs and varies more strongly. Covering the chip with 20 nm of PMMA gives the most inconsistent results. The four measurement spots of the empty chip have resonances close together. The difference between dedicated sample spot and reference spot is +70 MHz and +40 MHz, respectively. The 20 nm PMMA film causes frequency shifts of 140 MHz and 640 MHz, respectively, as shown in Figure 6-10. The stronger shift results from a filling of the split ring with more than 20 nm. Two main consequences can be drawn from these results: With a thin loading on the metal screen a frequency shift as large as with a thicker film can be achieved due to filled up split rings, which proves that the sensitivity is increased by the field concentration inside the undercut. The term "thin-film sensing" on the other hand has to be treated in a more distinguished way. In theory the DNA loading is a thin-film, but it is only deposited on the gold surface in the undercut. In contrast, the technical deposition of a resist thin-film, such as the spun-on PMMA, all over the biochip has to deal with the topology. With a depth of the split rings of 700 nm not much thinner films can be deposited homogeneously.
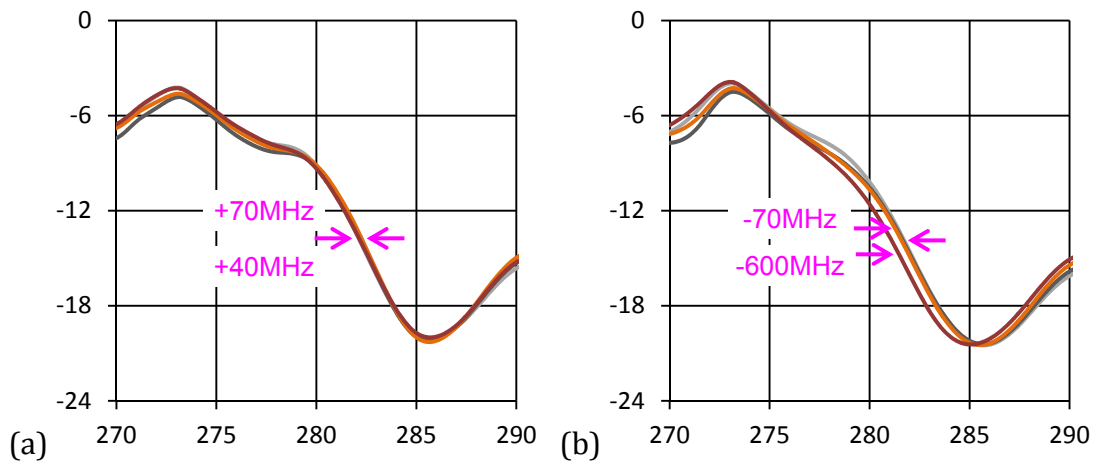
Figure 6-10: Transmission in dB over frequency in GHz of a biochip (a) clean and (b) loaded with a 20 nm thin-film of PMMA. Spots 1 and 2 (light and dark gray) are the references, spots 3 (orange) and 4 (red) are loaded. The frequency shift due to dielectric loading varies over sample spots.

The frequency shifts of the full set of PMMA measurements are summarized in Figure 6-11. The results for the 60, 70, and 100 nm films show good agreement of each the two measurement spots. The frequency shift is expected to be lower with a thinner film. However, the 70 nm shift as much as the 100 nm, whereas the 60 nm shift much less. This is caused by the different filling heights in the split rings depending on rotation speed and the exact position of dropping the solution in the spin-on process. The results for thinner films of 20 and 30 nm are even more inconsistent. The concentration of PMMA in the solvent is lower for the 679.01 type. Although generally it is seen that thinner films cause a lower frequency shift, no quantitative statement can be made. Anyhow, the results prove the frequency shift of the biochip's DRF to be prevalently depending on the amount of material in the undercut.
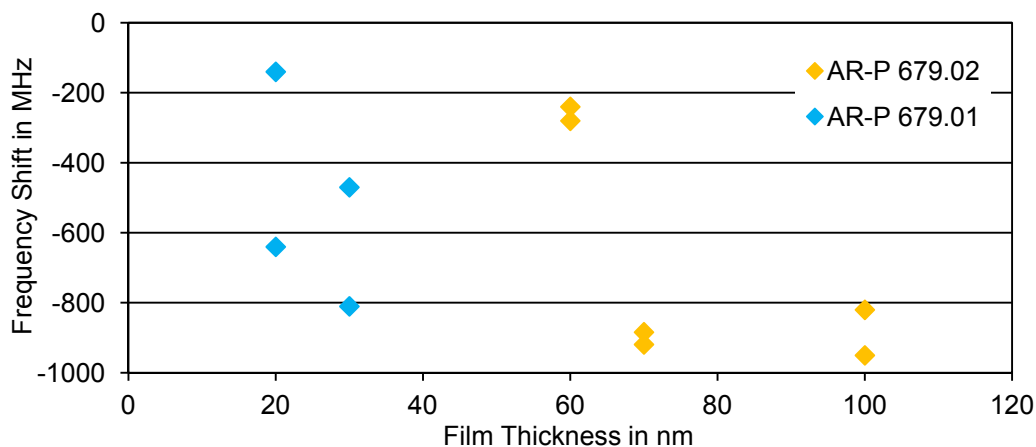
Figure 6-11: Frequency shifts of the biochip's DRF due to PMMA loading, with two measurement spots per chip / film thickness. The resonator apertures are deeper than film thickness, thus resulting in inconsistent shifts but confirming the field concentration in the undercut.

Another experiment trying to achieve different thicknesses and split-ring fillings is performed as a serial dilution of UV-dye.[II] The dye is available in solution forming a film of Paraloid including fluorescent pigments. The four measurements spots of a biochip are treated differently. One spot is left clear for reference. On the other spots identical solution amounts are deposited by dropping with a pipette. The dye in solution is diluted with additional solvent (ethylacetat) to produce concentrations of 1 % and 10 %. The dielectric Paraloid film causes frequency shifts as plotted in Figure 6-12. The 1 % spot shows no reliable shift. The 10 % spot shifts 2.5 GHz and the 100 % spot shifts 18.5 GHz. These films completely fill the split-ring apertures and cover the surface. The fluorescent color is used to verify the extent and homogeneity of the films. Since the rings are filled with sample in all cases the sample distribution differs in thickness above the metal screen only. With a thickness of approximately 10 times higher, the frequency shift is 7.4 times larger. Hence, the E-field distribution above the chip is, as predicted, the denser the closer it is to surface.
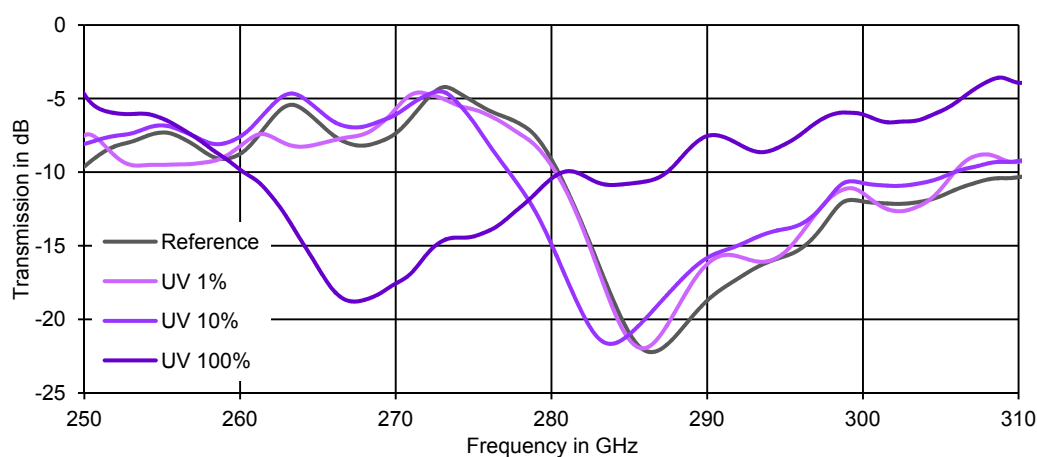
Figure 6-12: Serial dilution with fluorescent UV-dye. Different concentrations are deposited on the chip's measurement spots and dried.

Both sample materials used above, PMMA and Paraloid, are polymers. In the next step the biochip's sensitivity on organic material is confirmed. Similar to the UV-dye experiment a serial dilution is performed with technical gelatin. The gelatin is diluted in DI-water in two concentrations. First 1 g of gelatin is diluted in 100 ml DI-water at 60 °C and 2 mg of color pigments of Sulforhodamin 101 ("Texas Red") are added to enable optical inspection. For the second spot this solution is diluted to a concentration of 1 %. Again identical amounts (13.5 µl) of solution are dropped on the measurement spots leaving 100 times more gelatin on spot 4 than on spot 2 after drying. Spots 1 and 3 are left clean for reference. The chip is measured before and after gelatin deposition with reference DRF frequency changing less than 0.1 GHz. The thin film on spot 2 is estimated by AFM measurements to be approximately 100 nm thick. It causes a frequency shift of 1.3 GHz, while the thick layer shifts the DRF 11.1 GHz, as shown in Figure 6-13. As with the UV-dye, the gelatin film has a strong effect on the biochip's resonance close to the surface, quickly saturating with increasing thickness.

[II] The UV-dye is Lumogen 947361 fluorescent color pigments and clear Paraloid lacquer in solution from Kremer Pigmente, Aichstetten, absorbing at 378 nm (ultraviolet) and emitting at 434 nm (blue).
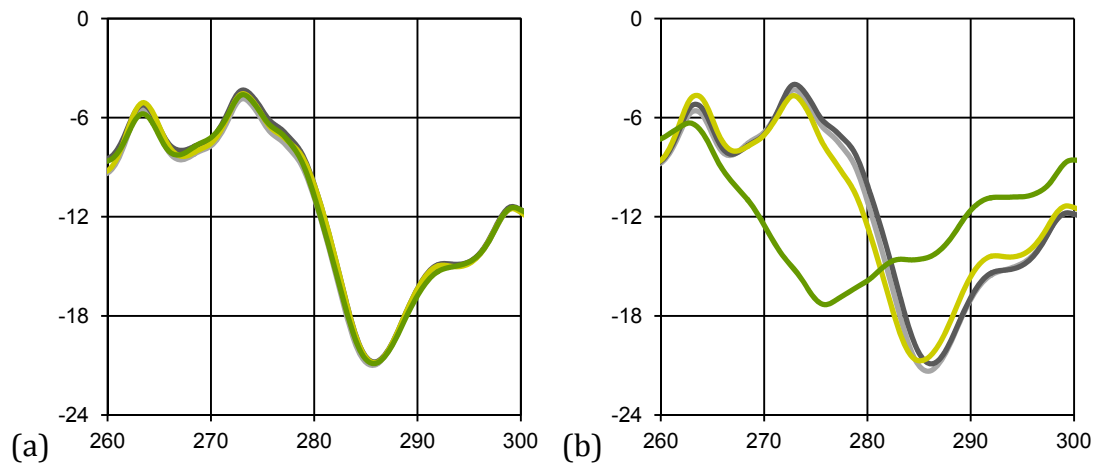
Figure 6-13: Transmission in dB over frequency in GHz of a biochip (a) clean and (b) loaded with thin-films of technical gelatin. Spots 1 and 3 (light and dark gray) are the references, spots 2 and 4 (light and dark green) are covered by a thin and a thick gelatin layer, respectively.

The biochip is proven to be sensitive enough for measurements of dielectric thin-films below 100 nm thickness at 280 GHz measurement frequency. The corresponding wavelength is more than 10^4 times larger than film thickness. In regard to the discussion in chapter 4.2, which leads to similar resonant frequency shifts for DNA films and thin polymer films, the biochip's sensitivity is sufficient for DNA sensing. Additionally, the gelatin experiment confirms the capability of sensing small amounts of organic material.

6.3 DNA-Sensing

6.3.1 DNA-Functionalization

For the sensing of DNA with the biochips, the sample DNA-strands are deposited in the undercut, as discussed in chapter 4.5. The DNA strands are immobilized locally on the open gold surface macroscopically forming a thin film. This technique involving a thiol for linking the DNA strand with the gold surface[Her97] was established by the group of M. Tarlov. The recipe of functionalizing THz-sensors with DNA is adapted from [Nag03], where measurements on single- and double-stranded DNA are presented with a much more complex kind of biochip / reader technology.

For the indirect identification of DNA the binding state of single probe strands to sample strands is determined. Simplified, if the strands are complementary they "hybridize" (bind) forming double-stranded DNA, otherwise they stay "denatured" (unbound). The biochip, consisting of glass and metal, is "functionalized" with probe-DNA for binding-state dependent measurements: First, double-stranded DNA molecules are "immobilized" on the surface with a linker at the 5'-end of the probe strand as drafted in Figure 6-14(a). The DNA is then denatured on-chip to remove the complementary part, leaving the functionalized biochip (b). The DNA could also be immobilized single-stranded, but the double-stranded way ensures sufficient spacing between the strands for on-chip hybridization. For the measurement sample DNA strands are brought onto the surface. If they are complementary to the immobilized probe strands, sample and probe strands hybridize. (Figure 6-14(c)) A

fluorescent marker, in the experiments here, is connected to the 3'-end of the sample. The hybridized DNA film exhibits a higher permittivity than the denatured film thus shifting the biochips resonance feature. The marker is attached for double-check purposes. The DNA-film on the biochip is fluorescent if the probe and sample strand hybridize only.
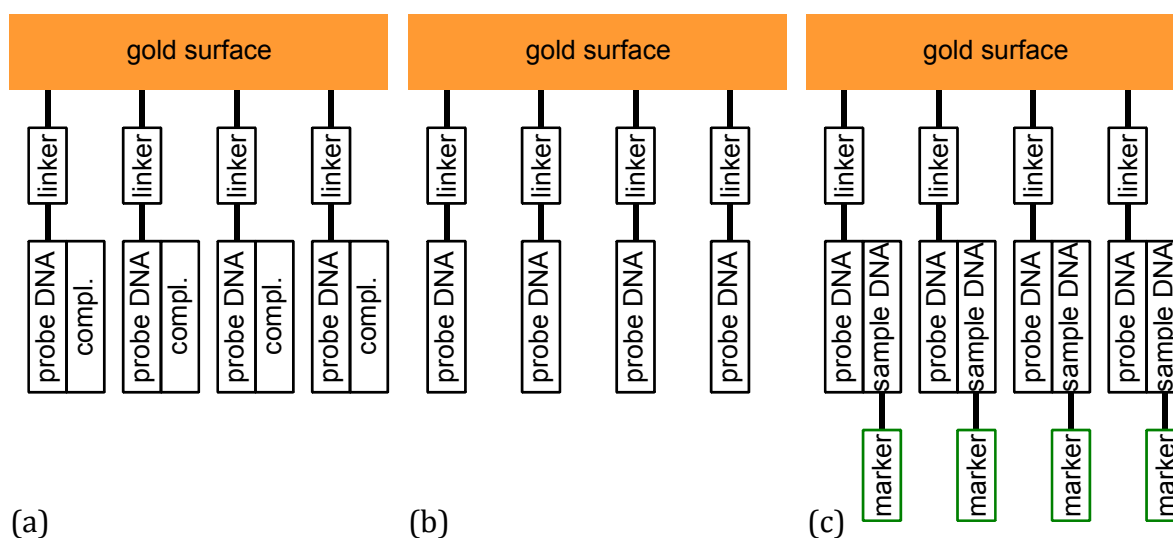
Figure 6-14: Theoretical DNA assembly with (a) immobilized double-stranded molecules linked to the gold surface, (b) single-stranded probe DNA only (functionalized) and (c) hybridized probe and sample strands with fluorescent marker linked to the sample strands.

For handling the DNA strands are always in solution. The individual descriptions of every step of the recipe are listed in appendix-chapter 8.5. The biochips are cleaned before functionalization in acetone and ethanol (five minutes each), purged with DI-water, and dried in a nitrogen flow. The DNA in solution is dripped on the biochip's sample spots with a pipette at 0.5 µl per drop.[III] Several drops are deposited consecutively, depending on the spot size. After 30 minutes the remains of the solution are removed by purging with DI-water. The chip is held in the water-flow carefully to avoid the water contaminating the reference spots.

The gold layer of the quartz-glass based biochip has an accessible gold surface on the bottom side and the layer edge of $4.73 \cdot 10^{-9}$ m^2 per resonator. The way of functionalizing with double-stranded DNA and denaturing results in an occupancy of approximately $5 \cdot 10^{12}$ molecules per square centimeter.[Pet97] Thus, one resonator saturates at $236.5 \cdot 10^6$ molecules or 0.4 fmol DNA per resonator.

In the functionalization process the biochip is exposed to chemicals for cleaning and to substances included in the DNA buffer solution. The biochip is resistant to the cleaning chemicals acetone, isopropanol, ethanol, DI-water, and nitrogen flow. Additionally, drying at 80 °C does not harm the chip. Biochip-reader measurements before and after chemical treatment perfectly agree.

The buffer solution contains various diluted salts, as listed in the recipe in appendix-chapter 8.5. When it is poured over the biochip, it leaves a highly inhomogeneous salt crust on

---

III Eppendorf Research Variable with PCR-clean ep-TIPS including filter to avoid cross-contamination

the surface and in the undercuts after drying. The crust is removed in a DI-water flow. A chip of the inferior 2010 series is logically divided into four measurement spots of which two are loaded with buffer solution and two are cleaned only for reference. Figure 6-15 shows the measurements at different states of the experiment. The absolute frequency value deviates between the measurements due to axis rescaling of the system being thermally unstable at the time. Actually, the sample spots are compared to reference spots to eliminate the need for a correct absolute frequency. The sample loading is indicated by the frequency shift of the sample spot compared to the reference spot. After cleaning and drying the DRFs of all four spots are close together. A small deviation due to chip inhomogeneity is seen. With the salt loading the sample spots show the DRFs shifted to lower frequencies. A larger amount of salt on spot 4 (Figure 6-15(b), red) causes a stronger shift than the lower amount on spot 1 (orange). After cleaning (c) the DRFs are closer again, but the sample spots still have a reduced resonant frequency due to humidity left over from cleaning. After 24 hours (d) the chip is completely dry and the four spots are as similar as before again. Steepness and modulation of the DRF remain unchanged proving the biochip to be resistant but also sensitive to the chemicals. The solution does not harm the structures, but it has to be removed from the resonators completely by thoroughly flushing the chips with DI-water after immobilization. Otherwise it will falsify the DNA measurement.
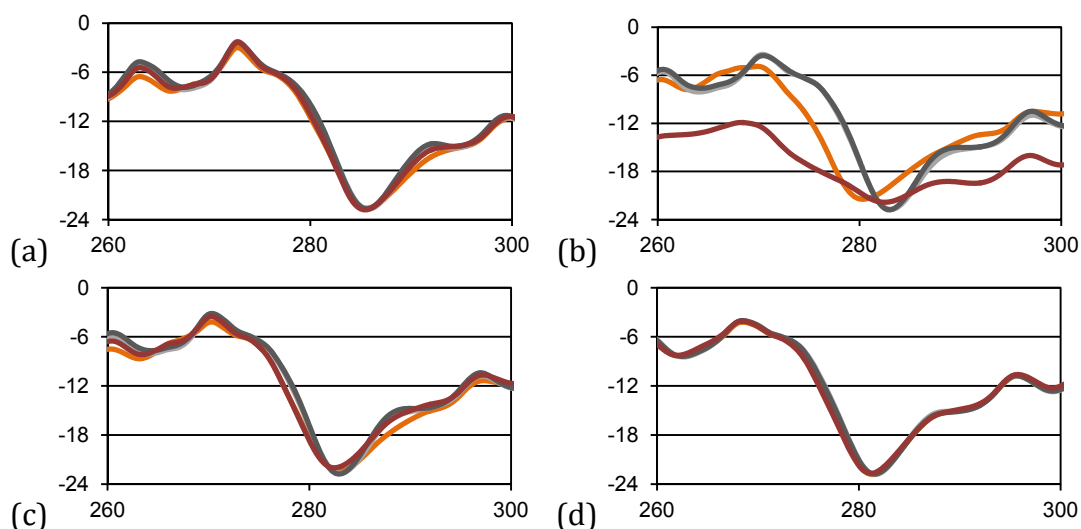
Figure 6-15: Transmission in dB over frequency in GHz of a biochip (a) after cleaning, (b) with salt crust from dried DNA buffer solution, (c) after cleaning from salt, and (d) one day later. Spots 1 (orange) and 4 (red) are loaded, spots 2 and 3 (light and dark gray) are references. The measurements approve chemical resistance to the DNA buffer solution and sensitivity to the salt in the solution and to water.

6.3.2 Successful dsDNA Measurement

With one chip of the good 2009 set, the presence of double-stranded DNA is measured. The chip is designed as one large array (Figure 6-1(b)) and logically divided into halves. One half is functionalized with a double-stranded random sequence "Oligo1/2", as discussed in chapter 6.3.1 and appendix-chapter 8.5, while the other half of the chip is left clean for reference. To avoid measurement artifacts from THz-path reflections the chip is removed from the biochip reader after each measurement (including 100 frequency sweeps). For the next measurement

the reader is short- and match-calibrated and the biochip is readjusted. Six consecutive measurements of each sample and reference are plotted in Figure 6-16 (pale blue and green). Several outliers appear e.g. at 300 GHz. These outliers are similar for corresponding reference and sample measurements. The mean values of the six measurements (strong colors) exhibit similar traces for reference and sample. The DRF flank at 283 GHz and the DRF minimum at 287 GHz have identical shapes. Both the flank and the minimum of the sample measurement are clearly shifted 0.5 GHz due to the loading with DNA strands.
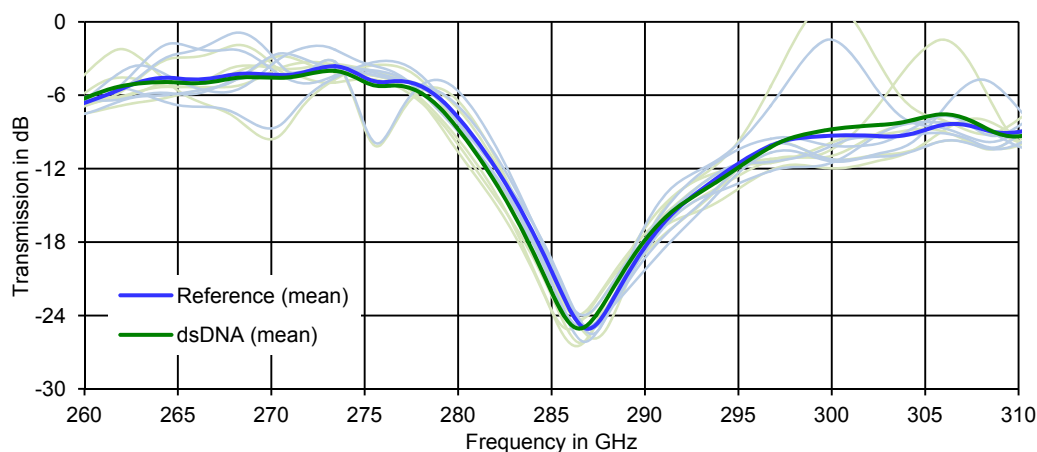
Figure 6-16: Measurements of a biochip with reference spot (blue) and sample spot with DNA loading (green). Individual measurements are in pale, means in strong color.

A single measurement is shown in Figure 6-17. The frequency shift of the DRF can clearly be seen for the flank as well as both extrema. The traces agree very well for the remaining spectrum. A THz-path interference results in a resonance feature at 275 GHz with a local maximum and minimum resembling the DRF shape. This feature is not shifted from reference to sample measurement because it is depending on the THz-path geometry only.
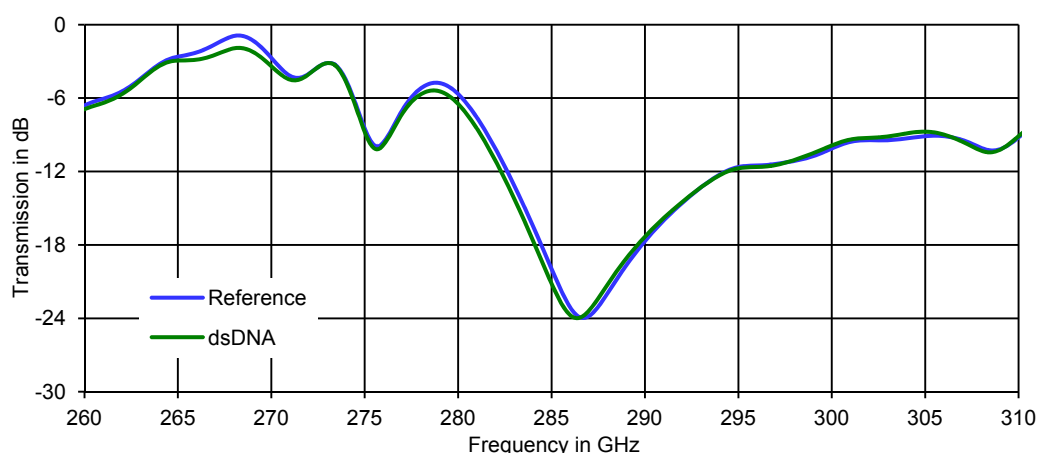
Figure 6-17: Exemplary measurement of a biochip with reference spot (blue) and sample spot with DNA loading (green).

6.3.3 Unsuccessful DNA Test Series

The biochip / reader technology is demonstrated detecting the presence of a dsDNA film functionalized to the gold surface in the undercut of the biochips. However, the ambition of this research is the detection of DNA binding states. This requires measurements of DNA

which is denatured and rehybridized on-chip. For this test series the simplified biochip sets produced in 2010 are available only. These chips do not have a chrome cover layer and the chrome in the undercut is not being removed. Thus, the DNA functionalization is supposed to be taking place on the full top metal surface. Again, the DNA is handled as described in chapter 6.3.1. The large array chip is logically divided into quarters (Figure 6-4) of which two are kept clean for reference and two are loaded with DNA. Different DNA sequences are used for the experiments. In addition to the random sequence "Oligo1/2" (Figure 6-18), which is also used for the successful experiment in 2009, DNA strands of beta-actin (Figure 6-19) and melanoma inhibitory activity (MIA) (Figure 6-20) are applied, both being markers for certain types of cancer.[Bos97, Loh12]

The measurements clearly do not show any frequency shift after the DNA functionalization process.
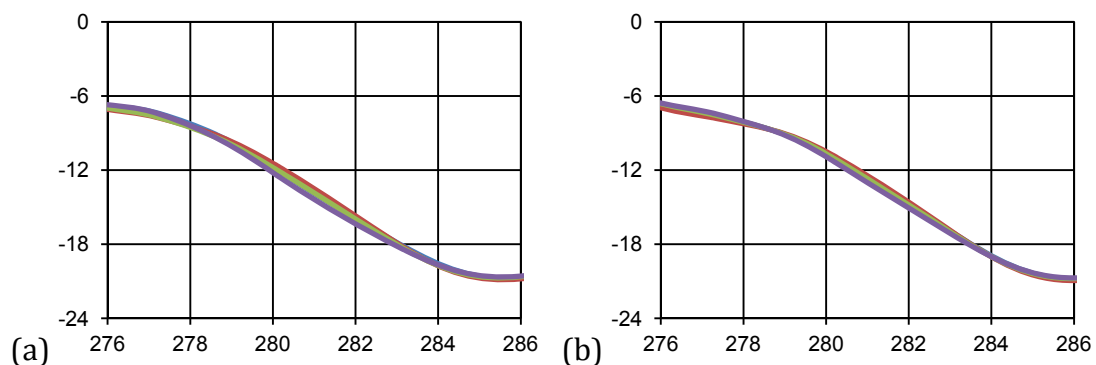
Figure 6-18: Transmission in dB over Frequency in GHz of a measurement of a biochip (a) before and (b) after DNA functionalization process with random sequence "Oligo1/2". Spots 1 (blue) and 2 (red) are sample spots. Spots 3 (green) and 4 (violet) are references. (Chip „June 2010 series 4 B")
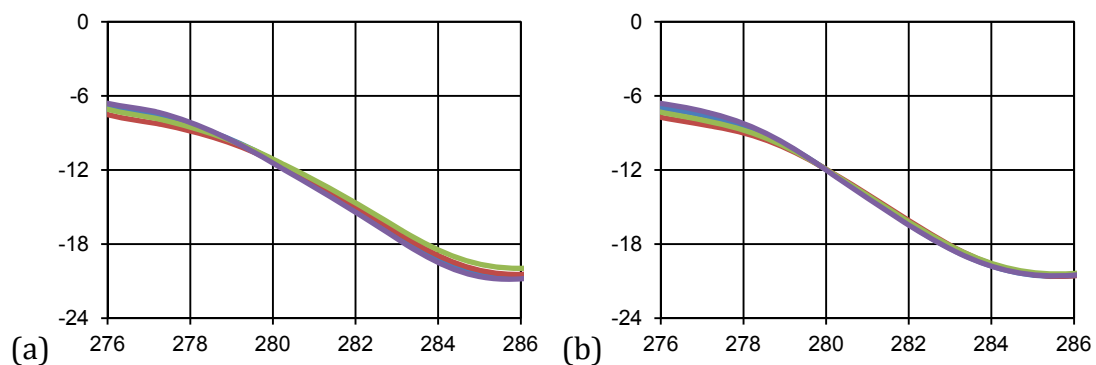
Figure 6-19: Transmission in dB over Frequency in GHz of a measurement of a biochip (a) before and (b) after DNA functionalization process with „Beta-Actin". Spots 1 (blue) and 3 (green) are sample spots. Spots 2 (red) and 4 (violet) are references. (Chip „June 2010 series 4 A")
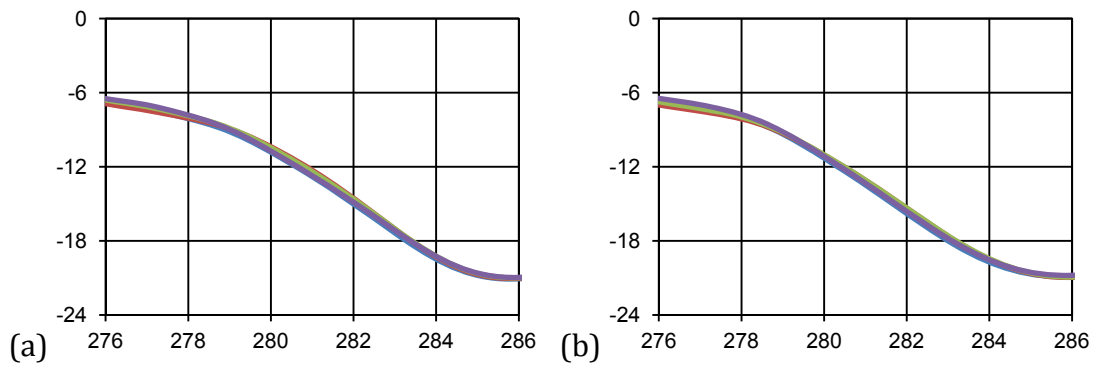
Figure 6-20: Transmission in dB over Frequency in GHz of a measurement of a biochip (a) before and (b) after DNA functionalization process with „MIA". Spots 1 (blue) and 3 (green) are sample spots. Spots 2 (red) and 4 (violet) are references. (Chip „June 2010 series 4 C")

Since the 2009 experiment with "Oligo1/2" shows a significant frequency shift it is highly implausible that nothing appears to happen in the 2010 experiment. New solutions are prepared and the functionalization process is performed under different ambient conditions. Components which are about to be combined are brought to identical temperatures before being brought into contact. The functionalization is made in a humid ambient. Different tools (teflon instead of metal) are used for handling. Despite these efforts, no experiment leads to a measurable frequency shift, leaving two possible explanations: Either the functionalization process in 2010 is not working, so that there is no DNA connected to the biochip and thus no frequency shift. Or the DNA is on the biochip but its amount or the effect on the resonant frequency is too small to be measured with the biochip reader.
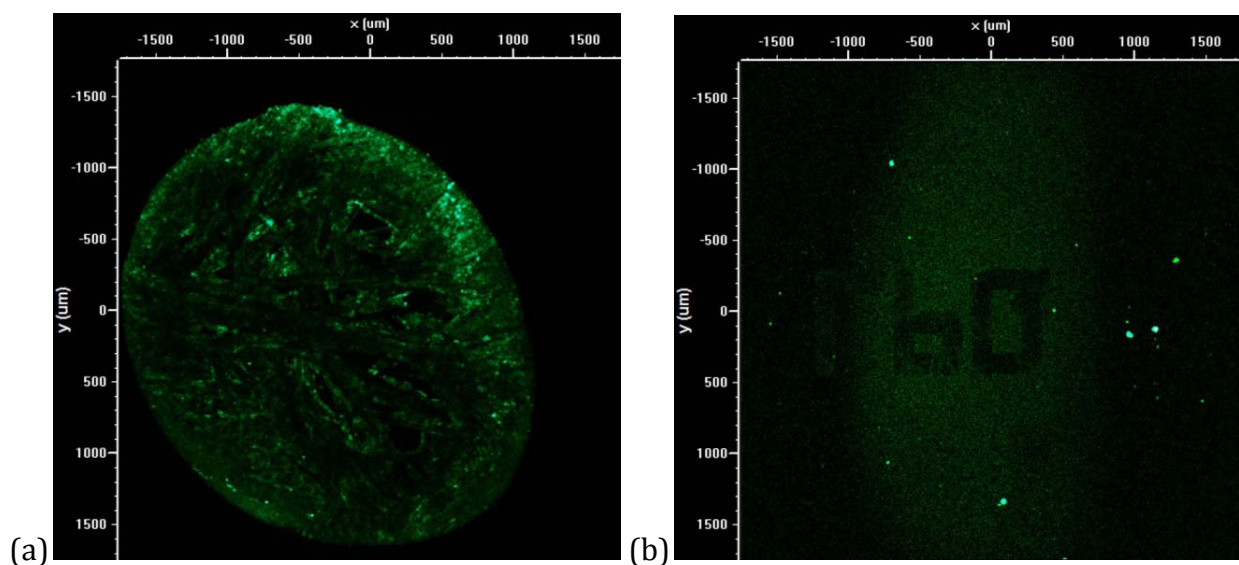
Figure 6-21: Microscope photos of a biochip from the unsuccessful experiments illuminated with 485 nm to excite the fluorescent marker at 514 nm. (a) A drying drop of DNA in solution with brightness from fluorescence at the rim. (b) After purging the chip with DI-water no marker is seen, only some artifacts from dirt particles and the weak illumination.

The complementary DNA strands are labeled with a fluorescent marker. Although the purpose of this research is a label-free technology, the markers are added for double-checking. Since the biochip experiences no frequency shift there should be no fluorescence

from the DNA on the gold surface. A 1.5 µl droplet is deposited at a position of the biochip where the gold surface is predominantly continuous. The structured inscription "LPQ" is used for orientation. The droplet clearly shows fluorescence, the brighter the closer to the rim (Figure 6-21(a)). This proves the marker to be functional only, but not whether the strands are hybridized or bound to the surface. After purging the surface with DI-water the salt from the buffer solution is removed and a thin-film of DNA is supposed to cover the gold. As Figure 6-21(b) shows, no fluorescence appears. The illumination and dirt particles are seen only. If the DNA is bound to the surface the marker is not further away from the gold as 4 nm. Admittedly, in this low distance the gold quenches the fluorescence, which might be a reason why it may not be seen even if it actually was there.

Although the amount of DNA is very low and the film thickness small compared to the chip thickness, another investigation method is tried to determine the presence of organic material on the biochip. Energy-dispersive X-ray spectroscopy (EDX) at a low-energy mode is utilized to search the surface for substances. The part of the biochip mostly excited by EDX is the gold-layer, since the technology is measuring into a certain depth. The thin DNA-film, if any, makes a small difference but adds new chemical element peaks to the spectrum, such as phosphor. The EDX-spectra of the reference and the sample spot are shown in Figure 6-22 with almost no noticeable difference. Especially, no additional peaks appear for the sample spectrum.
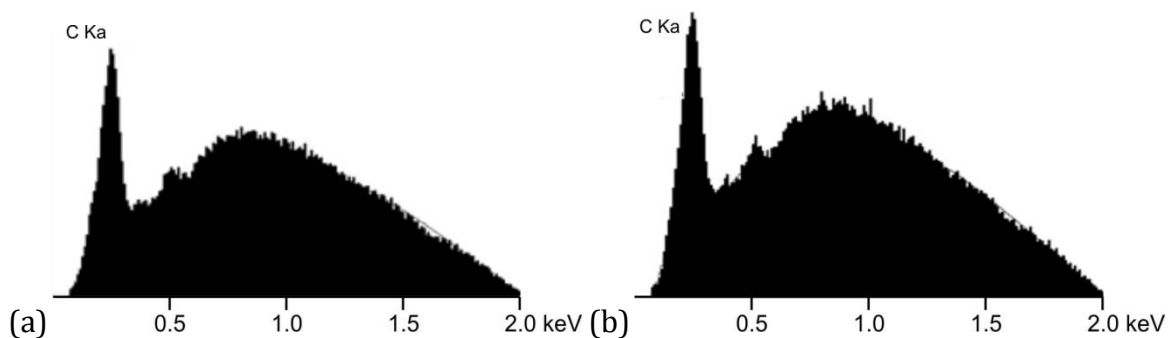
Figure 6-22: EDX spectra of a loaded biochip's (a) reference and (b) sample spot, with almost identical results. (Peaks for Au appear at higher energy levels.)

The search of a DNA film by fluorescence and EDX is clearly at the detection limit of these techniques. Several measurements are performed with different chips and handling procedures. Since all of these experiments show a clean surface without any doubt, it is obvious that the functionalization process has failed. Further investigation is required to find out whether the surface linking has failed, the prepared DNA changed due to aging, or other biochemical effects took place. However, for a satisfactory solution, specific expertise in the field of DNA handling and functionalization is required, going beyond the limits of this dissertation.

7 Conclusion

Thin-film sensing is a THz-application developing in various directions. Several approaches (e.g. waveguides, surfaces) utilizing different physical phenomena (e.g. reflections, resonances, plasmons) are being investigated by research groups mostly with electronics and physics background. Hence, the results of thin-film sensing experiments are almost entirely generated with films of arbitrary dielectric materials and more or less unspecified applications. The competition appears to be about the detection of the thinnest film. Deviating from this, the detection of DNA aims for the lowest total number of molecules, while the film thickness depends on the type of DNA samples. But the biochips fit into the context of thin-film sensing, since a film of short DNA strands has a thickness in the sub-μm range and the measured quantity in both cases is the refractive index or permittivity, respectively. Other approaches, as reviewed in chapter 2, are appropriate in the μm-range, whereas the presented biochip has proven to be capable of detecting films with less than 100 nm of thickness.

The working principle of the developed biochip is the frequency shift of a resonator due to dielectric loading being the deposition of dielectric material in the E-field vicinity of the resonator. The detection of small frequency shifts requires a high Q-factor to distinguish between close resonances clearly. The dual resonance feature (DRF) of the asymmetric double-split ring resonator (aDSR) exhibits a steep flank in the frequency spectrum corresponding to a high Q-factor. Additionally, the E-field is concentrated at characteristic locations rendering the need for full surface covering with sample material. This combination, including the capability of free-space accessibility, makes the frequency selective surface (FSS) with aDSRs a successful choice for high-sensitivity biochips.

Transferring the theoretically optimized split-rings to real biochips involves the choice of materials. Gold as the conductive material exhibits a high conductivity improving the Q-factor and can be used for localized functionalization being the technology to attach DNA molecules to the biochip at the characteristic locations of high E-field concentration. It is chemically resistant and well established in microfabrication technology. The undercut being a grove in the substrate below the resonator edges improves the resonance and the sensitivity if the sample is deposited here. Quartz-glass substrates enable the elegant preparation of the metal in the undercut by lithography exposure from the backside. Quartz-glass, or fused silica, is available as wafers; Again the microtechnology processing is well-known, and the handling is comparable to those of microscope slides. Hence, quartz-glass substrates are more likely to excite industrial interest as the more scientific and more expensive silicon wafers.

For the understanding, designing, and optimization of the aDSR extensive numerical simulation series are performed with the full-wave EM-field solver HFSS in the frequency domain. The resonance behavior of a symmetric ring (base mode) is found to be similar to a $\lambda/2$-dipole antenna. The resonant frequency is primarily depending on the ring's circumference while line width and height have a small influence only. Becoming asymmetric the resonator exhibits the DRF at a frequency below the base mode. The steepness and the

height of the DRF flank strongly depend on the E-field distribution at the gaps, and therefore especially on the asymmetry angles and the substrate's refractive index. The aDSR resonance is also depending on the direction of the polarization of the incident THz-radiation. The biochip is designed for polarization parallel to the resonator arcs, but an alternative design of four center-symmetrically arranged aDSRs is developed behaving almost independent of the polarization direction. Finally, the coupling between neighbor elements of the resonator array (FSS) in both lateral directions has influence on the field distribution primarily. Taking into account the technological aspects given above, the aDSR is designed for a DRF at 280 GHz with a modulation of 22 dB within 11 GHz and a corresponding Q-factor $Q_\omega \approx 50$. The steep part (between the 3 dB-limits) of the DRF-flank measures 16 dB over 5 GHz.

The large-scale production of biochips in suitable factories is offered and presumed feasible at a reasonable quality. On the other hand, the manufacturing of small sets of biochips in the cooperating university laboratories turns out to be challenging. The lithography with a smallest feature size of 20 µm and the lift-off process for the complementary structure are more or less common practice. Even the anisotropic substrate etching is realized to produce homogeneous results. The crux of the matter lies in the removal of the chrome adhesive layer in the undercut. The metal layers and the photo resist have to be extremely clean. Even low contamination with particles results in defects in the metal layers after the chrome etching process. The first and successful measurements are performed with biochips as designed. Later the quality could not be maintained due to infrastructural issues. A simplified version of the biochip is used lacking the chrome cover layer and the chrome etching process. The DNA can only be attached to the top-side of the metal here (but the full surface), resulting in a lower interaction with the E-field. Thus the simplified biochips have a lower sensitivity with more sample material, but the performance is still sufficient for a proof of principle.

In theory the FSS is linearly scalable, meaning that reducing the structure size to the half doubles the resonant frequency. In practice this in an approximation only, because the model deviates from the idealized theory by losses, finite dimensions, and conductivity. Experiments with scaled FSSs indicate a deviation of approximately 4%. The biochip is manufactured with half of the size of the 280 GHz-version and a corresponding reader is built for read-out. The 560 GHz biochip is measured and its resonance behavior is confirmed.

The biochip, combined with a biochip reader being a fully electronic THz-spectrometer, forms a complete technology for THz-sensing of small amounts of material, such as DNA. Conventional THz-setups, such as the time domain spectroscopy (TDS), are laser-based. Regarding widespread application these systems are too slow, large, and expensive and require too much maintenance. The biochip reader measures a spectrum from 244 GHz to 318 GHz with 31 MHz resolution. 100 measurements are taken, averaged, processed and displayed in 110 ms. Filtering further reduces the noise coarsening the resolution to values still better than 0.5 GHz. A demonstrator setup is built to proof the feasibility of assembling a system from commercially available state-of-the-art components, which is acceptable for widespread usage in terms of speed, size, cost, and handling. The biochip reader generates a 12 to 18 Gigahertz baseband which is multiplied in consecutive diode-based mixers by a

factor of 18 reaching the required lower THz-range. The THz-radiation is transmitted by a horn antenna and quasi-optically guided by lenses. After transmission through the biochip it is received, subharmonically mixed down to the megahertz-range, and digitized for signal processing. The system works with one oscillator only, utilizing the THz-path delay to generate an intermediate MHz-frequency, thus enabling quasi-heterodyne detection.

Several experiments are performed to proof the technology to be working, to evaluate the sensitivity, and to indicate DNA-sensing capability. Very good agreement is found for the biochip's resonant frequency. The prediction from simulations and the measurements with the biochip reader deviate by 1 % only. The reader measurement is confirmed by TDS measurements with almost identical results. Biochips are covered with films of various substances to investigate the sensitivity of the system. Films in the µm-range, such as UV-dye and technical gelatin, cause significant frequency shifts. Thinner films made of a PMMA-based photo resist are not homogeneous due to the fact that the structures are deeper than the desired film-thickness. Although these films cannot be analyzed quantitatively, the PMMA-film experiments proof the system's ability of detecting low-ε films below 100 nm thickness. Comparable approaches with single split-ring resonators indicate a detection limit for thin-films in the THz-regime at 100 nm, even with a high permittivity.[OHa08] The aDSR-based biochip detects thinner films with a lower index of refraction.

Finally, the system is expected to detect DNA binding states. The measurements with gelatin and thin PMMA indicate a sufficient sensitivity for sub-100 nm DNA films. However, the DNA experiments exhibit more challenges. A first successful detection of DNA proves the functionality of this sensing technology. A loading of 0.4 fmol of random double-stranded DNA (20 basepairs long) per resonator, results in a frequency shift of approximately 0.5 GHz.

Direct comparison to the metasurface experiment of O'Hara et al. indicates a significantly lower detection limit for the FSS approach. The successful DNA measurement with the FSS biochip used 4730 µm² per resonator with a 4 nm thin film of DNA with $\varepsilon_r = 1.2$. The metasurface is composed of smaller resonators with 60 µm periodicity only, requiring approximately 48 units to cover the same surface as one aDSR. In their experiment with a full surface covering of barium oxide, 3600 µm² per resonator are utilized with a 100 nm thick film of $\varepsilon_r = 3.6$. Hence, the sample volume per resonator in the metasurface experiment is 20 times higher, 48 times as many resonators are active, and the sample permittivity is 3 times higher. In conclusion, the FSS is approximately 2900 times more sensitive than the metasurface, though localized functionalization on the metasurface would possibly decrease this advantage significantly.

A measurements series of DNA binding states was planned to supplement these results. Unfortunately, DNA measurements could not be performed successfully again to determine DNA binding states. The main issue in the analysis of this failure is the verification if or if not DNA is actually bound to the gold surface. No technology is available to verify DNA molecules bound in the undercut. Therefore, the possibility of an error in the first measurement cannot be excluded. The later experiments are performed with simplified biochips, where the DNA is

supposed to bind to the top surface. Various detection techniques could not identify the molecules there. It is unclear whether the DNA is not there, or partially present, as the amount may be too little to be seen. The functionalization of DNA to the gold surface and the handling of the required chemical substances are the most critical aspects in this experiment. Although instructions are available handling errors are possible. Especially the hydration and storage (several months at -24°C) of the DNA-strands is suspected to be have harmed the DNA or its thiol-linker. The first (successful) experiment is performed with high-quality biochips and fresh chemicals and DNA. However, the later (unsuccessful) experiments are subject to several handicaps. The biochip manufacturing takes place in a contaminated laboratory environment and the surface preparation is different to the earlier case. The ratio of molecules to open gold surface is much lower, and the DNA possibly aged in the cold storage. Several smaller issues combined usually cause a larger problem. It is therefore believed, that the experiment under good conditions actually is a successful detection of DNA, whereas the later experiments show no result because of a failed DNA functionalization.

The biochip based on a frequency selective surface assembled from asymmetric double-split ring resonators is a suitable device for the THz-detection of thin dielectric films. With its detection limit below 100 nm the biochip outclasses other approaches for THz-thin-film sensing. Despite the final experimental troubles, the verification activities prove the biochip to be able of detecting minute amounts of locally functionalized DNA, thus leaving the need for further investigation of biochemical aspects, such as DNA handling and functionalization. The combination of the biochip and the compact and fully electronic biochip reader system demonstrates that a complete technology for DNA-sensing can be made market-ready in conceivable time.

8 <u>Appendix</u>

8.1 <u>Symbols and Abbreviations</u>

ADC   analog to digital converter

aDSR   asymmetric double-split ring resonator

AFM   atomic force microscope

cw   continuous wave

DAC   digital to analog converter

DAQ   data acquisition hardware (analog/digital converter)

DI-water   deionized water (σ = 0.055 μS/cm)

DNA   deoxyribonucleic acid

dsDNA   double-stranded DNA

DUT   device under test

ε permittivity (real part, unless otherwise specified)

E-field   electric field

EDX   energy-dispersive X-ray spectroscopy

FFT   Fast Fourier Transform

FSS   frequency selective surface

IF   intermediate frequency

LO   local oscillator / fundamental frequency

n   refractive index (real part, unless otherwise specified)

PBC   periodic boundary condition (HFSS)

PET   polyethylene terephthalate / polyester

pec   perfect electronic conductor (HFSS: σ = 10^{30} S/m)

PML   perfectly matched layer (HFSS)

PMMA   polymethyl methacrylate / Plexiglas

PP   polypropylene

Q_ω Q-factor defined by 3dB-bandwidth[Zinke] ($Q_\omega = \omega_{res}/\Delta\omega$)

REM   raster electron microscopy

RF   radio frequency

Rx   receiver, here also: THz-detector

SEM   scanning electron microscopy

SiO$_2$ silicon dioxide

SRR   split-ring resonator

ssDNA   single-stranded DNA

TDS   time domain spectroscopy

TEM   transversal electro magnetic

Tx   transmitter, here also: THz-emitter / -source

UHF   ultra high frequency (300 MHz – 3 GHz)

VCO   voltage controlled oscillator

8.2 **FSS Designs**

280 GHz LP on silicon
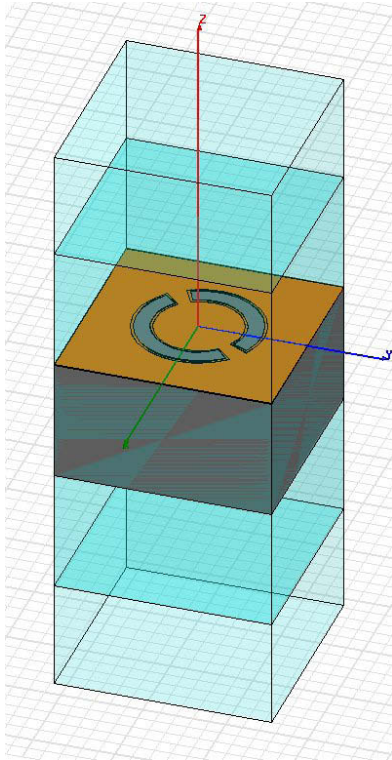
Simulation:
> PBC in **X**-, **Y**-direction
> PML in ±**Z**- direction
> 17752 tetrahedra

cellsize:	263µm x 263µm
inner radius:	56µm
outer radius:	76µm
gold-layer thickness:	200nm
offset angle:	8°
gap angle:	22°
undercut width:	3µm

substrate (silicon)
> thickness: 150µm
> ε_r = 11.78, tan δ = 0.0001
> oxide-layer: 500nm
> ε_r = 3.8

sample (DNA)
> thickeness: 100nm
> εr = 2.6, tan δ = 0.001, σ = 100kS/m
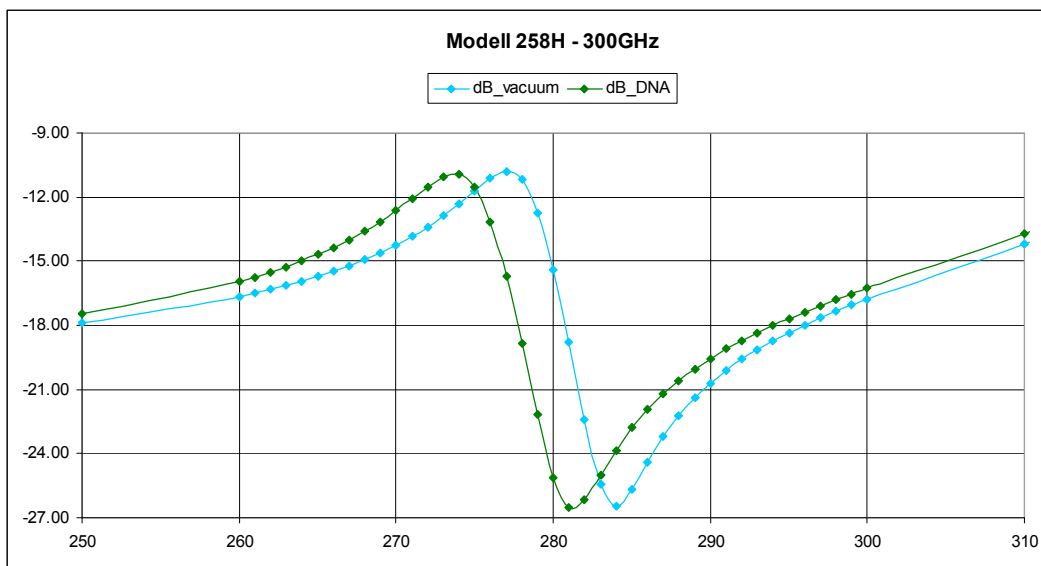
Figure 8-1: The DRF of the 280 GHz LP design shows a frequency shift of 3 GHz upon loading with DNA, corresponding to an amplitude shift of 10 dB at 280 GHz.

280 GHz LP on quartz-glass
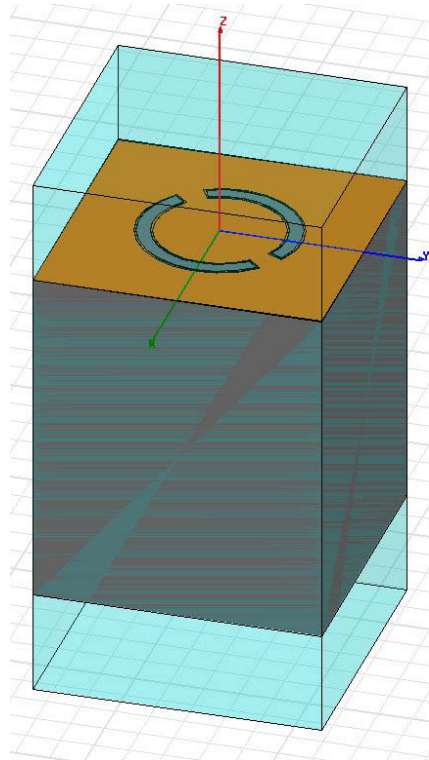
Simulation:

    PBC in **X**-, **Y**-direction
    PML in ±**Z**- direction
    17070 tetrahedra

cellsize: 416µm x 416µm
inner radius: 96µm
outer radius: 116µm
gold-layer thickness: 200nm
offset angle: 8°
gap angle: 22°
undercut width: 3µm

substrate (quartz-glass)
    thickness: 500µm
    ε_r = 3.81, tan δ = 0.0001
    „etch-layer":   500nm
    ε_r = 3.81

sample (DNA)
    thickeness: 100nm
    ε_r = 2.6, tan δ = 0.001, σ = 100kS/m
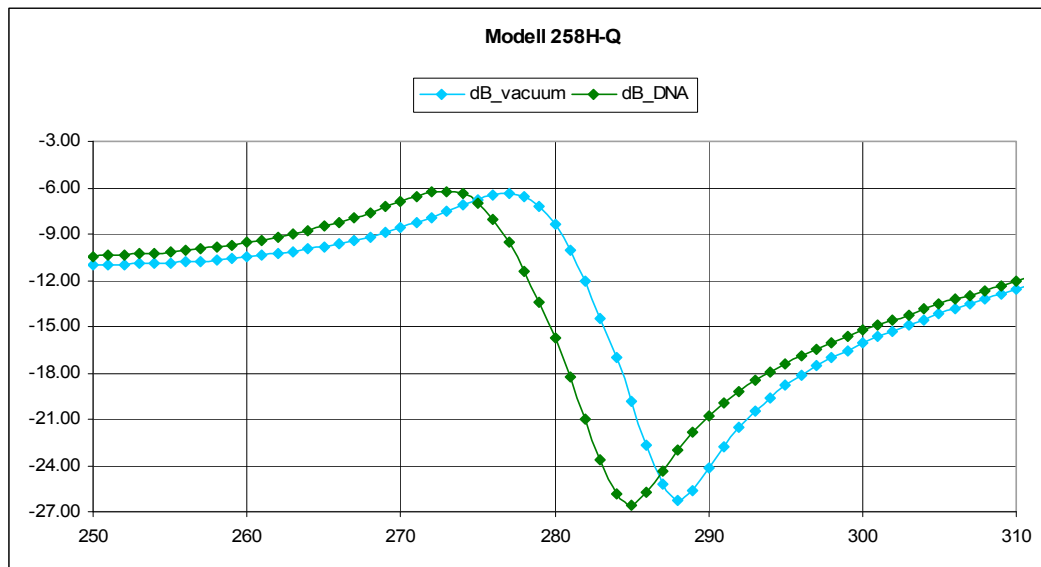
Figure 8-2: The DRF of the 280 GHz LP design shows a frequency shift of 3 GHz upon loading with DNA, corresponding to an amplitude shift of 9 dB at 283 GHz.

280 GHz ZS on quartz-glass
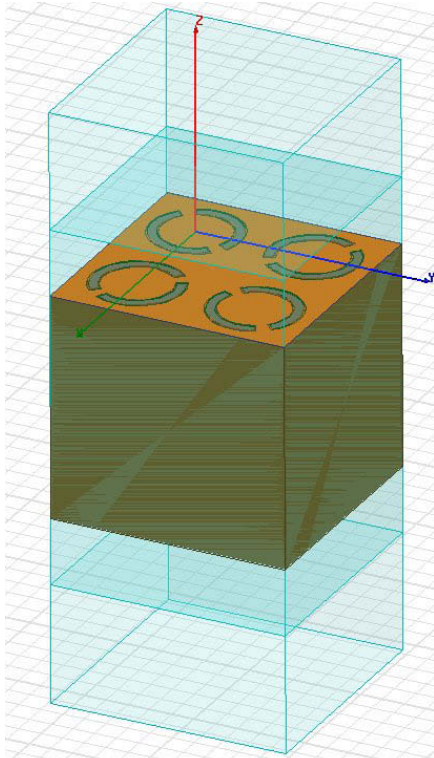
Simulation:
    PBC in X-, Y-direction
    PML in ±Z- direction
    89577 tetrahedra

cellsize: 2·265µm x 2·265µm
inner radius: 80µm
outer radius: 100µm
gold-layer thickness: 200nm
offset angle: 8°
gap angle: 22°
undercut width: 3µm

substrate (quartz-glass)
    thickness: 500µm
    ε_r = 3.81, tan δ = 0.0001
    „etch-layer":   500nm
    ε_r = 3.81

sample (DNA)
    thickeness: 100nm
    ε_r = 2.6, tan δ = 0.001, σ = 100kS/m
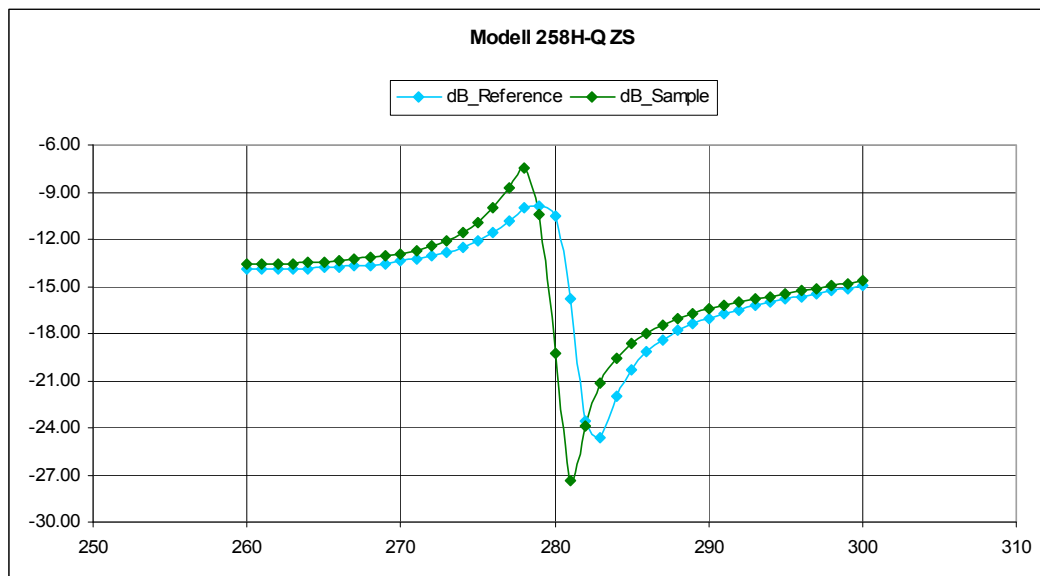
Figure 8-3: The DRF of the 280 GHz LP design shows a frequency shift of 1.5 GHz upon loading with DNA, corresponding to an amplitude shift of 10 dB at 283 GHz.

8.3 FSS on PET-foil

The first series of FSS is made from gold on PET substrate. Variations of positive and complementary designs are included on one lithography mask. The substrate becomes bumpy during the heating-steps in the lithography process and the thin lines of the positive structures are easily detached from the substrate. Only the complementary structures can be produced reproducibly.

The mask is designed with AutoCAD and produced by ML&C GmbH, Jena. The substrate is Mylar (biaxially-oriented polyethylene terephthalate PET) from Goodfellow GmbH, Bad Nauheim with 50 μm thickness. A 15 nm chrome adhesive layer and 400 nm gold are deposited by sputtering at the Institute for Microsystem Technology, University of Siegen. As an alternative a 20 nm titanium adhesive layer and 400 nm gold are deposited with electron beam physical vapor deposition (EBPVD) at the Institute of Semiconductor Electronics, RWTH Aachen. The structures are wet-etched in a lift-off process with AZ5214E photo resist at the Institute for Microsystem Technology, University of Siegen.

8.4 **Biochip Production Logs**

Complementary FSS on silicon substrate:

step	action
1	thermal oxidation
2	photo-resist spin-on
3	mask exposure
4	developing, removing then: rinsing with DI-water, drying with nitrogen flow
5	plasma cleaning
6	metallization (10nm Cr, 200nm Au, 10nm Cr)
7	lift-off then: rinsing with propanol and DI-water, drying in nitrogen flow
8	SiO_2 dry etch (reactive ion etching RIE)
9	SiO_2 chemical wet etch then: rinsing with DI-water, drying with nitrogen flow
10*	photo-resist spin-on
11*	mask exposure
12*	developing, removing then: rinsing with DI-water, drying with nitrogen flow
13*	crome etch then: rinsing with DI-water, drying with nitrogen flow
14	resist layer spin-on for protection
15	chip separation (wafer dicing saw)
16	remove protection resist in acetone then: rinsing with propanol and DI-water, drying in nitrogen flow

* required to protect the chrome cover layer, while removing chrome in the undercut

Complementary FSS on quartz-glass substrate with backside exposure:

step	action
1	photo-resist spin-on
2	mask exposure
3	developing, removing then: rinsing with DI-water, drying with nitrogen flow
4	plasma cleaning
5	metallization (10nm Cr, 200nm Au, 10nm Cr)
6	lift-off then: rinsing with propanol and DI-water, drying in nitrogen flow
7	quartz chemical wet etch then: rinsing with DI-water, drying with nitrogen flow
8*	photo resist spin-on
9*	exposure from the backside
10*	developing, removing then: rinsing with DI-water, drying with nitrogen flow
11*	crome etch then: rinsing with DI-water, drying with nitrogen flow
12	resist layer spin-on for protection
13	chip separation (wafer dicing saw)
14	remove protection resist in acetone then: rinsing with propanol and DI-water, drying in nitrogen flow

* required to protect the chrome cover layer, while removing chrome in the undercut

8.5 DNA-Handling Recipe

Chemicals and Abbreviations:

substance	abbreviation	provider
sodium chloride	"NaCl"	Merck, Darmstadt, D
(tris-(hydroxymethyl)animomethane-hydrochloride	"Tris-HCl"	Sigma, Steinheim, D
ethylenediaminetetraacetic acid	"EDTA"	Sigma-Aldrich, Gillingham, UK
potassium dihydrogen phosphate	"KH_2PO_4"	Merck, Darmstadt, D
6mercapto-1hexanol	"MCH"	Fluka, Buchs, CH

Buffer-Solution "TE-NaCl":

The buffer-solution is prepared at room temperature adding the following substances to DI-water constantly stirring:

	concentration c	molecular weight M	mass m (for 0.1l)
NaCl	1000 mmol/l	58.442 g/mol	5,844.20 mg
Tris-HCl	10 mmol/l	121.135 g/mol	121.14 mg
EDTA	1 mmol/l	292.240 g/mol	29.22 mg

Hybridization:

The DNA is bought from Eurofins MWG Operon, Ebersberg, in dried single strands. The "random DNA" is a set of oligonucleotide of 20 bases with the sequences

"Oligo1": `5'-thiol- ACACTGTGCCCATCTACGAG -3'`

"Oligo2": `5'- TGTGACACGGGTAGATGCTC -fluo-3'`

"Oligo1" and "Oligo2" are complementary DNA strands which are hybridized before immobilization. Each type is hydrated with DI-water and diluted with TE-NaCl. 5 ml buffer solution with 1 µmol/l DNA is tempered at 50 °C for 12 h resulting in 1 µmol/l dsDNA "Oligo1/2" in buffer-solution.

Immobilization:

For Immobilization KH_2PO_4 is added to the buffer-solution with DNA at a concentration of 1 mol/l (M = 136.09 g/mol, m = 680.5 mg for 5 ml immobilization solution). This immobilization solution is deposited on the biochip at room temperature for 60 min. The chip is then thoroughly purged with DI-water to remove all components from the buffer-solution. The dsDNA is now bound to the gold-surface.

Denaturation:

The biochip with immobilized DNA is tempered in TE-NaCl at 60 °C for 60 min. After purging with TE-NaCl to remove the complementary strands, the chip is cleaned with DI-water. Now the biochip contains ssDNA only bound to surface, the chip is functionalized.

Rehybridization / Sample deposition

The sample ssDNA strands will bind to the immobilized strands if they are complementary. The sample DNA is given in buffer-solution at 1 µmol/l. Additionally, MCH is added at 1 mmol/l (M = 134.24 g/mol, V = 14.11 µl for 5 ml rehybridization solution) to improve sample acceptance by the immobilized strands. Again the solution is deposited on the biochip's sample spots at 50 °C for 60 min.

Bibliography

[Alber]   B. ALBERTS, D. BRAY, J. LEWIS, M. RAFF, K. ROBERTS, & J. D. WATSON, *Molekularbiologie der Zelle*, VCH (1997).

[aWe09]   C. AM WEG, W. VON SPIEGEL, R. HENNEBERGER, R. ZIMMERMANN, T. LOEFFLER, & H. G. ROSKOS, *Fast Active THz Cameras with Ranging Capabilities*, Journal of Infrared, Millimeter and Terahertz Waves 30(12), pp. 1281–1296 (2009).

[Aka03]   Y. AKAHANE, T. ASANO, B.-S. SONG, & S. NODA, *High-Q photonic nanocavity in a two-dimensional photonic crystal*, Nature 425, pp. 944-947 (2003).

[Balan]   C. A. BALANIS, *Advanced Engineering Electromagnetics 2nd ed.*, John Wiley & Sons (2012).

[Bar03]   T. BARAS, T. KLEINE-OSTMANN, & M. KOCH, *On-Chip THz Detection of biomaterials: A Numerical Study*, Journal of Biological Physics 29(2-3), pp. 187-194 (2003).

[Bax11]   J. B. BAXTER & G. W. GUGLIETTA, *Terahertz Spectroscopy*, Analytical Chemistry 83(12), pp. 4342–4368 (2011).

[Bel09]   M. A. BELKIN, Q. J. WANG, C. PFLÜGL, A. BELYANIN, S. P. KHANNA, A. G. DAVIES, E. H. LINFIELD, & F. CAPASSO, *High-Temperature Operation of Terahertz Quantum Cascade Laser Sources*, IEEE Journal of Selected Topics in Quantum Electronics 15(3), pp. 957-962 (2009).

[Bit11]   A. BITZER, A. ORTNER, H. MERBOLD, T. FEURER, & M. WALTHER, *Terahertz near-field microscopy of complementary planar metamaterials: Babinet's principle*, Optics Express 19(3), pp. 2537-2545 (2011).

[Böhme]   E. BÖHMER, *Elemente der angewandten Elektronik*, Vieweg (2000).

[Bos97]   A.-K. BOSSERHOFF, M. KAUFMANN, B. KALUZA, I. BARTKE, H. ZIRNGIBL, R. HEIN, W. STOLZ, & R. BUETTNER, *Melanoma-inhibiting Activity, a Novel Serum Marker for Progression of Malignant Melanoma*, Cancer Research 57(15), pp. 3149-3153 (1997).

[Bru00]   M. BRUCHERSEIFER, M. NAGEL, P. HARING BOLIVAR, & H. KURZ, *Label-free probing of the binding state of DNA by time-domain*, Applied Physics Letters 77(24), pp. 4049-4051 (2000).

[Bru02]   M. BRUCHERSEIFER, P. HARING BOLIVAR, & H. KURZ, *Combined optical and spatial modulation THz-spectroscopy for the analysis of thin-layered systems*, Applied Physics Letters 81(10), pp. 1791-1793 (2002).

[Bur54]   C. A. BURRUS & W. GORDY, *Submillimeter Wave Spectroscopy*, Physical Review 93(4), pp. 897–898 (1954).

[Campb]   S. A. CAMPBELL, *The science and engineering of microelectronic fabrication*, Oxford University Press (1996).

[Cas09]   E. CASTRO-CAMUS & M. B. JOHNSTON, *Extraction of the anisotropic dielectric properties of materials from polarization-resolved terahertz time-domain spectra*, Journal of Optics A: Pure and Applied Optics 11(10), 105206 (2009).

[Che07]   H. CHEN, L. WANG, Y. QU, T. KUANG, L. LI, & W. PENG, *Investigation of guanidine hydrochloride induced chlorophyll protein 43 and 47 denaturation in the terahertz frequency range*, Journal of Applied Physics 102(7), 074701 (2007).

[Coo06]   M. A. COOPER, *Opticalbiosensors: where next and how soon?*, Drug Discovery Today 11(23-24), pp 1061‑1067 (2006).

[Coo08]   K. B. COOPER, R. J. DENGLER, G. CHATTOPADHYAY, E. SCHLECHT, J. GILL, A. SKALARE, I. MEHDI, & P. H. SIEGEL, *A High-Resolution Imaging Radar at 580 GHz*, IEEE Microwave and Wireless Components Letters 18(1), pp. 64-66 (2008).

[Deb06]   C. DEBUS, *Frequenzselektive Oberflächen im Terahertz-Frequenzbereich*, diploma thesis, university of Siegen (2006).

[Deb07]   C. DEBUS & P. HARING BOLIVAR, *Frequency selective surfaces for high sensitivity terahertz sensing*, Applied Physics Letters 91(18), 184102 (2007).

[Deb08]   C. DEBUS & P. HARING BOLIVAR, *Terahertz biosensors based on double split ring arrays*, Proceedings of SPIE 6987, 69870U (2008).

[Deb09]   C. DEBUS, P. HARING BOLIVAR, M. AWAD, & M. NAGEL, *Terahertz Biochip Technology: Toward High-Sensitivity Label-Free DNA Sensors*, American Biotechnology Laboratory 27(6), pp. 8-11 (2009).

[Deb11]   C. DEBUS, G. SPICKERMANN, M. NAGEL, & P. HARING BOLIVAR, *All-Electronic Terahertz Spectrometer for Biosensing*, Microwave and Optical Technology Letters 53(12), pp. 2899-2902 (2011).

[Den08]   A. J. DENINGER, T. GÖBEL, D. SCHÖNHERR, T. KINDER, A. ROGGENBUCK, M. KÖBERLE, F. LISON, T. MÜLLER-WIRTS, & P. MEISSNER, *Precisely tunable continuous-wave terahertz source with interferometric frequency control*, Review of Scientific Instruments 79(4), 044702 (2008).

[DLu03]   F. C. DE LUCIA, *Spectroscopy in the Terahertz Spectral Region*, in D. Mittleman (Ed.), Sensing with Terahertz Radiation, pp. 39-115, Springer (2003).

[Dri07]   T. DRISCOLL, G. O. ANDREEV, D. N. BASOV, S. PALIT, S. Y. CHO, N. M. JOKERST, & D. R. SMITH, *Tuned permeability in terahertz split-ring resonators for devices and sensors*, Applied Physics Letters 91(6), 062511 (2007).

[Eleft]   G. V. ELEFTHERIADES & K. G. BALMAIN, *Negative-Refraction Metamaterials*, John Wiley & Sons (2005).

[Fal04]   F. FALCONE, T. LOPETEGI, M. A. G. LASO, J. D. BAENA, J. BONACHE, M. BERUETE, R. MARQUÉS, F. MARTÍN, & M. SOROLLA, *Babinet Principle Applied to the Design of Metasurfaces and Metamaterials*, Physical Review Letters 93(19), 197401 (2004).

[Fed05]   J. F. FEDERICI, B. SCHULKIN, F. HUANG, D. GARY, R. BARAT, F. OLIVEIRA, & D. ZIMDARS, *THz imaging and sensing for security applications—explosives, weapons and drugs*, Semiconductor Science and Technology 20, pp. S266–S280 (2005).

[Fed07]   V. A. FEDOTOV, M. ROSE, S. L. PROSVIRNIN, N. PAPASIMAKIS, & N. I. ZHELUDEV, *Sharp Trapped-Mode Resonances in Planar Metamaterials with a Broken Structural Symmetry*, Physical Review Letters 99(14), 147401 (2007).

[Fin99]   H.-W. FINK & C. SCHÖNENBERGER, *Electrical conduction through DNA molecules*, Letters to Nature 398, pp. 407-410 (1999).

[Fis02]   B. M. FISCHER, M. WALTHER, & P. U. JEPSEN, *Far-infrared vibrational modes of DNA components*, Physics in Medicine and Biology 47, pp. 3807-3814 (2002).

[Fis05]   B. FISCHER, M. HOFFMANN, H. HELM, G. MODJESCH, & P. U. JEPSEN, *Chemical recognition in terahertz time-domain spectroscopy and imaging*, Semiconductor Science and Technology 20, pp. S246-S253 (2005).

[Frans]   S. FRANSSILA, *Introduction to microfabrication*, John Wiley & Sons (2004).

[Gay02]   P. GAY-BALMAZ & O. J. F. MARTINA, *Electromagnetic resonances in individual and coupled split-ring resonators*, Journal of Applied Physics 92(5), pp. 2929-2936 (2002).

[Geb10]   R. GEBS, P. KLOPP, G. KLATT, T. DEKORSY, U. GRIEBNER, & A. BARTELS, *Time-domain terahertz spectroscopy based on asynchronous optical sampling with femtosecond semiconductor disk laser*, Electronics Letters 46(1), pp. 75-76 (2010).

[Gel08]   B. GELMONT, R. PARTHASARATHY, & T. GLOBUS, *Edge Effects in Propagation of Terahertz Radiation in Subwavelength Periodic Structures*, Semiconductors 42(8), pp. 924–930 (2008).

[Gel10]   R. M. GELFAND & H. MOHSENI, *Design of a plasmonic photonic crystal for single bio-molecule spectroscopy*, Proceedings of SPIE 7759, 775907 (2010).

[Glo02] T. R. GLOBUS, D. L. WOOLARD, A. C. SAMUELS, B. L. GELMONT, J. HESLER, T.W. CROWE, & M. BYKHOVSKAIA, *Submillimeter-wave Fourier transform spectroscopy of biological macromolecules*, Journal of Applied Physics 91(9), pp. 6105-6113 (2002).

[Gri90] D. GRISCHKOWSKY, S. KEIDING, M VAN EXTER, & C. FATTINGER, *Far-infrared time-domain spectroscopy with terahertz beams of dielectrics and semiconductors*, Journal of the Optical Society of America B 7(10), pp. 2006-2015 (1990).

[Gup91] S. GUPTA, M. Y. FRANKEL, J. A. VALDMANIS, J. F. WHITAKER, G. A. MOUROU, F. W. SMITH, & A. R. CALAWA, *Subpicosecond carrier lifetime in GaAs grown by molecular beam epitaxy at low temperatures*, Applied Physics Letters 59(25), pp. 3276-3278 (1991).

[Haefe] R. A. HAEFER & B. ILSCHNER, *Oberflächen- und Dünnschicht-Technologie Teil 1 Beschichtung von Oberflächen*, Springer (1987).

[Har81] W. N. HARDY & L. A. WHITEHEAD, *Split-ring resonator for use in magnetic resonance from 200-2000 MHz*, Review of Scientific Instruments 52(2), pp. 213-216 (1981).

[Har99] P. HARING BOLIVAR, *Coherent terahertz spectroscopy*, in A. Miller et al., Semiconductor quantum optoelectronics, pp. 151- 191, Taylor & Francis (1999).

[Har02] P. HARING BOLIVAR, M. BRUCHERSEIFER, M. NAGEL, H. KURZ, A. BOSSERHOFF, & R. BÜTTNER, *Label-free probing of genes by time-domain terahertz sensing*, Physics in Medicine and Biology 47, pp. 3815–3821 (2002).

[Har04] P. HARING BOLIVAR, M. NAGEL, F. RICHTER, M. BRUCHERSEIFER, H. KURZ, A. BOSSERHOFF, & R. BÜTTNER, *Label-free THz sensing of genetic sequences: towards 'THz biochips'*, Philosophical Transactions of the Royal Society A 362, pp. 323–335 (2004).

[Has11] A. M. HASHIM, F. MUSTAFA, S. F. ABD RAHMAN, & A. R. ABDUL RAHMAN, *Dual-Functional On-Chip AlGaAs/GaAs Schottky Diode for RF Power Detection and Low-Power Rectenna Applications*, Sensors 11(8), pp. 8127-8142 (2011).

[Hei11] M. S. HEIMBECK, M. K. KIM, D. A. GREGORY, & H. O. EVERITT, *Terahertz digital holography using angular spectrum and dual wavelength reconstruction methods*, Optics Express 19(10), pp. 9192-9200 (2011).

[Heilm] A. HEILMANN, *Antennen (Erster Teil)*, Bibliographisches Institut (1970).

[Hel83] P. HELMINGER, J. K. MESSER, & F. C. DE LUCIA, *Continuously tunable coherent spectroscopy for the 0.1-1.0-Thz region*, Applied Physics Letters 42(4), pp. 309-310 (1983).

[Her97] T. M. HERNE & M. J. TARLOV, *Characterization of DNA Probes Immobilized on Gold Surfaces*, Journal of the American Chemical Society 119(38), pp. 8916-8920 (1997).

[hfss] *HFSS Online Help*, Ansoft HFSS 13 (2010).

[Hir04] H. HIRORI, K. YAMASHITA, M. NAGAI, & K. TANAKA, *Attenuated Total Reflection Spectroscopy in Time Domain Using Terahertz Coherent Pulses*, Japanese Journal of Applied Physics 43(10A), pp. L1287‑L1289 (2004).

[Höl08] R. HÖLZEL, *Dielectric and dielectrophoretic properties of DNA*, IET Nanobiotechnology 3(2), pp. 28-45 (2008).

[Irene] E. A. IRENE, *Surfaces, interfaces, and thin films for microelectronics*, John Wiley & Sons (2008).

[Jas10] C. JASTROW, S. PRIEBE, B. SPITSCHAN, J. HARTMANN, M. JACOB, T. KÜRNER, T. SCHRADER, & T. KLEINE-OSTMANN, *Wireless digital data transmission at 300 GHz*, Electronics Letters 46(9), pp. 661-663 (2010).

[Jia00] Z. JIANG, M. LI, & X.-C. ZHANG, *Dielectric constant measurement of thin films by differential time-domain spectroscopy*, Applied Physics Letters 76(22), pp. 3221-3223 (2000).

[Jin] J. JIN, *The Finite Element Method in Electromagnetics*, John Wiley & Sons (2002).

[Joh06]   N. P. JOHNSON, A. Z. KHOKHAR, H. M. H. CHONG, R. M. DE LA RUE, & S. MCMEEKIN, *Characterisation at infrared wavelengths of metamaterials formed by thin-film metallic split-ring resonator arrays on silicon*, Electronics Letters 42(19), pp. 1117-1119 (2006).

[Joh07]   N. P. JOHNSON, A. Z. KHOKHAR, B. LAHIRI, S. MCMEEKIN, R. M. DE LA RUE, C. DEBUS, & P. HARING BOLIVAR, *Recent Advances in Photonic Crystals and Metamaterials*, 9th International Conference on Transparent Optical Networks, Rome (Italy) (2007).

[Joh72]   P. B. JOHNSON & R. W. CHRISTY, *Optical Constants of the Noble Metals*, Physical Review B 6(12), pp. 4370-4379 (1972).

[Kap10]   B. KAPILEVICH, Y. PINHASI, R. ARUSI, M. ANISIMOV, D. HARDON, B. LITVAK, & Y. WOOL, *330 GHz FMCW Image Sensor for Homeland Security Applications*, Journal of Infrared, Millimeter and Terahertz Waves 31(11), pp. 1370–1381 (2010).

[Kim10]   Y. KIM & D.-S. YEE, *High-speed terahertz time-domain spectroscopy based on electronically controlled optical sampling*, Optics Letters 35(22), pp. 3715-3717 (2010).

[Kla09]   G. KLATT, R. GEBS, C. JANKE, T. DEKORSY, & A. BARTELS, *Rapid-scanning terahertz precision spectrometer with more than 6 THz spectral coverage*, Optics Express 17(25), pp. 22847-22854 (2009).

[Kle11]   T. KLEINE-OSTMANN & T. NAGATSUMA, *A Review on Terahertz Communications Research*, Journal of Infrared, Millimeter and Terahertz Waves 32(2), pp. 143–171 (2011).

[Lah09]   B. LAHIRI, A. Z. KHOKHAR, R. M. DE LA RUE, S. G. MCMEEKIN, & N. P. JOHNSON, *Asymmetric split ring resonators for optical sensing of organic materials*, Optics Express 17(2), pp. 1107-1115 (2009).

[Lah11]   B. LAHIRI, S. G. MCMEEKIN, R. M. DE LA RUE, & N. P. JOHNSON, *Resonance hybridization in nanoantenna arrays based on asymmetric split-ring resonators*, Applied Physics Letters 98(15), 153116 (2011).

[Lai08]   X. LAI, C.-H. LIANG, T. SU, & B. WU, *Novel Dual-Band Microstrip Filter using Complementary Split-Ring Resonators*, Microwave and Optical Technology Letters 50(1), pp. 7-10 (2008).

[Lee]   Y.-S. LEE, *Principles of Terahertz Science and Technology*, Springer (2009).

[Loh12]   J. G. LOHR, P. STOJANOV, M. S. LAWRENCE, D. AUCLAIR, B. CHAPUY, C. SOUGNEZ, P. CRUZ-GORDILLO, B. KNOECHEL, Y. W. ASMANN, S. L. SLAGER, A. J. NOVAK, A. DOGAN, S. M. ANSELL, B. K. LINK, L. ZOU, J. GOULD, G. SAKSENA, N. STRANSKY, C. RANGEL-ESCAREÑO, J. C. FERNANDEZ-LOPEZ, A. HIDALGO-MIRANDA, J. MELENDEZ-ZAJGLA, E. HERNÁNDEZ-LEMUS, A. SCHWARZ-CRUZ Y CELIS, I. IMAZ-ROSSHANDLER, A. I. OJESINA, J. JUNG, C. S. PEDAMALLU, E. S. LANDER, T. M. HABERMANN, J. R. CERHAN, M. A. SHIPP, G. GETZ, & T. R. GOLUB, *Discovery and prioritization of somatic mutations in diffuse large B-cell lymphoma (DLBCL) by whole-exome sequencing*, Proceedings of NAS 109(10), pp. 3879-3884 (2012).

[Log11]   R. T. LOGAN JR., J. R. DEMERS, & B. L. KASPER, *Portable Coherent Frequency-Domain THz Spectrometer*, Proceedings of SPIE 8032, 80320P (2011).

[Lüke]   J.-R. OHM & H. D. LÜKE, *Signalübertragung*, Springer (2007).

[MDo00]   M. E. MACDONALD, A. ALEXANIAN, R. A. YORK, Z. POPOVÍC, & E. N. GROSSMAN, *Spectral Transmittance of Lossy Printed Resonant-Grid Terahertz Bandpass Filters*, IEEE Transactions on Microwave Theory and Techniques 48(4), pp. 712-718 (2000).

[Mae08]   A. MAESTRINI, J. WARD, G. CHATTOPADHYAY, E. SCHLECHT, & I. MEHDI, *THz Sources Based on Frequency Multiplication and Their Applications*, Frequenz 62(5/6), pp. 118-122 (2008).

[Maier]   S. A. MAIER, *Plasmonics: Fundamentals and Applications*, Springer (2007).

[Mar00]   A. G. MARKELZ, A. ROITBERG, & E. J. HEILWEIL, *Pulsed terahertz spectroscopy of DNA, bovine serum albumin and collagen between 0.1 and 2.0 THz*, Chemical Physics Letters 320(1-2), pp. 42–48 (2000).

[Mar05]   R. Marqués, J. D. Baena, M. Beruete, F. Falcone, T. Lopetegi, M. Sorolla, F. Martín, & J. Garcia, *Ab initio analysis of frequency selective surfaces based on conventional and complementary split ring resonators*, Journal of Optics A 7, pp. S38-S43 (2005).

[Mar08]   A. G. Markelz, *Terahertz Dielectric Sensitivity to Biomolecular Structure and Function*, IEEE Journal of Selected Topics in Quantum Electronics 14(1), pp. 180-190 (2008).

[Mar19]   G. Marconi & C. S. Franklin, US patent 1,301,473, reprint in [Munk1], pp. 7-8 (1919).

[Mat10]   C. Mateo-Segura, G. Goussetis, & A. P. Feresidis, *Resonant Effects and Near-Field Enhancement in Perturbed Arrays of Metal Dipoles*, IEEE Transactions on Antennas and Propagation 58(8), pp. 2523 – 2530 (2010).

[Men04]   A. Menikh, S. P. Mickan, H. Liu, R. MacColl, & X.-C. Zhang, *Label-free amplified bioaffinity detection using terahertz wave technology*, Biosensors and Bioelectronics 20(3), pp. 658–662 (2004).

[Men09]   R. Mendis, V. Astley, J. Liu, & D. M. Mittleman, *Terahertz microfluidic sensor based on a parallel-plate waveguide resonant cavity*, Applied Physics Letters 95(17), No. 171113 (2009).

[Mic02]   S. P. Mickan, A. Menikh, H. Liu, C. A. Mannella, R. MacColl, D. Abbott, J. Munch & X-C Zhang, *Label-free bioaffinity detection using terahertz technology*, Physics in Medicine and Biology 47, pp. 3789-3795 (2002).

[Mic02a] S. P. Mickan, K.-S. Leeb, T.-M. Lub, J. Munch, D. Abbott, & X.-C. Zhang, *Double modulated differential THz-TDS for thin film dielectric characterization*, Microelectronics Journal 33, pp. 1033–1042 (2002).

[Miy10]   F. Miyamaru, Y. Sasagawa, & M. W. Takeda, *Effect of dielectric thin films on reflection properties of metal hole arrays*, Applied Physics Letters 96(2), 021106 (2010).

[Munk1]   B. A. Munk, *Frequency Selective Surfaces Theory and Design*, John Wiley & Sons (2000).

[Munk2]   B. A. Munk, *Finite Antenna Arrays and FSS*, John Wiley & Sons (2003).

[Munk3]   B. A. Munk, *Metamaterials – Critique and Alternatives*, John Wiley & Sons (2009).

[Naf07]   M. Naftaly & R. E. Miles, *Terahertz Time-Domain Spectroscopy for Material Characterization*, Proceedings of the IEEE 95(8), pp. 1658-1665 (2007).

[Nag01]   M. Nagel, T. Dekorsy, M. Brucherseifer, P. Haring Bolivar, & H. Kurz, *Characterization of Polypropylene Thin-Film Microstrip Lines at Millimeter and Submillimeter Wavelengths*, Microwave and Optical Technology Letters 29(2), pp. 97-100 (2001).

[Nag02]   M. Nagel, P. Haring Bolivar, M. Brucherseifer, H. Kurz, A. Bosserhoff, & R. Büttner, *Integrated THz technology for label-free genetic diagnostics*, Applied Physics Letters 80(1), pp. 154-156 (2002).

[Nag03]   M. Nagel, F. Richter, P. Haring-Bolívar, & H. Kurz, *A functionalized THz sensor for marker-free DNA analysis*, Physics in Medicine and Biology 48, pp. 3625-3636 (2003).

[Nag05]   M. Nagel, P. Haring Bolivar, & H. Kurz, *Modular parallel-plate THz components for cost-efficient biosensing systems*, Semiconductor Science and Technology 20, pp. S281–S285 (2005).

[Nag06]   M. Nagel & H. Kurz, *Corrugated waveguide based genomic biochip for marker-free THz read-out*, International Journal of Infrared and Millimeter Waves 27(4), pp. 517-529 (2006).

[Nag11]   T. Nagatsuma, *Terahertz technologies: present and future*, IEICE Electronics Express 8(14), pp. 1127-1142 (2011).

[Oh09]   K.-H. Oh, N. Shimizu, N. Kukutsu, Y. Kado, S. Kohjiro, K. Kikuchi, T. Yamada, & A. Wakatsuki, *Heterodyne THz-wave receiver with a superconducting tunneling mixer driven by a high sweeping-speed photonics-based THz-wave local oscillator*, IEICE Electronics Express 6(10), pp. 601-606 (2009).

[OHa08]   J. F. O'HARA, R. SINGH, I. BRENER, E. SMIRNOVA, J. HAN, A. J. TAYLOR, & W. ZHANG, *Thin-film sensing with planar terahertz metamaterials: sensitivity and limitations*, Optics Express 16(3), pp. 1786-1795 (2008).

[OHa12]   J. F. O'HARA, W. WITHAYACHUMNANKUL, & I. AL-NAIB, *A Review on Thin-film Sensing with Terahertz Waves*, International Journal of Infrared and Millimeter Waves 33(3), pp. 245-291 (2012).

[Öje09]   E. ÖJEFORS, U. R. PFEIFFER, A. LISAUSKAS, & H. G. ROSKOS, *A 0.65 THz Focal-Plane Array in a Quarter-Micron CMOS Process Technology*, IEEE Journal of Solid-State Circuits 44(7), pp. 1968-1976 (2009).

[Oppen]   A. V. OPPENHEIM, R. W. SCHAFER, & J. R. BUCK, *Zeitdiskrete Signalverarbeitung*, Pearson (2004).

[Ord83]   M. A. ORDAL, L. L. LONG, R. J. BELL, S. E. BELL, R. R. BELL, R. W. ALEXANDER JR., & C. A. WARD, *Optical Properties of the metals Al, Co, Cu, Au, Fe, Pb, Ni, Pd, Pt, Ag, Ti, and W in the infrared and far infrared*, Applied Optics 22(7), pp. 1099 – 1119 (1983).

[Pag58]   C. H. PAGE, *Harmonic Generation with Ideal Rectifiers*, Proceedings of the IRE 46(10), pp. 1738-1740 (1958).

[Pan58]   R. H. PANTELL, *General Power Relationships for Positive and Negative Nonlinear Resistive Elements*, Proceedings of the IRE 46(12), pp. 1910-1913 (1958).

[Pap08]   N. PAPASIMAKIS, V. A. FEDOTOV, N. I. ZHELUDEV, & S. L. PROSVIRNIN, *Metamaterial Analog of Electromagnetically Induced Transparency*, Physical Review Letters 101(25), 253901 (2008).

[Par05]   R. PARTHASARATHY, T. GLOBUS, T. KHROMOVA, N. SWAMI, & D. WOOLARD, *Dielectric properties of biological molecules in the Terahertz gap*, Applied Physics Letters 87(11), 113901 (2005).

[Pel09]   M. PELUSI, F. LUAN, T. D. VO, M. R. E. LAMONT, S. J. MADDEN, D. A. BULLA, D.-Y. CHOI, B. LUTHER-DAVIES, & B. J. EGGLETON, *Photonic-chip-based radio-frequency spectrum analyser with terahertz bandwidth*, Nature Photonics 3(3), pp. 139 – 143 (2009).

[Pen99]   J. B. PENDRY, A. J. HOLDEN, D. J. ROBBINS, & W. J. STEWART, *Magnetism from Conductors and Enhanced Nonlinear Phenomena*, IEEE Transactions on Microwave Theory and Techniques 47(11), pp. 2075-2084 (1999).

[Penfi]   P. PENFIELD JR. & R. P. RAFUSE, *Varactor Applications*, The M.I.T. Press (1964).

[Pet97]   K. A. PETERLINZ, R. M. GEORGIADIS, T. M. HERNE, & M. J. TARLOV, *Observation of Hybridization and Dehybridization of Thiol-Tethered DNA Using Two-Color Surface Plasmon Resonance Spectroscopy*, Journal of the American Chemical Society 119(14), pp. 3401-3402 (1997).

[pic]   Website of Picometrix LLC, *http://www.picometrix.com*, (November 2011).

[Pic06]   E. Pickwell & V. P. Wallace, Biomedical applications of terahertz technology, Journal of Physics D: Applied Physics 39, pp. R301–R310 (2006).

[Pla05]   P. C. M. PLANKEN, C. E. W. M. VAN RIJMENAM, & R. N. SCHOUTEN, *Opto-electronic pulsed THz systems*, Semiconductor Science and Technology 20, pp. S121–S127 (2005).

[Pozar]   D. M. POZAR, *Microwave Engineering*, John Wiley & Sons (2005).

[Pro03]   S. PROSVIRNIN & S. ZOUHDI, *Resonances of closed modes in thin arrays of complex particles*, in S. Zouhdi et al., Advances in Electromagnetics of Complex Media and Metamaterials, pp. 281-290, Kluwer Academic Publishers (2003).

[Rau05]   C. RAU, G. TOROSYAN, R. BEIGANG, & K. NERKARARYAN, *Prism coupled terahertz waveguide sensor*, Applied Physics Letters 86(21), 211119 (2005).

[Rog10]   A. ROGGENBUCK, H. SCHMITZ, A. DENINGER, I. CÁMARA MAYORGA, J. HEMBERGER, R. GÜSTEN, & M. GRÜNINGER, *Coherent broadband continuous-wave terahertz spectroscopy on solid-state samples*, New Journal of Physics 12, 043017 (2010).

[rpg]   Website of Radiometer Physics GmbH, *http://www.radiometer-physics.de* (October 2011).

[Saf07]   A. M. E. SAFWAT, S. TRETYAKOV, & A. RÄISÄNEN, *Dual Bandstop Resonator Using Combined Split Ring Resonator and Defect Ground Structure*, Microwave and Optical Technology Letters 49(6), pp. 1249-1253 (2007).

[Sak05]   K. SAKAI & M. TANI, *Introduction to Terahertz Pulses*, in K. Sakai, Terahertz Optoelectronics, pp. 1-30, Springer (2005).

[Sch99]   G.W. SCHWAAB, *Heterodyne spectrometers*, Infrared Physics & Technology 40(3), pp. 207–218 (1999).

[Sch10]   M. SCHELLER, K. BAASKE, & M. KOCH, *Multifrequency continuous wave terahertz spectroscopy for absolute thickness determination*, Applied Physics Letters 96(15), 151112 (2010).

[She01]   R. A. SHELBY, D. R. SMITH, & S. SCHULTZ, *Experimental Verification of a Negative Index of Refraction*, Science 292, pp. 77-79 (2001).

[Shu11]   P. SHUMYATSKY & R. R. ALFANO, *Terahertz sources*, Journal of Biomedical Optics 16(3), 033001 (2011).

[Sie04]   P. SIEGEL, *Terahertz Technology in Biology and Medicine*, IEEE Transactions on Microwave Theory and Techniques 52(10), pp. 2438-2447 (2004).

[Sin11]   R. SINGH, I. A. I. AL-NAIB, M. KOCH, & W. ZHANG, *Sharp Fano resonances in THz metamaterials*, Optics Express 19(7), pp. 6312 – 6319 (2011).

[Siz10]   F. SIZOV, *THz radiation sensors*, Opto-Electronics Review 18(1), pp. 10-36 (2010).

[Sun10]   H. SUN, Y. J. DING, & I. B. ZOTOVA, *THz Spectroscopy by Frequency-Tuning Monochromatic THz Source: From Single Species to Gas Mixtures*, IEEE Sensors Journal 10(3), pp. 621-629 (2010).

[Tan09]   T. TANABE, S. RAGAM, & Y. OYAMA, *Continuous wave terahertz wave spectrometer based on diode laser pumping: Potential applications in high resolution spectroscopy*, Review of Scientific Instruments 80, 113105 (2009).

[Tao11]   H. TAO, E. A. KADLEC, A. C. STRIKWERDA, K. FAN, W. J. PADILLA, R. D. AVERITT, E. A. SHANER, & X. ZHANG, *Microwave and Terahertz wave sensing with metamaterials*, Optics Express 19(22) pp. 21620-21626 (2011).

[The10]   M. THEUER, R. BEIGANG, & D. GRISCHKOWSKY, *Highly sensitive terahertz measurement of layer thickness using a two-cylinder waveguide sensor*, Applied Physics Letters 97(7), 071106 (2010).

[The11]   M. THEUER, D. R. GRISCHKOWSKY, & R. BEIGANG, *Hochempfindliche Dünnschichtsensoren basierend auf Terahertz-Wellenleitern*, Technisches Messen 78(5), pp. 268-273 (2011).

[Thumm]   M. THUMM, W. WIESBECK, & S. KERN, *Hochfrequenzmeßtechnik*, B. G. Teubner (1997).

[Varda]   J. C. VARDAXOGLOU, *Frequency Selective Surfaces*, Research Studies Press (1997).

[vdi]   Website of Virginia Diodes, Inc., *http://vadiodes.com* (October 2011).

[vEx89]   M. VAN EXTER, C. FATTINGER, & D. GRISCHKOWSKY, *High-brightness terahertz beams characterized with an ultrafast detector*, Applied Physics Letters 55(4), pp. 337-339 (1989).

[vHipp]   A. R. VON HIPPEL, *Dielectrics and Waves*, Artech House (1995).

[Win99]   C. WINNEWISSER, F. LEWEN, J. WEINZIERL, & H. HELM, *Transmission features of frequency-selective components in the far infrared determined by terahertz time-domain spectroscopy*, Applied Optics 38(18), pp. 3961-3967 (1999).

[Wit07]   W. WITHAYACHUMNANKUL, G. M. PNG, X. YIN, S. ATAKARAMIANS, I. JONES, H. LIN, B. S. Y. UNG, J. BALAKRISHNAN, B. W.-H. NG, B. FERGUSON, S. P. MICKAN, B. M. FISCHER, & D. ABBOTT, *T-Ray Sensing and Imaging*, Proceedings of the IEEE (95)8, pp. 1528-1558 (2007).

[Wit08]   W. WITHAYACHUMNANKUL, B. M. FISCHER, & D. ABBOTT, *Material thickness optimization for transmission-mode terahertz time-domain spectroscopy*, Optics Express 16(19), pp. 7382-7396 (2008).

[websk]   Website of Web of Knowledge, *http://apps.webofknowledge.com* (September 2011).

[Wu]   T. K. WU, *Frequency Selective Surface and Grid Array*, John Wiley & Sons (1995).

[You09]   B. YOU, T.-A. LIU, J.-L. PENG, C.-L. PAN, & J.-Y. LU, *A terahertz plastic wire based evanescent field sensor for high sensitivity liquid detection*, Optics Express 17(23), pp. 20675-20683 (2009).

[You10]   B. YOU, J.-Y. LU, J.-H. LIOU, C.-P. YU, H.-Z. CHEN, T.-A. LIU, & J.-L. PENG, *Subwavelength film sensing based on terahertz anti-resonant reflecting hollow waveguides*, Optics Express 18(18), pp. 19353-19360 (2010).

[Zhang]   X.-C. ZHANG & J. XU, *Introduction to THz Wave Photonics*, Springer (2010).

[Zha02]   G. ZHAO, R. N. SCHOUTEN, N. VAN DER VALK, W. T. WENCKEBACH, & P. C. M. PLANKEN, *Design and performance of a THz emission and detection setup based on a semi-insulating GaAs emitter*, Review of Scientific Instruments 73(4), pp. 1715-1719 (2002).

[Zinke]   O. ZINKE & H. BRUNSWIG, *Höchstfrequenztechnik 1*, Springer (2000).

[Zinke2]   O. ZINKE & H. BRUNSWIG, *Höchstfrequenztechnik 2*, Springer (1999).

[zom]   Website of Zomega Terahertz Corporation, *http://www.zomega-terahertz.com* (November 2011).

Permissions

__Danksagung__

Diese Dissertation und die zugrundeliegende Forschungsarbeit entstanden während meiner Zeit als wissenschaftlicher Mitarbeiter am Lehrstuhl für Höchstfrequenztechnik und Quantenelektronik an der Universität Siegen unter der Leitung von Herrn Prof. Peter Haring Bolivar. Ich danke Herrn Haring dafür, dass er das „Projekt Biosensing" auch unter ungewöhnlichen Umständen über die Jahre hinweg immer voran gebracht hat, dass er mir die Arbeit an diesem Thema ermöglicht hat und nicht zuletzt dass er mir schon früh die Möglichkeit gegeben hat, elektromagnetische Felder und Wellen am Computer simuliert darzustellen und zu verstehen.

Ich danke meinen Kollegen am Lehrstuhl für die immer verfügbare Unterstützung, die vielen Diskussionen und die konstruktive Kritik, insbesondere Herrn Dustin Polke, der von Anfang an mit mir zusammen durch die Hochs und Tiefs des Forschungsalltags geschritten ist; Herrn Gunnar Spickermann, dessen schier unendliche Neugier immer wieder dazu führte weitere Details zu betrachten; und Herrn Dr. Heiko Schäfer-Eberwein für seine Unterstützung in Sachen Biochip-Herstellung und die vielen Stunden im Technologielabor.

Ich danke Herrn Dr. Michael Nagel für die Prozessentwicklung und die Herstellung der Biochips im Labor des Instituts für Halbleitertechnik an der RWTH Aachen, den Mitarbeitern vom Support der Firma Ansoft, die mir immer geholfen haben, wenn ich ihr HFSS wieder über seine Möglichkeiten hinaus beanspruchen wollte und Herrn Dr. Torsten Löffler der Firma Synview für die Unterstützung im Umgang mit dem T-Ranger und seiner Software.

Ich danke allen Korrekturlesern dieser Ausarbeitung für ihre Fehlersuche und Kritik. Wer jetzt noch Schreibfehler findet, der darf sie behalten.

Ich danke Frau Heike Brandt, dass sie den Papierkrieg gegen die Verwaltung für mich gewonnen hat; den Mitarbeitern des Studentenwerks der Universität Siegen und meinen Kollegen anderer Lehrstühle, insbesondere Herrn Stephan Meyer, für die erfrischenden Mittagspausen; Amerika für die Erfindung der Food-Hall; und allen Veranstaltern und Teilnehmern der CLEO-Konferenzen, auf denen ich Motivation getankt habe.

Ich danke meinen Eltern, meiner Schwester und meinen Freunden dafür, dass sie mich jederzeit unterstützt und angetrieben haben.

Ich danke Melanie dafür, dass sie immer da ist, um Freud und Leid mit mir zu teilen.

The detection and characterization of dielectric thin-films and biomolecules are of great interest for THz-research due to characteristic material properties at these frequencies. The detection of films much thinner than wavelength or material amounts in femtomol range requires specialized sensors. The sensors identify a material's permittivity, or refractive index, respectively, by a signal delay in the time domain or the detuning of a resonator in the frequency domain. A biochip in particular aims at the detection of sub-µm-size molecules, such as DNA or proteins.

This work begins with a review of the state-of-the-art THz-thin-film sensing approaches evolving towards lower film thicknesses. These indicate that more promising results are achieved with high-Q resonators due to their more efficient sample/E-field interaction. The asymmetric double-split ring resonator (aDSR) is researched, exhibiting a sharp resonance feature and a strong concentration of the electric field. In a two-dimensional array, corresponding to a frequency selective surface, the aDSR qualifies as the basic element for a biochip with a high sensitivity. For the biochip development material properties as well as practical and commercial aspects are taken into account. The result is a glass chip with a structured three-layer metal surface and undercut edges.

With regard to practical aspects, a biochip reader is developed being compact, easy to use, of low-maintenance and affordable, to find application in biomedical laboratories. The reader is essentially a fully-electronic spectrometer for 240 - 320 GHz, reading a single measurement spot in 110 Milliseconds. Compared to a classical network analyzer, the setup has reduced complexity and cost. It generates the high frequencies from a single voltage controlled oscillator by upconverting in diode-based mixers. Heterodyne detection is realized by utilizing the time delay of the signal sweeping through the frequency band.

The functionality of biochip and reader is compared to TDS measurements proving good results. The detection of dielectric thin-films is successfully applied with dye, photo-resist and gelatin. Hybridized DNA, deposited locally by a functionalization process, is detected. However, the DNA detection could not be confirmed by additional measurements. Causes for this failure are investigated and discussed.

UNIVERSITÄT
SIEGEN